Mémoire

Auteur : Tasseroul, Mathilde
Promoteur(s) : De Becker, Michaël
Faculté : Faculté des Sciences
Diplôme : Master en sciences spatiales, à finalité approfondie
Année académique : 2023-2024
URI/URL : http://hdl.handle.net/2268.2/21434

Faculty of Sciences

Department of Astrophysics, Geophysics and Oceanography ; Space Sciences Master Research focus

Multi-band radio study of the particle-accelerating colliding-wind binary WR 147

Author:
Mathilde Tasseroul

Supervisor:
Michaël De Becker

Reading committee:
Gaël Buldgen
Valentin Christiaens
Michaël De Becker
Dominique Sluse

Academic year 2023-2024

Acknowledgements

First of all, I would like to deeply thank my supervisor, Dr.Michaël De Becker, who helped and supported me during this year for this Master's thesis. Thanks to him, I discovered the fascinating PACWBs objects and got a glimpse of the complex and intriguing world of radio astrophysics. He made me want to explore this field further. Without his numerous advice, suggestions and attentive listening this master's thesis would not have been possible.

Secondly, I am also grateful to Agustina Belen Blanco who taught me all about radio data processing. She agreed to take her time to explain everything I had to know and more. I learned a lot thanks to the many hours she spent with me. Her patience and kindness became essential to this work.

Thirdly, I thank the members of the Reading Committee, Dominique Sluse, Valentin Christiaens, Michaël De Becker, and Gaël Buldgen for the time they devote to the reading of this manuscript.

Then, I would like to thank my friends at the university who made these two master's years easier and lighter thanks to their cheerfulness. I also address a big thanks to my oldest friends from secondary school who always allowed me to think about something else when I needed to.

Lastly, I must thank my family, especially my parents, Solange and Francis, and my sister, Adrienne, who have always trusted me since the first year of my studies. I couldn't have asked for anything better than their encouragement and their presence all along these years. My last thanks goes to my partner, Cedric, who has always been by my side, supporting me through the best and the worst of times.

Abstract

Massive stars can be characterized by various properties. Two of them are their winds and their multiplicity. Since massive stars are more likely to be part of a binary system, their winds may collide and interact. These systems are called colliding-wind binaries (CWB). CWBs in which some charged particles in the wind collisions region are accelerated to relativistic velocities are called particle-accelerating colliding-wind binaries (PACWB). This master thesis focuses on one of them, WR 147. The physics and properties of these objects are discussed in Chap. 1.

In Chap. 2 the radiative processes are presented. Indeed, two types of radio emission can be observed in these PACWB systems. On the one hand, the thermal emission, also called Bremsstrahlung, comes from the ionized wind of the stars. On the other hand, the non-thermal emission, or synchrotron emission, is produced by relativistic electrons accelerated by the Diffusive Shock Acceleration process (DSA). The low frequency part of the spectrum is likely to be affected by so-called turnover processes, leading to a severe drop of the synchrotron flux. Among these processes, free-free absorption is the most likely to affect the radio spectrum of PACWBs.

This master thesis includes the analysis of the radio emission of WR 147 in two radio frequency bands. More precisely, it aims at achieving a deeper understanding of the WR 147 behavior at these frequencies through a detailed intra-band investigation. In particular, it focuses on low frequencies where the synchrotron emission is stronger but also more susceptible of being affected by turnover processes that are often difficult to constrain.

Data from the Jansky Very Large Array (JVLA) are used for this purpose. After processing the radio data, including flagging, calibrating, and imaging steps, the flux density of the source is obtained in both bands but also in each sub-band. All these steps are described in Chap. 3. With these flux densities, several fits are proposed, in Chap. 4, notably based on the foreground absorption model. Several parameters are determined such as the thermal and non-thermal spectral indices. However, it is observed that this model is not adapted to the behavior of WR 147 at low frequencies. Thus a new model, the internal absorption model, is proposed. It consists in the absorption of the synchrotron radio emission by thermal electrons located in the emission region, and not by material surrounding the emission region. It seems that this new model better represents the behavior of WR 147, although it does not lead to a perfect fit.

Then, in Chap. 5, several elements of discussion are addressed based on the parameters and fits of the different models. These include the value of the compression ratio, the justification of the turnover process at play being free-free absorption, and the possible influence of a third star in the system. The relevance of the internal absorption model is also discussed in detail. Finally, a more general model combining the foreground absorption model and the internal absorption model is proposed to generalize the behavior of PACWBs. In Chap. 6 several perspectives for future observations are considered, notably based on the internal absorption model and on the general model.

Contents

Chapter 1

Introduction

1.1 Basic concepts of stellar astrophysics

Stars are characterized by various properties such as their mass, luminosity, temperature, and composition. Stars are not immutable objects, their characteristics will evolve during their lives.

It may be worth defining more precisely the notion of a star's spectral type. The spectral classification of a star is linked to its luminosity (L) and its effective temperature (T_{eff}). Indeed, the luminosity of a star is given by :

$$L = 4\pi R^2 F = 4\pi R^2 \sigma T_{eff}^4 \tag{1.1}$$

where the flux (F), given by the Stephan Boltzmann law, is multiplied by the surface of the star (assumed to be spherical). Moreover, the effective temperature is the temperature that a black body with the same radius and luminosity as the considered star would have (Dupret, 2022). It can be inferred from the properties of a black body that hotter stars radiate more energy than cooler ones (De Becker, 2022).

The spectral type of a star is defined according to its effective temperature in the following order:

O B A F G K M

In this sequence, O-type stars are characterized by the highest effective temperature (up to $\sim$ 100 000 K) and M-type stars have the lowest effective temperature ($\sim$ 3 000 K)

In addition to that, it is possible to refine the spectral type classification by making use of a number directly following the letter from the classification sequence. These numbers range between 0 and 9.5, with the lowest number standing for the highest effective temperature. Moreover, according to Wien's law, the color of a star is related to its effective temperature.

$$\lambda_{max}(cm) = \frac{0.29}{T(K)} \tag{1.2}$$

If a star has a higher effective temperature, its spectrum will peak in the bluer wavelengths; inversely, if a star has a lower effective temperature, its spectrum will peak at redder wavelengths.

Stars with the highest effective temperature in the above sequence are also the most massive ones. Since massive stars will be at the core of this work, their properties and main important features as their winds or multiplicity will be presented in Sect. 1.2. Besides, a particular focus will be set on Wolf-Rayet stars in Sect. 1.2.4. Then, in Sect. 1.3, an overview of the shock physics that can arise in massive stars will be given with a specific interest in shocks taking place in a binary system made of two massive stars. As a last point of the introduction, a sketch of the target of interest, WR 147, together with the objectives of this work will be presented in Sect. 1.4.

1.2 Massive Stars

1.2.1 Definition and main properties

In this work, the focus will be set on the most massive types of stars. They encompass O and early-B-type stars, along with their evolved counterparts known as Wolf-Rayet (WR) stars. Let's define these categories and some properties that are useful for this work.

Stars can be roughly categorized into low and intermediate-mass stars on the one hand, and massive stars on the other hand. The minimum stellar mass required for massive stars is about $8\,M_{\odot}$. The main criterion to establish this mass limit comes from their evolution. All stellar types go first through the main sequence in which central fusion of hydrogen occurs. However, stellar evolution follows significantly different pathways at more advanced stages of their evolution, depending on their mass. Unlike low and intermediate-mass stars, massive stars have a high enough temperature and pressure to go further than the production of carbon and oxygen and trigger successive combustion of heavier elements until iron. The reaction products accumulate in the star center and the next reaction is triggered, which explains why they have an "onion"-like structure (successive layers). These nuclear reactions lead to iron production and at that point, it is no longer possible to produce energy by nuclear fusion. It results in a rapid contraction of the core becoming a neutron star or a black hole. The external layers of the star are expelled into the surrounding medium. Thus, massive stars end up as a core-collapse supernova.

It is relevant to present the stellar parameters of massive stars, specifically of O-type stars, to achieve a global view of these objects. The corresponding values of the stellar parameters can be found in Martins et al. (2005). According to this study, the effective temperatures are situated between 30 000 K and 45 000 K with the highest effective temperature for the earliest spectral types. The variations of these values depend also on the luminosity class V, III, I corresponding to dwarfs, giants, and supergiants, respectively.
Several other O-type stellar parameters are also worth mentioning, such as:

- $log\frac{L}{L_{\odot}}$ between 4.6 and 6
- Radius (in $R_{\odot}$) between 7.3 and 23
- Mass (in $M_{\odot}$) between 16.4 and 66.8

Another important property of massive stars is their winds. Given their high importance regarding this work, the winds of massive stars will be described in more detail in Sect. 1.2.2.

1.2.2 Stellar winds

Winds are an important feature of massive stars because they affect and shape their surroundings due to their injection of matter, energy, and momentum.

These winds are driven thanks to the radiation pressure. It is explained by the absorption of a photon from the photosphere by an ion in the stellar atmosphere, that gains radial momentum. The photon is then re-emitted in a random direction, which leads to an acceleration of the ion (Rauw, 2023). This is the line-driving mechanism in which the outflow of the wind is driven by the transfer of energy and momentum from the radiation field to the atmosphere through the absorption of photons in atomic transitions (Muijres et al., 2012).

To describe stellar wind several quantities must be defined. These quantities are the mass-loss rate $\dot{M}$, the terminal velocity v_∞, and the kinetic power of the stellar wind P_{kin}.
The mass loss rate can be expressed thanks to the equation of mass continuity according to Muijres et al. (2012) as follows:

$$\dot{M} = 4\pi r^2 v(r)\rho(r) \tag{1.3}$$

$\rho(r)$ is the mass density and $v(r)$ is the velocity at radius r. $v(r)$ describes the velocity structure outside the photosphere which involves the second important wind parameter, i.e., the terminal velocity v_∞:

$$v(r) = v_\infty \left(1 - \frac{R}{r}\right)^\beta \tag{1.4}$$

where R is the stellar radius. The terminal velocity of the wind is the maximum velocity value that can be reached by the wind at a distance r from the star radius. The β parameter rules how fast this terminal velocity will be reached.
Muijres et al. (2012) had predicted values for the mass-loss rate and terminal wind velocities for massive O-type stars based on stellar parameters established by Martins et al. (2005). The mass-loss rate takes values between 10^{-5} and 10^{-8} solar mass per year (depending on the spectral type and evolutionary stage) and the terminal velocity is typically a few thousand km/s.

Finally, the kinetic power of a stellar wind is given by:

$$P_{kin} = \frac{1}{2}\dot{M}v_\infty^2 \tag{1.5}$$

It expresses the amount of kinetic energy flowing per unit of time in the stellar wind. For example, on the basis of De Becker and Raucq (2013), the kinetic power of a O4 dwarf star is $3.2 \times 10^{36}\,\mathrm{erg\,s^{-1}}$ and $7.7 \times 10^{36}\,\mathrm{erg\,s^{-1}}$ for a O5 supergiant star.

The energy budget is also an important aspect of these winds looking at all the energy available in massive stars. In this case, it is the fraction of the bolometric luminosity converted into the kinetic power of the stellar wind. However, this fraction will depend on the composition of the outer layers of the star but also on the evolutionary stage of the star (De Becker and Raucq, 2013). Indeed, this conversion is more efficient for Wolf-Rayet stars than O-type stars. Wolf-Rayet stars will be more detailed in Sect. 1.2.4.

1.2.3 Multiplicity

A multiple-star system is a system of two or more gravitationally bound stars. According to Offner et al. (2023), this can lead to separations ≤ 0.1 pc. Although it may be thought that single stars are more common than multiple systems, it is not necessarily the case, especially for some spectral types. Indeed, according to Offner et al. (2023), a significant fraction of stars have at least one stellar companion. To quantify this trend, the multiplicity fraction (MF) can be used. It is defined as the fraction of primaries (stars) with at least one companion (S, B, T, and Q being the number of single stars, binaries, triples, and quadruples):

$$MF = \frac{B + T + Q + ...}{S + B + T + Q + ...}$$

The triple/high-order fraction (THF) can be defined in the same way as:

$$THF = \frac{T + Q + ...}{S + B + T + Q + ...}$$

In Offner et al. (2023), the authors analyze multiplicity statistics versus the primary mass. The first part of their study includes F, G, K Dwarfs, M Dwarfs, Brown Dwarfs, A stars, and also B and O-type stars. The general behavior of the multiplicity statistics can be seen in Fig. 1.1. The MF and THF grow monotonically with the primary mass, meaning that there is a higher probability to have, at least, a binary system among massive stars such as B and O-type stars (in the main sequence). More precisely, the MF goes from $\approx 20\%$ for Brown Dwarfs and late-M dwarfs, to $\approx 50\%$ for solar-type stars and is even $> 90\%$ for OB-type stars. Concerning the TFH, it is $\approx 2\%$, 14%, and 70% for late-M dwarfs, FGK dwarfs and O-type stars, respectively. As a general trend, 58% of main sequence stars are members of multiples, which implies that most of the main sequence stars are members of multiples even though it can vary with environment density.

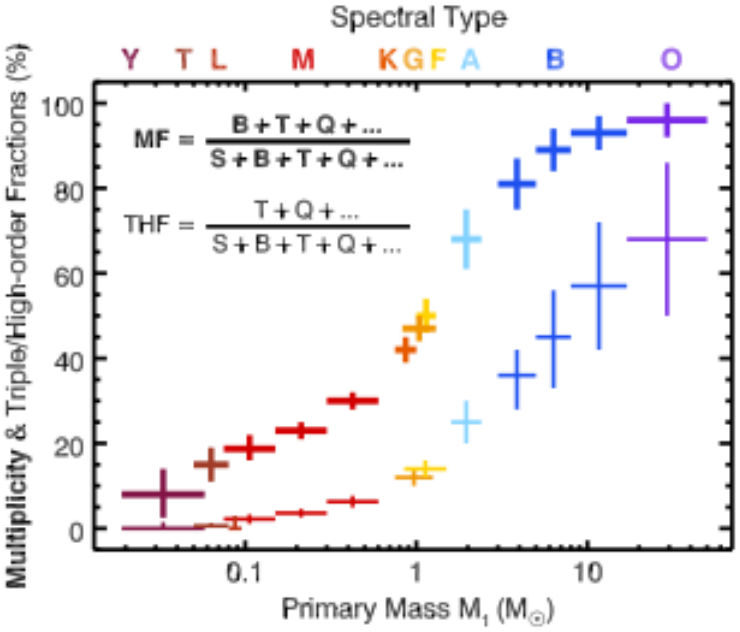

Figure 1.1: Multiplicity fraction and triple/high order fraction of Brown dwarfs and main sequence stars taken from Offner et al. (2023)

Most massive stars are thus part of binary or higher multiplicity systems. Massive systems also show a wide range of orbital parameters such as eccentricity (from circular to highly eccentric orbits) and orbital period (from a few days up to several decades, or even more). An interesting phenomenon of massive multiple systems is the collision of their winds, which opens up relevant opportunities from the point of view of shock physics. This work will notably focus on this point.

1.2.4 Wolf-Rayet stars

Definition

It has been emphasized in the previous section that massive stars have a significant impact on the interstellar medium through their winds and their evolution into a supernova. The most massive ones, with a mass $\geq 20 M_{\odot}$, are expected to go through a Wolf-Rayet phase during their evolution. Wolf-Rayet stars are the evolved counterparts of the massive O and/or B-type stars and, thus, will result in supernovae with a compact remnant such as a neutron star or a black hole at their center. WR stars are notably distinguished through their strong, broad emission lines, their fast and dense winds, and their high luminosity.

Classification

Wolf-Rayet stars display spectroscopically, strong and broad emission lines in contrast to their younger progenitor stars, which have narrow absorption lines (Crowther, 2007). This emission spectrum comes mainly from the winds due to their high density (Rauw, 2023). The standard classification of Wolf-Rayet stars is based on these emissions lines. There are three main categories: the WN type, showing nitrogen and helium lines, the WC-type, showing helium and carbon lines, and the WO type, showing helium and oxygen lines (Crowther, 2007). These lines reflect the composition of their atmosphere with the nitrogen in WR being the product of the CNO cycle and the carbon/oxygen being the product of helium burning (triple α process). On top of that, a "h" suffix in the spectral type indicates the presence of hydrogen lines (Crowther, 2007).

As for classical stars, it is possible to refine the spectral classification. WN stars may be categorized as 'early WN' (WNE) for WN2 to WN5 or 'late WN' (WNL) for WN7 to WN9 depending on the line ratio of N III-V and He I-II. In addition, they can be tagged as weak(-w) and strong (-s) depending on the equivalent widths of He$II\lambda$5412 being smaller or larger than 40 Å (Crowther, 2007). WO-type stars can be sub-classified from WO1 to WO4 depending on the relative strength of O V-VI and C IV emission lines.

Physical and wind properties of Wolf-Rayet stars

As has been done for the massive O-stars, it may be interesting to comment on the stellar parameters for Wolf-Rayet stars. The following values are taken from the general review on WR stars (Crowther, 2007) and are summarized in Fig. 1.2

Sp	T_*	$\log L$	$\dot{M}$	v_∞	logN(LyC)	M_v	Example
Type	kK	$L_\odot$	$M_\odot \mathrm{yr}^{-1}$	$\mathrm{km\,s}^{-1}$	$\mathrm{ph\,s}^{-1}$	mag	
			WN stars				
3-w	85	5.34	–5.3	2200	49.2	–3.1	WR3
4-s	85	5.3	–4.9	1800	49.2	–4.0	WR6
5-w	60	5.2	–5.2	1500	49.0	–4.0	WR61
6-s	70	5.2	–4.8	1800	49.1	–4.1	WR134
7	50	5.54	–4.8	1300	49.4	–5.4	WR84
8	45	5.38	–4.7	1000	49.1	–5.5	WR40
9	32	5.7	–4.8	700	48.9	–6.7	WR105
			WNha stars				
6ha	45	6.18	–5.0	2500	49.9	–6.8	WR24
9ha	35	5.86	–4.8	1300	49.4	–7.1	WR108
			WC and WO stars				
(WO)	(150)	(5.22)	(–5.0)	(4100)	(49.0)	(–2.8)	(BAT123)
(4)	(90)	(5.54)	(–4.6)	(2750)	(49.4)	(–4.5)	(BAT52)
5	85	5.1	–4.9	2200	48.9	–3.6	WR111
6	80	5.06	–4.9	2200	48.9	–3.6	WR154
7	75	5.34	–4.7	2200	49.1	–4.5	WR90
8	65	5.14	–5.0	1700	49.0	–4.0	WR135
9	50	4.94	–5.0	1200	48.6	–4.6	WR103

Figure 1.2: Physical and wind properties of Milky Way WR stars, with WR stars from the Large Magellanic Cloud in parenthesis. This table is taken from Crowther (2007)

The effective temperature varies with the spectral classification. WN stars seem to have lower effective temperatures than WNh and WC/WO stars. The effective temperatures are notably higher for earlier subtypes than for later subtypes.

In contrast to the effective temperature, the luminosity does not show a clear trend when WN and WC/WO types are compared. One only notices that WNha stars seem brighter.

Finally, the mass of WR stars, which is not included in the table, has typical values of $10 - 25\,M_\odot$ and more particularly between $10 - 15\,M_\odot$ for hydrogen-free WR stars (Crowther, 2007).

Since the winds are a major feature of massive stars, including Wolf-Rayet stars, it is also important to quantify some of their main properties such as the mass-loss rate and terminal velocity. Their values are also presented in Fig. 1.2.
The mass-loss rate and terminal velocities for Wolf-Rayet stars are given by the same formulas (Eq. 1.3) and (Eq. 1.4) as for massive O-stars.
The terminal velocity of WR stars depends on the spectral type, with higher values for WNha and WO/WC stars. Moreover, higher values of the terminal velocity correspond to the earlier subtypes. Unlike the terminal velocity, the mass-loss rate seems to depend neither on spectral type nor on the subtypes.

A last wind property that deserves to be mentioned is the metallicity dependence. Nugis and Lamers (2000) have established the mass-loss dependence of WC and WN stars according to their metallicity :

$$log\frac{\dot{M}}{M_\odot yr^{-1}} = -11.00 + 1.29logL/L_\odot + 1.74logY + 0.47logZ$$

Y and Z are the fractions of helium and metals respectively. As a global trend, stronger winds are observed for WR stars with higher metallicity.

Multiplicity

It was emphasized, in Sect. 1.1, that the probability of having a multiple system was higher for massive main sequence stars. Specific studies were undertaken to determine the binary fraction of WR stars. Here are a few of them. The first one concerns Galactic WC-type WR stars (Dsilva et al., 2020), the second one concerns Galactic WNE stars (Dsilva et al., 2022), and the third one concerns the Galactic WNL population (Dsilva et al., 2023). The intrinsic binary fraction they derived for each of these three categories is:

- WC: 0.96
- WNE: 0.56
- WNL: 0.62

As for O-type stars, WR stars seem to be mainly found in a binary system. This trend has consequences on their evolution as it will be seen below.

Formation scenarios and evolution

Massive stars may evolve in different ways, depending on their initial mass and whether they are part of a multiple system. In Dsilva et al. (2020), Dsilva et al. (2022) and Dsilva et al. (2023), they derive the intrinsic binary fraction for WC, WNL, and WNE stars as well as their orbital period, which allows to put constraints on the evolution of each type.

First of all, single WR stars were thought to evolve according to the "Conti Scenario" (Maeder, 1996). In this scenario, main sequence O-type stars may evolve into a Luminous Blue Variable (LBV). These LBV are eruptive variable stars characterized by sporadic

huge mass ejection events followed by long periods of quiescence (Rauw, 2023). Then, due to their winds, they get rid of their external layers which leads to the exposure of the products of the H-burning followed by the products of He-burning (nitrogen and carbon) (Dsilva et al., 2022). This evolution sequence can be summarized as follows:

$$O \rightarrow LBV \rightarrow WN \rightarrow WC \rightarrow WO$$

It has to be noted that the LBV transition is not yet completely understood and even in some cases may be set aside (Crowther, 2007).

Then, as shown in the previous section, WR stars have a higher probability of being part of a binary system. The two components may interact and influence the evolution of the WR. There are different types of interaction such as mass transfer, common-envelope evolution, or mergers. As a conclusion of their study, in Dsilva et al. (2023), several binary evolution channels are proposed regarding the orbital period of each spectral type. Moreover, they underlined in Dsilva et al. (2020) a lack of short-period WC-type stars with an orbital period distribution peaking at ($P \sim 5000\,\mathrm{d}$) unlike WN stars which present a majority of short-period binaries (with a peak at $P < 5\,\mathrm{d}$). In this way, this discrepancy in the orbital period distribution leads to the different evolutionary channels. One of them, for example, concerns short-period WN binaries which can be explained by mass transfer from the primary to the secondary star. This leads to the loss of the hydrogen envelope of the primary, resulting in a WN star. Taking into account the multiplicity of LBV, an other evolutionary channel is proposed for long-period stars namely $O \rightarrow LBV \rightarrow WN \rightarrow WC$.

1.3 Shock physics in massive stars

1.3.1 Colliding-Wind Binaries

It was established in Section 1.2 that massive stars have powerful winds as well as a higher probability of being part of a binary system. In these conditions, the winds of the two massive stars in a binary system may interact.

Such systems are called Colliding-Wind Binaries (CWB). A representation of a CWB is displayed in Fig. 1.3. The particular region of space where these winds interact is called the Wind-Wind Collision Region (WCR). Since these winds propagate at hypersonic speeds, each of the two winds that collide produces a high-Mach-number shock (this notion will be detailed in Sect. 1.3.2), with a contact discontinuity in between the two shock fronts. This discontinuity constitutes a separation between the two shocked plasmas and is defined so that the pressure on both sides is balanced. Shocks may arise in different ways. It can take either the form of a coulombic interaction, which implies a collision between two charged particles, or a collisionless hydrodynamic shock. The latter arises when the gas density is low enough, implying that the mean free path of the particles is greater than the length scale of the shocks (De Becker and Van Grootel, 2022). In the context of a wind-wind collision in this work, only collisionless shocks will be considered. The main consequences of these shocks at the WCR are the heating of the plasma up to temperatures above $10^7\,\mathrm{K}$ and the decrease of the wind velocities in the post-shock region (Pittard et al., 2020). It illustrates the conversion of the kinetic energy of the wind into thermal energy. The gas in the interaction region is said to be "shocked". This shocked region is thus bounded on either side by the two magneto-hydrodynamics (MHD) shocks produced by each stellar wind.

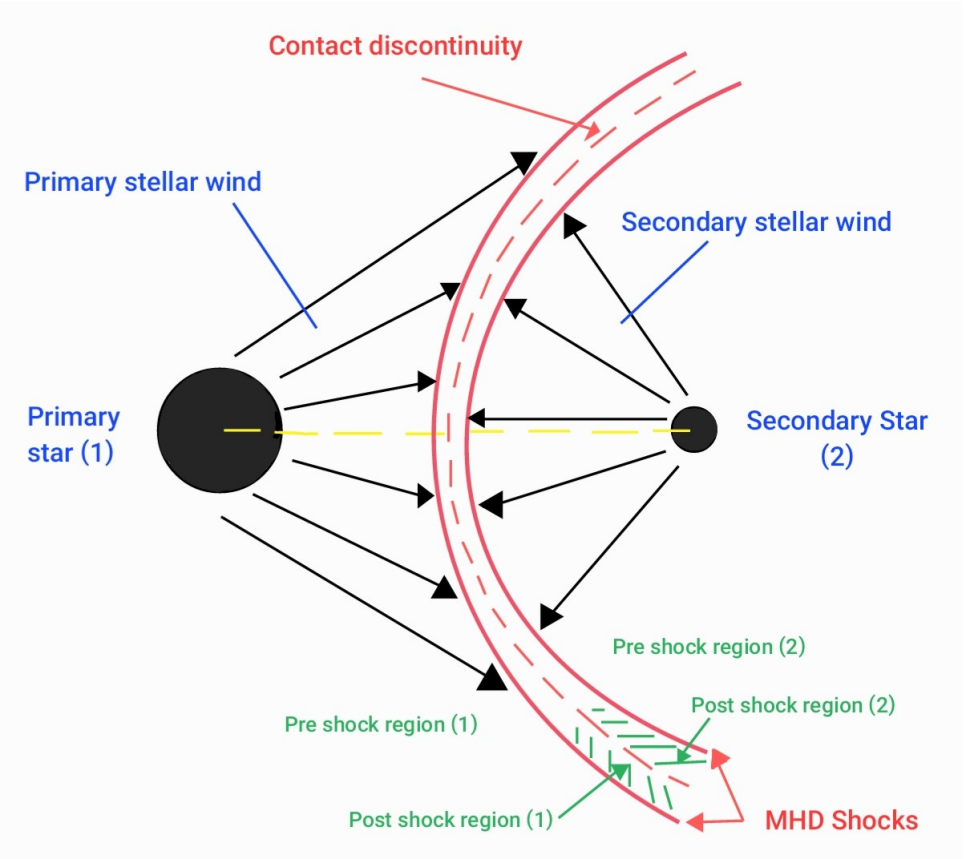

Figure 1.3: Geometry of a CWB region

The geometry of the interaction region notably depends on the strength of the winds. As shown in Fig. 1.3, the primary star's wind is stronger than the one produced by the secondary star, so the WCR will be curved and located closer to the secondary star. If the two stars were perfectly identical with the same winds, the contact discontinuity would be a straight region (without curvature) at an intermediate distance from the two stars, with shocks on either side.

As shown in Fig. 1.3, the whole wind is not implied in the collision region. The part of the wind that is not directed towards the other star will indeed not collide with the other wind. This entails that not all the fraction of bolometric luminosity converted into wind kinetic power wind will contribute to the shock. Only a part of this kinetic power will supply wind-wind interaction processes. Furthermore, this fraction of injected kinetic power will depend on the geometry of the WCR and the angular distance measured with respect to the line of center (imaginary straight line between the centers of the two stars). Indeed, velocity vectors of the winds can be split into two components, the normal or perpendicular component to the shock and the tangential component. Only the normal component will contribute to the injection of energy because it is directed towards the interaction region. In this way, in the case of a part of the interaction region with less curvature, the normal component will be dominant so the energy input will be higher. Conversely, in a more curved region, the tangential component is more important and the energy input is less. The contribution of the injected kinetic energy into this collision region comes from both stars and due to this geometry effect, the main contributor is not necessarily the primary star.

1.3.2 Diffusive Shock Acceleration

It was highlighted in Sect. 1.3.1 that shock physics is an important feature of the wind interaction in a binary system of massive stars. This is the reason why in this section, the physics behind hydrodynamic shocks and the associated process of Diffusive Shock Acceleration (DSA) will be detailed.

In the first place, the basics of shock physics will be presented based on De Becker and Van Grootel (2022). A shock is a discontinuity between an upstream and a downstream region (before and after the shock). These regions can be described with parameters such as the temperature, the pressure, or the density. The separation between these two regions is called a jump where the different parameters change significantly. As already mentioned above, the shocks considered here are collisionless as well as non-relativistic (shock velocities are significantly lower than the speed of light). An important quantity that must be defined is the Mach Number (M_u). It is a dimensionless number that qualitatively represents the strength of a shock. It can be defined as the following (with the lower indices u and d meaning the upstream the downstream region, respectively):

$$M_u = \frac{u_u}{a_u} = \left(\frac{\rho u_u^2}{\gamma P_u}\right)^{1/2} \tag{1.6}$$

γ is the adiabatic index, which is equal to 5/3 in the case of a monoatomic gas. a_u is the sound speed in the upstream region and it may be written as:

$$a_u = \sqrt{\frac{\gamma P_u}{\rho_u}} \tag{1.7}$$

One condition that determines whether a shock can form is that the upstream flow must be supersonic which translates as $M_u > 1$. Besides, it can be relevant to define the compression ratio χ which is the ratio between the downstream and the upstream density, or equivalently, the ratio between the upstream and downstream velocity:

$$\chi = \frac{\rho_d}{\rho_u} = \frac{u_u}{u_d} \tag{1.8}$$

Shock physics may arise in a variety of environments leading to different types of shocks as adiabatic shocks, radiative shocks, magnetohydrodynamic shocks,... In the context of this work, the focus will be set on strong adiabatic shocks assuming monoatomic gas. Adiabatic shocks mean that there is no exchange of energy (gain or loss) with the environment. Strong shocks, also called high Mach number shocks, involve M_u much greater than 1. This assumption leads to a compression ratio $\chi = 4$ and the density and velocity ratios may be written as $\rho_u = \frac{1}{4}\ \rho_d$ and $u_u = 4\ u_d$. Moreover, the pressure and the temperature in the post-shock region are given by:

$$P_d = \frac{3}{4}\rho_u u_u^2 \tag{1.9}$$

$$T_d = \frac{3}{16}\frac{m}{k}u_u^2 \tag{1.10}$$

with k the Boltzmann's constant, and m the mean mass per particle. The last equation supports one of the statements shown in Sect. 1.3, about the conversion of kinetic energy into thermal energy in the post-shock region.

Since the basics of shock physics have been reviewed, the diffusive shock acceleration or DSA process can be now explained. This process allows the acceleration of charged particles up to relativistic velocities by magneto-hydrodynamic shocks, where the magnetic field plays an important role. The general idea behind DSA is the transfer of mechanical energy from the shock to the kinetic energy of charged particles, leading to their acceleration.

Some assumptions are frequently expressed when talking about DSA, in particular in the framework of colliding-wind binaries:

- Non-relativistic shock
- High Mach number
- Adiabatic
- Collisionless
- Magnetohydrodynamic

The last three items are mandatory to have DSA, unlike the first two which are assumed to simplify the context or to make it more appropriate to the topic of this master thesis. Considering a magnetohydrodynamic shock implies the presence of a magnetic field, with both ordered and turbulent components.

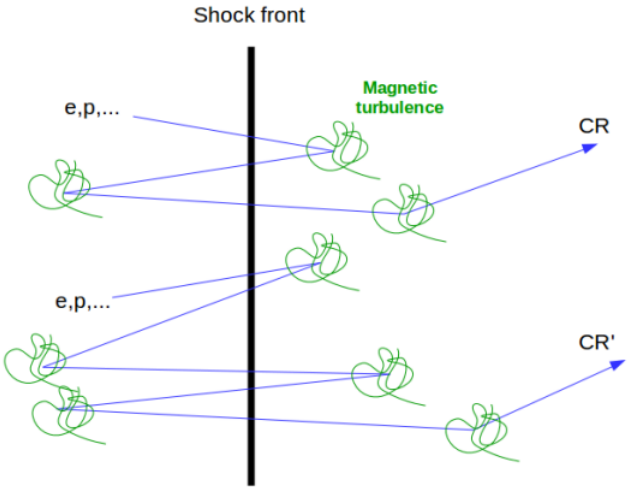

Figure 1.4: Illustration of the Diffusive Shock Acceleration mechanism. Taken from De Becker and Van Grootel (2022)

The DSA process is illustrated in Fig. 1.4. A high-energy charged particle (proton, electron,...) will cross the shock front and then will be isotropically scattered by the scattering centers, which are magnetic turbulences. "Isotropically" means that these particles are allowed to cross back the shock front or leave the acceleration region. These spots of magnetic turbulence are present on both sides of the shock front. In this way, these highly energetic charged particles may cross back and forth.

Considering a charged particle with an energy E in the downstream region, the shock front and upstream region approach at a velocity $V = u_u - u_d = 3/4\ u_u$ from its point of view. V is called the shock velocity jump and represents the relative velocity between the two regions. Let's adopt the point of view of a particle initially in the upstream region, and moving to the downstream region. This particle will "see" the downstream flow approaching with a velocity V. The particle will cross the shock front and will be scattered by the magnetic turbulence that is co-moving with the downstream flow. In the case in which the particle is scattered back in the direction of the shock front, the particle that is now downstream will "see" again the upstream flow approaching with a velocity "V", and it will cross again the shock front, and so on. The relative gain of energy comes from the particle bouncing back and forth on always approaching scattering centers on both sides of the shock front. In other words, the particle will be reflected like a ball in a region delimited by two approaching walls, therefore transmitting energy to the particle at every reflection. It can be shown that after one cycle (upstream $\rightarrow$ downstream $\rightarrow$ upstream) the relative energy gain is finally :

$$\frac{E'' - E}{E} = \frac{\Delta E}{E} \propto \frac{V}{c} \tag{1.11}$$

It is clear from the above equation that the relative energy gain of the particle will be higher for greater velocity jumps V.

This successive crossing thus explains the energy gain of the charged particles and thus, their acceleration. The particle is likely to undergo a lot of acceleration cycles as a result of the potential back-scattering to the shock front, hence the iterative nature of the process. An important aspect of DSA is the escape probability that affects every scattering by magnetic turbulence: at every iteration, particles may leave the acceleration region and thus stop benefiting from the energy gain. This results in a power law distribution of relativistic particles:

$$N(E)dE = KE^{-p}dE \tag{1.12}$$

with K being the normalization parameter of the population of relativistic particles. Since p is the index of the power law distribution of particles and is preceded by a minus sign, it implies a greater population of particles at lower energies than at higher ones. It means that most of the particles don't stay for a long time in the acceleration region and don't gain a lot of energy. It is important to note that this power law distribution results from the iterative nature of the process and the systematic probability of escaping at each crossing. Finally, the index of the power law is dependent on the compression ratio of the shock as follows:

$$p = \frac{\chi + 2}{\chi - 1}. \tag{1.13}$$

In the context of our assumptions, the compression ratio is equal to 4 and thus $p = 2$.

1.3.3 Particle-Accelerating Colliding-Wind Binaries

In previous subsections, it was stated that in a binary system of massive stars, their winds collide and produce strong shocks at the WCR. In this context, the DSA mechanism may take place, leading to the acceleration of charged particles. The combination of these processes gives rise to the concept of Particle-Accelerating Colliding-Wind Binaries (PACWBs). A PACWB is a particular subset of CBWs in which the DSA process occurs and accelerates charged particles in the wind up to relativistic velocities. These particles

may eventually leave the acceleration region (Fig. 1.4) and become a part of the Galactic Cosmic Ray (CR) population. Even though most Galactic CRs are accelerated by the shocks of young supernova remnants, PACWBs should provide a contribution as well (De Becker et al., 2017).

As was previously mentioned, the consideration of the energy budget in this kind of system is important. The energy budget for a PACWB is represented in Fig. 1.5. The numbers beside the arrows represent the order of magnitude of the energy transfer.

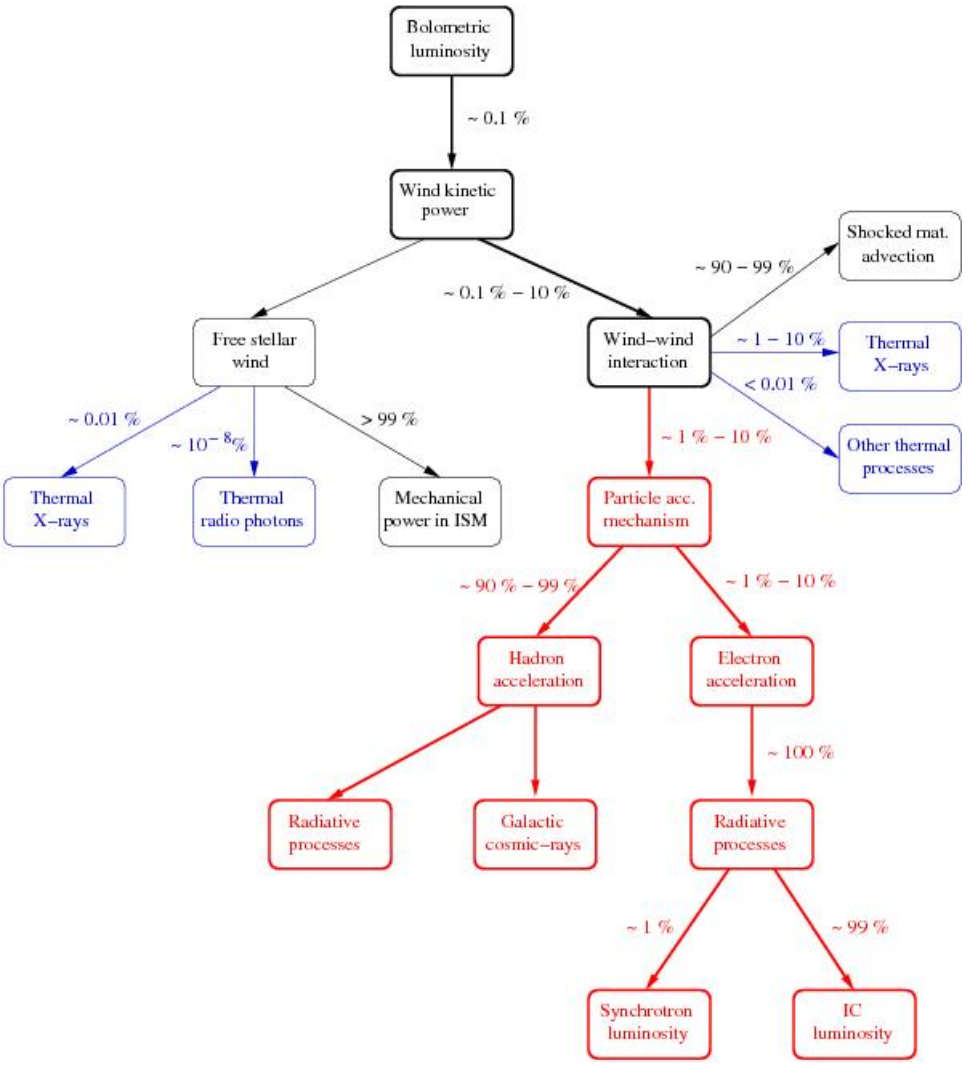

Figure 1.5: Energy budget in a PACWB. The thermal processes are in blue and the non-thermal processes are in red. Taken from De Becker and Raucq (2013).

At the beginning, the bolometric luminosity is partially transferred as wind kinetic power (Section 1.2.2). Then, while the kinetic power itself drives some thermal emission by the wind, a percentage of this power will feed the interaction between the winds (Section 1.3.1). The wind collision produces both thermal and non-thermal emissions. The non-thermal emission comes from the relativistic particles (hadrons and electrons) accelerated through the DSA process. The accelerated hadrons (protons) may interact with the surrounding material producing pions. γ-ray emission arises from the decay of these pions (De Becker

and Raucq, 2013). Two main different types of emission emerge from the acceleration of electrons. The main part of the energy goes to the Inverse Compton (IC) scattering process involving UV/visible stellar photons. Through the IC process, photons are re-emitted at a higher energy leading to X-ray emission (De Becker and Raucq, 2013). The remaining part of the energy is converted into radio emission through the radiation of synchrotron luminosity.

PACWBs are a subset of CWBs. This raises the question: should all CWBs be classified as PACWBs, or what proportion of CWBs are actually PACWBs? Essentially, how prevalent is particle acceleration in CWBs? To classify a CWB as a PACWB, certain criteria must be met, such as the presence of non-thermal emission (γ-ray, NT X-ray, radio synchrotron). These emissions are indeed the direct consequence of the acceleration of particles in a CWB. There are different cases, such as ηCar, which was identified as a PACWB thanks to its non-thermal hard X-ray and γ-ray emission, even though it lacks a radio counterpart. This contrasts with most PACWBs, which have been identified primarily by their non-thermal radio emission only (De Becker and Raucq, 2013).

All the identified PACWBs are grouped into a catalog (De Becker and Raucq, 2013) that initially included 43 objects (*List A* in De Becker and Raucq (2013)). Moreover, a second list (*List B* in De Becker and Raucq (2013)) is provided including objects whose non-thermal emissions are not clear. However, the catalog dates from 2013. Since then, several objects have been added to the PACWB list, which includes now 50 objects. The updated PACWB catalog can be found at the following address: `https://www.astro.uliege.be/~debecker/pacwb/`.

The catalog encompasses systems made of massive stars such as O-type stars, WR stars, and even early B-type stars. Because of this variety, the parameter space of PACWBs deserves some attention. It was shown in De Becker and Raucq (2013) that the mass-loss rates and terminal velocities are widespread. The former goes from 10^{-8} to $10^{-4}\,M_\odot$/year with WR displaying the higher values. The latter takes values between 500 and 3500 km/s. These systems are mainly binary, but a few of them are of higher multiplicity. As a matter of fact, the multiplicity of some systems identified as PACWBs is not fully known, opening up the possibility that they could be either binary or multiple systems. The period of the PACWB is given in the catalog, when possible. The lowest value is a few weeks, while the highest is 10^5 days, covering several orders of magnitude (De Becker and Raucq, 2013). It should be noted that half of the objects in the catalog are WR stars. Yet the number of these stars in the Milky Way is about 1200 ± 100 (Crowther, 2015) for at least 10^9 stars in total. This fraction of WR stars in identified PACWBs may be due to an observational bias. Due to their higher luminosity in comparison to O-type stars, they have more energy which can be translated into more non-thermal emission. Thus, WR stars are more readily identified as PACWBs compared to O-type stars, which explains their over-representation in the catalog.

1.4 Target and objectives

The target at the center of this work is WR 147. Its coordinates are RA 20 36 43.64 and δ +40 21 07.6. WR 147 is a confirmed binary system formed by a WN8h star, and the companion is either a BO.5V (Williams et al., 1997) or a 08-09 VIII (Wallace et al., 1999) star (it will later be referred to as an OB star) and both of them display winds. The period associated with this system is of the order of 1300 years (Rodríguez et al., 2020b). The system was identified as a PACWB thanks to its strong non-thermal (synchrotron) radio emission.

Since WR 147 is one of the brightest WR stars in the radio domain, it is a valid target to investigate its radio emission. In particular, its brightness constitutes a relevant feature to address the main scientific questions at the core of this Master thesis:

- *What can we learn from the multi-band investigation of its radio spectrum?*

  Indeed, most radio studies of PACWBs are based on flux measurements integrated over wide bands. However, more detailed studies with a better spectral resolution are mainly lacking.

- *How can a more detailed investigation of the lower frequency radio spectrum improve our understanding of the physics at work in these systems?*

  As will be explained in Chapter 2, the low frequency part of the synchrotron spectrum is most of the time more difficult to interpret. It can be affected by various physical processes that are mostly poorly constrained.

To do so, we will use data obtained with the Jansky Very Large Array (JVLA) interferometer (Sect. 3.2). The radio emission will be analyzed in two different spectral bands. Besides, each frequency band will be subdivided into smaller bands allowing a more precise intra-band analysis. Several scenarios for the observed emission will be envisaged according to the behavior of the spectrum.

In this first chapter, the general physics of massive stars was presented, with a particular focus on their winds and multiplicity. We introduced the concepts of CWBs and PACWBs. The main criteria to identify a PACWB is the non-thermal radio emission highlighting the acceleration of electrons in the collision region. Radiative processes (thermal and non-thermal) in the radio domain will be presented in Chapter 2 along with a more detailed explanation of radio emissions expected from massive stars. In Chapter 3, basic concepts of interferometry and the telescope used in this work (the JVLA) will be introduced, as well as the data collection and methods that were used. Then, the results and discussions will be given in Chapters 4 and 5 respectively. The thesis will end with a conclusion and several prospects in Chapter 6.

Chapter 2

Radio Astrophysics

2.1 Radiative processes

The content of this section was mostly taken from the Radio astrophysics course (De Becker, 2022).

The beginning of radio astrophysics can be traced back to the early 20th century thanks to Karl Jansky, who detected an unknown periodic radio signal coming from a celestial object, which turned out to be radio emission from the Galactic center. This first discovery was the trigger to start studying astrophysics in the radio domain.

Some of the important and early discoveries in radio astrophysics are :

- The observation of the hyperfine structure emission from neutral hydrogen at 21 cm
- The mapping of the structure of the Milky Way
- The discovery of pulsars by Jocelyn Bell
- The detection of the Cosmic Microwave Background

2.1.1 Fundamentals of radio astrophysics

Let us start by defining some relevant quantities, assumptions, and major concepts.

First, one of the main quantities in radio astrophysics is the specific intensity (also called spectral brightness). It is defined as :

$$I_\nu = \frac{E}{cos\theta \, d\sigma \, d\Omega \, dt \, d\nu} \tag{2.1}$$

This equation can be interpreted as the amount of energy in the interval $[\nu, \nu + d\nu]$ crossing a unit surface area ($d\sigma$) under a given angle (θ) per unit of time (dt) and within a given solid angle ($d\Omega$). In the MKS system the units are $\mathrm{J\,s^{-1}\,m^{-2}\,Hz^{-1}\,sr^{-1}}$ and in the cgs system they are $\mathrm{erg\,s^{-1}\,cm^{-2}\,Hz^{-1}\,sr^{-1}}$. From the specific intensity, two other significant quantities can be defined. The first one is the total intensity :

$$I = \int_0^\infty I_\nu \, d\nu \tag{2.2}$$

The second one is the flux density :

$$S_\nu = \int_{Source} I_\nu \, cos\theta \, d\Omega \tag{2.3}$$

It might be reduced as follows if small angles are considered:

$$S_\nu = \int_{Source} I_\nu \, d\Omega \tag{2.4}$$

By looking at the units of this last quantity ($\mathrm{erg\,s^{-1}\,cm^{-2}\,Hz^{-1}}$) it can be seen that it depends on the distance d as $S_\nu \propto d^{-2}$.
In radio astrophysics, it is usual to express flux densities in a specific unit called $Jansky$ (Jy):

$$1 \; Jy = 10^{-23} \, \mathrm{erg\,s^{-1}\,cm^{-2}\,Hz^{-1}}$$

Secondly, in the radio domain, one big assumption is used: the Rayleigh-Jeans limit. This is valid for representing the low-frequency part of the Planck function, which is the function that defines the continuum spectrum of a black body at a given temperature T. At the second order, it leads to the following simplification in the function:

$$B_\nu = \frac{2\,h\,\nu^3}{c^2} \frac{1}{e^{h\nu/kT} - 1} \tag{2.5}$$

$$\approx \frac{2\,\nu^2}{c^2} kT \tag{2.6}$$

with B_ν having the same units as specific intensities, h the Planck's constant and k the Boltzmann's constant. This simplification is especially valid in the low-frequency regime, hence its widespread use in the radio domain. From this relation, the brightness temperature can be defined:

$$T_B = \frac{c^2}{2\,k\,\nu^2} B_\nu^{RJ} \tag{2.7}$$

This relation is applicable in the Rayleigh-Jeans limit and represents the temperature that a black body radiating the same energy as the measured radio source would have.

Thirdly, the radio synchrotron emission covered in this work is produced by charged particles that undergo some acceleration under the influence of a specific force (of electric or magnetic origin, depending on the process). In this context, the power radiated by an accelerated charged particle (with an electric charge q) is given by Larmor's formula :

$$P_{rad} = \frac{2q^2\,\dot{v}^2}{3\,c^3} \tag{2.8}$$

This formula is only valid in the rest frame of the particle. It can be also inferred that the radiation is dipolar. This means that the radiation pattern exhibits a doughnut shape, i.e., there is no radiation along the acceleration direction and it shows its maximum along the direction perpendicular to the acceleration direction.

Finally, the last important consideration is the distinction between thermal and non-thermal processes. When the velocity distribution of the particles has the following form:

$$f(v) = \frac{4v^2}{\sqrt{\pi}} (\frac{m}{2kT})^{3/2} \, exp(-\frac{m\,v^2}{2kT}) \tag{2.9}$$

it is said to be Maxwellian and the radiative process to be thermal. This equation can be seen as the probability of finding a particular velocity v in an interval between v and $v + dv$.
In comparison, when the distribution of particles according to their velocity does not follow a Maxwell-Boltzmann distribution, we talk about a non-thermal radiative process. In this case, the emitting particles are relativistic and follow a power law distribution

$$N(E) \propto E^{-p} \tag{2.10}$$

where $N(E)$ is the number density of relativistic particles between energy E and $E + dE$ and p is the particle index of the power law distribution. These particles may include particles accelerated through the DSA process. Thus, Eq. 1.12 and Eq. 2.10 represent the same phenomenon with p the spectral index given by Eq. 1.13.

2.1.2 Free-free emission

Free-free (FF) emission, also called Bremsstrahlung radiation, results from the acceleration of an electron by the Coulomb force. Indeed, in an ionized medium, electrons and ions are moving around each other. The electrons coming closer to an ion undergo a Coulomb force, leading to their acceleration. As seen above, this acceleration will lead to the emission of electromagnetic radiation given by Larmor's formula (Eq. 2.8). The temperature of the astrophysical environments known to produce thermal FF radio emission is of the order of 10^4 K.
The focus of this interaction is set on the electrons because of their lower mass. The ratio between the mass of a proton and an electron is $\frac{m_p}{m_e} \sim 1800$ so the acceleration ratio is $\frac{\dot{v}_p}{\dot{v}_e} = \frac{m_e}{m_p} \sim 5.5\,10^{-4}$. Putting this in Larmor's formula, we get $\frac{P_p}{P_e} = (\frac{\dot{v}_p}{\dot{v}_e})^2 \sim 3\,10^{-7}$. For this reason, only the radiative emission from the electrons will be taken into account. The Bremsstrahlung radiation process might be either thermal or non-thermal according to the energy of the particle involved (thermal or non-thermal population). However, in the radio domain, only thermal Bremsstrahlung is relevant, as the non-thermal one produces high-energy photons.

First and foremost a simple example will be presented before looking at the more complex emission from stellar winds. It consists of free-free thermal radio emission from an ionized cloud. The main equations will be presented as well as the general spectrum of this emission and the different regimes.

In this general case, the emission process is presented but the self-absorption process (also called free-free absorption), when the emitted photon is absorbed by an electron in the same medium, must also be included. The main equation governing these processes is the radiative transfer equation:

$$\frac{dI_\nu}{ds} = \epsilon_\nu^{ff} - \kappa_\nu^{ff} I_\nu \tag{2.11}$$

The different terms can be detailed :

- ϵ_ν^{ff} is the **free-free emissivity** which is proportional to :

$$\epsilon_\nu^{ff} \propto n_e\, n_i T^{-1/2}\, ln\Lambda \tag{2.12}$$

  With n_e and n_i the number density of electrons and ions respectively and $ln\Lambda$ the Coulomb logarithm that will be detailed below.

- κ_ν^{ff} is the **absorption coefficient**, which has the following main dependencies:

$$\kappa_\nu^{ff} \propto \frac{1}{T^{3/2}}\,\nu^{-2} n_e\, n_i\, ln\Lambda \tag{2.13}$$

- I_ν is the **specific intensity**.
- ds is the **infinitesimal distance element** along the optical path.

A supplementary assumption concerns the cloud. It is assumed to be homogeneous, meaning that the electron and ion number densities are homogeneous in the cloud as well as the temperature along the optical path. This assumption implies that κ_ν^{ff} is constant along the line of sight. Therefore the optical depth may be defined as follows:

$$\begin{aligned}\tau_\nu &= \int \kappa_\nu^{ff} ds \\ &= \kappa_\nu^{ff} \int ds \\ &= \kappa_\nu^{ff} L\end{aligned} \tag{2.14}$$

The optical depth might be defined as the capability of a given medium (here the cloud) to attenuate light, and L is the total depth of the cloud.
Given Kirchoff's identity:

$$\kappa_\nu^{ff} = \frac{\epsilon_\nu^{ff}}{B_\nu(T)} \tag{2.15}$$

it is possible to write the radiative transfer equation as:

$$-\frac{dI_\nu}{d\tau_\nu} = I_\nu - B_\nu \tag{2.16}$$

The general solution to this equation is:

$$I_\nu = I_\nu(0)e^{-\tau_\nu} + B_\nu\,(1 - e^{-\tau_\nu}). \tag{2.17}$$

Given that the cloud is considered to have no back illumination ($I_\nu(0) = 0$), and considering the Rayleigh-Jean limit, this simplification leads to:

$$I_\nu = \frac{2kT}{c^2}\,\nu^2\,(1 - e^{-\tau_\nu}) \tag{2.18}$$

The optical depth is proportional to the absorption coefficient. Taking into account the dependency of the absorption coefficient with the frequency, the specific intensity can be split into two regimes :

- If **low frequencies** are considered:

$$\tau_\nu \propto \kappa_\nu^{ff} \propto \nu^{-2} \rightarrow \tau_\nu >> 1 \rightarrow e^{-\tau_\nu} \sim 0 \tag{2.19}$$

$$I_\nu = \frac{2kT}{c^2}\nu^2 \tag{2.20}$$

- If **high frequencies** are considered:

$$\tau_\nu \propto \kappa_\nu^{ff} \propto \nu^{-2} \rightarrow \tau_\nu << 1 \rightarrow 1 - e^{-\tau_\nu} \sim \tau_\nu \tag{2.21}$$

$$I_\nu = \frac{2kT}{c^2}\nu^2\tau_\nu \tag{2.22}$$

On the one hand, a regime dominated by free-free absorption at low frequencies and on the other hand an optically thin regime at high frequencies. The former has a clear dependence on the frequency as ν^2 and the latter has no clear dependence on the frequency considering the frequency dependence for the optical depth. Therefore, the free-free emission spectrum (specific intensity, I_ν, as a function of frequency) has the morphology presented in the left panel of Fig. 2.1.

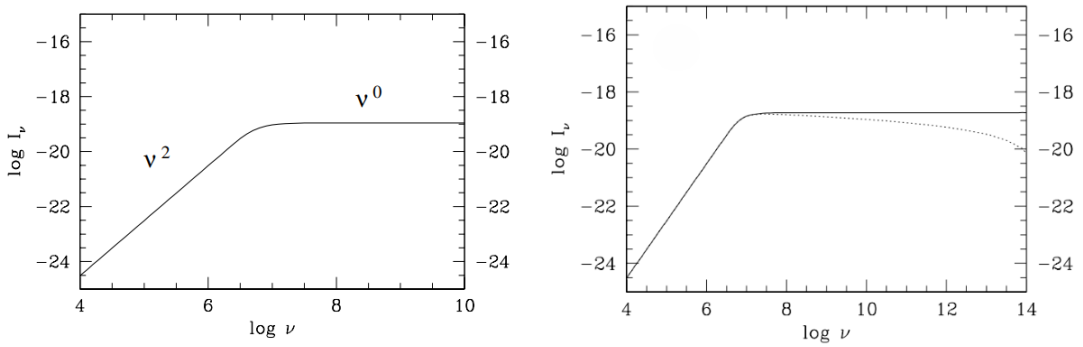

Figure 2.1: Free-free emission spectrum of a homogeneous ionised cloud; left panel: without Coulomb logarithm dependence ; right panel: with Coulomb logarithm dependence (De Becker, 2022).

A clear transition between two regimes can be seen in Fig. 2.1. This transition occurs at a specific cut-off frequency, that corresponds to $\tau_\nu = 1$. This frequency can be obtained thanks to the definition of the optical depth and the full expression of the absorption coefficient. For instance, using parameters corresponding to an HII region, i.e., $n_e = n_i = 200\,\mathrm{cm}^{-3}$, $L = 10^{16}$ cm and $T = 10^4$ K, the value of the cut-off frequency is 40 MHz meaning that above this value (corresponding to the optically thin regime) the spectrum is nearly flat.

A final comment can be made on the free-free emission spectrum. As mentioned above, the spectrum in the optically thin part is nearly flat and has no dependence on the frequency. However, in the absorption coefficient expression, there is the Coulomb logarithm ($ln\Lambda$) term which is the logarithm of the ratio between the maximum and the minimum impact parameter (the distance of closest approach between two interacting particles) for electrons passing near ions in the ionized cloud. This parameter has a slight dependency on the frequency, i.e., $ln\Lambda \propto \nu^{-0.1}$. If it is taken into account, it induces a slight decrease in the optically thin part of the spectrum as a function of frequency. This effect is seen in the right panel of Fig. 2.1 with the dotted line.

2.1.3 Synchrotron emission

In the simplest view, synchrotron radiation is produced by a charged particle (here, a relativistic electron) moving in a magnetic field. The magnetic force acting on the electron will induce a helical motion of the particle. This particle will undergo acceleration and lose energy through the emission of synchrotron radiation.

A radiative process triggered by a magnetic force may involve thermal, mildly relativistic as well as relativistic electrons. The denomination of the radiation will change according to the energy of the electron. In the case of thermal, non-relativistic electrons the radiation

is called cyclotron or gyroresonance radiation. In comparison, gyrosynchrotron radiation is associated with mildly relativistic electrons (with a Lorentz factor, γ, around 2 or 3). In this work, we deal with highly relativistic electrons, and hence, synchrotron radiation.

A particular aspect of synchrotron radiation is the relativistic beaming due to the relativistic nature of the electrons involved. Indeed, from the point of view of an observer not co-moving with the relativistic electron, this radiation will be highly beamed in the direction of motion of the emitting particle.

In the case of an astrophysical source, a whole population of relativistic electrons is considered. As explained in a previous section, the population of relativistic electrons is distributed as a function of energy:

$$N(E)dE = KE^{-p}\,dE \tag{2.23}$$

where $N(E)\,dE$ is the number (or number density) of relativistic electrons between energies E and $E + dE$. The factor K present in the distribution is a normalisation parameter of the population and p is the index of the power law distribution of the relativistic particles. It can be shown that the synchrotron emissivity for this distribution of electrons is a power law as well as a function of photon frequency. The main dependencies of the synchrotron emissivity are:

$$J(\nu) \propto \frac{K}{p+1}\, B^{-\frac{p-1}{2}}\, \nu^{-\frac{p-1}{2}} \propto \nu^{-\alpha} \tag{2.24}$$

with B the magnetic field and α the spectral index of the photon distribution, that depends on the electron index p: $\alpha = \frac{p-1}{2}$.
In the case of a DSA described in Sect. 1.3 (high Mach number adiabatic shocks and monoatomic gas), the electron index p is equal to 2 which leads to $\alpha = 0.5$. The frequency dependence of the synchrotron emissivity is then given by $J(\nu) \propto \nu^{-0.5}$.

The synchrotron spectrum of an astrophysical source may not only display pure synchrotron emission but also a self-absorbed part. Indeed, a radio photon might be absorbed by a relativistic electron in the same plasma where it was emitted. This process is called Synchrotron Self-Absorption (SSA). It arises when a synchrotron photon transfers all its energy to a relativistic electron in a magnetic field.
The absorption coefficient for SSA depends on various parameters (with the same meaning as the previous equations) as expressed below,

$$\chi(\nu) \propto K\, B^{\frac{p+2}{2}}\, \nu^{-\frac{p+4}{2}}. \tag{2.25}$$

Spectrum and spectral indices

As it was carried out for Bremsstrahlung, a simple example will be used to express the shape of the synchrotron spectrum and its dependency on the frequency.

In this simple case, let's consider a piece of material (emitting and absorbing) of a thickness l. Once again, similarly to the ionized cloud, the radiative transfer equation is the starting point. In this case, it is given by

$$\frac{dI_\nu}{dx} = \frac{J(\nu)}{4\pi} - \chi(\nu)\, I(\nu) \tag{2.26}$$

where $J(\nu)$ is the emissivity per unit volume, $\chi(\nu)$ is the average absorption coefficient and $I(\nu)$ is the specific intensity.
The associated solution is:

$$I_\nu = \frac{J(\nu)}{4\pi\,\chi(\nu)}\left(1 - \exp(-\chi(\nu)l)\right) \tag{2.27}$$

Two distinct regimes might be also inferred from this solution depending on the "amplitude" of the absorption.

- **Optically thin regime**:
  The absorption is considered to be weak. Regarding Eq. 2.14 which is also valid in this case, the optical depth is said to be low. In this way, the argument in the exponential is small in Eq. 2.27 and may be expressed as a Taylor development.

$$I_\nu = \frac{J(\nu)\,l}{4\pi} \tag{2.28}$$

  Taking into account the frequency dependence of the emissivity (Eq. 2.24), the dependence of the synchrotron spectrum on the frequency is then :

$$I_\nu = \nu^{-\frac{p-1}{2}} \tag{2.29}$$

- **Optically thick regime**:
  On the contrary to the other regime, the absorption is strong which leads to the cancellation of the exponential term in Eq. 2.27.

$$I_\nu = \frac{J(\nu)}{4\pi\,\chi(\nu)} \tag{2.30}$$

  Considering the frequency dependence for the absorption coefficient (Eq. 2.25) and the emissivity coefficient (Eq. 2.24) in Eq. 2.27, it leads to the following total dependence:

$$\begin{aligned} I_\nu &\propto \nu^{-\frac{p-1}{2}}\,\nu^{\frac{p+4}{2}} \\ &\propto \nu^{\frac{-p+1+p+4}{2}} \\ &\propto \nu^{5/2} \end{aligned} \tag{2.31}$$

The resulting broadband spectrum is represented in Fig. 2.2.

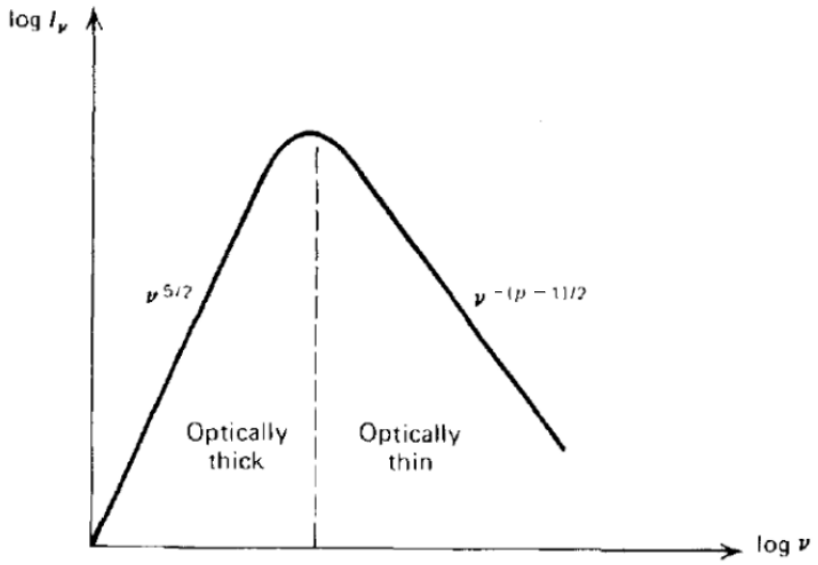

Figure 2.2: Spectrum of synchrotron emission (specific intensity as a function of frequency) of an emitting and absorbing material with the two distinct regimes. Taken from De Becker (2022).

As with free-free emission, there is a clear transition between the two regimes that arises at the turnover frequency; below this value, SSA is considered to be significant. The value of this critical frequency can be found at the optical depth equal to 1. Starting with Eq. 2.14, it can be expressed using the equation for the absorption coefficient (Eq. 2.25). The SSA turnover frequency is then given by:

$$\nu_{SSA} \propto (K\, B^{\frac{p+2}{2}}\, l)^{\frac{2}{p+4}}. \tag{2.32}$$

It depends on the normalization parameter of relativistic electrons K, the local magnetic field B, the size of the emitting/absorbing region l, and the electron index of the relativistic electron distribution p.

Energy equipartition

It is always relevant to address astrophysical sources in terms of energetic considerations. When talking about synchrotron sources, two main reservoirs have to be considered: the magnetic energy and the energy in relativistic particles (including mainly electrons and protons). The sum of these reservoirs constitutes what is conventionally called the total energy. It can be written as:

$$E_{tot} = E_e + E_p + E_B \tag{2.33}$$

with the different terms defined as:

$$E_p = k\, E_e \tag{2.34}$$

$$E_e = L\, B^{-3/2} C_3 \tag{2.35}$$

$$E_B = U_B\, \phi\, V = \frac{B^2}{8\pi}\, \phi\, V \tag{2.36}$$

where U_B is the magnetic energy density, ϕ is the volume filling factor taking its values between 0 and 1, C_3 is a factor dependent on the spectral index α and on the considered

frequency range, and k is the fraction between the proton energy and the electron energy. As a general simplification, it can be assumed to have a spherical emitting volume with a radius R with an active fraction ϕ in the emission process. The magnetic energy becomes $E_B = \frac{B^2 \phi R^3}{6}$ and then the total energy is :

$$E_{tot} = (1+k)\, L\, B^{-3/2}\, C_3 + \frac{B^2 \phi R^3}{6}. \tag{2.37}$$

It can be seen that both terms depend on the magnetic field. There is a value of the magnetic field which minimizes the total energy. Taking the derivative of the expression (Eq. 2.37) as a function of B and setting it to 0, the expression of the magnetic field at minimum energy is then:

$$B_{min} = \Big(\frac{9}{2}\frac{(1+k)C_3 L}{\phi R^3}\Big)^{2/7} \tag{2.38}$$

The term $1+k$ takes values between 10 and 100 and is not always easy to determine, but the power 2/7 damps this accuracy problem. Observations determine the luminosity L.

This expression of the magnetic field at minimum energy can be replaced into the expressions of the two energy reservoirs, and the main outcome is

$$E_B = \frac{3}{4} E_{part}. \tag{2.39}$$

This can be interpreted as "at minimum energy, the magnetic and relativistic particle energy reservoirs are very close to equipartition". This is the *equipartition theorem*. These results can be shown in Fig. 2.3.

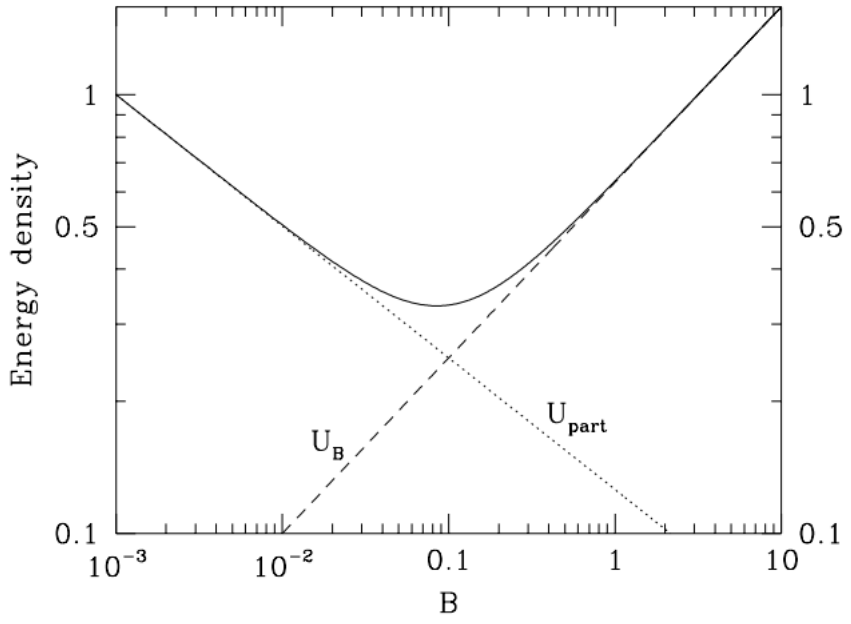

Figure 2.3: Energy equipartition and energy densities of the two reservoirs; the solid line represents the total energy density. Taken from De Becker (2022).

This situation of (almost) equipartition results from the assumption of the minimum energy state of the system. It can be used to estimate the strength of the magnetic field in the synchrotron emission region.

2.1.4 General spectrum and turnover processes

The free-free spectrum and the non-thermal radio emission spectrum were presented above. However, the observed spectrum of a radio source might include both non-thermal and thermal components of the emission. The different values of the slope in the spectrum correspond to the distinct nature of the emission.

Some processes may affect the spectrum of the synchrotron emission and lead to a turnover in the low-frequency domain. The first process was already addressed above: **synchrotron self-absorption**. This mechanism arises below a specific critical frequency that is expressed in Eq. 2.32. This process was introduced in Sect. 2.1.3.

The second turnover process worth discussing is the **free-free absorption** by thermal electrons. More precisely, synchrotron emission absorbed by a screen of matter between the source and the observer (*foreground free-free absorption*) will have the shape:

$$S_\nu \propto \nu^{-\alpha} e^{-\tau_\nu} \tag{2.40}$$

Eq. 2.40 expresses the attenuation of the flux due to thermal electrons in a plasma. The attenuation factor is quantified by the optical depth (τ_ν) for free-free absorption, which was introduced in Sect. 2.1.2. The optical depth is much higher at low frequencies, making free-free absorption an efficient turnover process in the low-frequency part of the radio spectrum. Given the density of the plasma the stellar winds are made of, free-free absorption is the dominant turnover process at work in the radio spectrum of PACWBs (Benaglia et al., 2020; De Becker et al., 2017; Saha et al., 2023). This process will be considered with a high priority while interpreting our results in Chapter 4.

The third effect that could affect the emission spectrum at low frequencies is the **Razin-Tsytovitch effect**. It has to be noted that this is not an absorption process, but rather a process that inhibits the synchrotron radiation in a magnetized plasma.

The energy radiated by one relativistic electron through the synchrotron process is intimately related to relativistic beaming as briefly mentioned in Sect. 2.1.3. More precisely, the latter phenomenon consists of the narrowing of the radiation pattern from an emitting electron to a highly elongated beam of emission pointing to the direction of the velocity vector of the electron. This happens only for relativistic particles. A consequence of this beaming is a very strong enhancement of the emitted radiative energy. This can be illustrated by the following relation, which expresses the energy per unit angular frequency ($d\omega$) and per unit solid angle ($d\Omega$) received by a given observer from a radiating relativistic electron:

$$\frac{dE}{d\Omega\, d\omega} = \frac{q^2}{4\,\pi^2\, c} \left| \int_{-\infty}^{\infty} \frac{f(t)}{(1 - \mathbf{n}\,\beta)^3}\, dt \right|^2 \tag{2.41}$$

where q is the charge of the electron, β is the electron velocity vector in units of c ($\beta = v/c$), $\mathbf{n}$ is the unit vector pointing to the observer, and $f(t)$ is a function of retarded time.

This expression is valid for vacuum and emphasizes the importance of the denominator for a relativistic particle. Indeed, because of the beaming, the radiation reaches the observer provided the electron velocity vector is almost co-aligned with the line of sight. As a result, the scalar product $\mathbf{n}\,\beta$ tends to one ($\mathbf{n}$ is a unit vector, β is very close to one for a highly

relativistic electron, and the cosine between these two vectors is almost one). Consequently, the term $(1 - \mathbf{n}\,\beta)$ tends to zero. The energy received by the observer is thus substantially amplified by the $1/(1 - \mathbf{n}\,\beta)$ factor, especially considering it is raised to the equivalent of the 6th power. This amplification factor plays a key role in explaining the brightness of synchrotron sources.

However, in a magnetized thermal plasma, Eq. 2.41 has to be slightly modified. The term in brackets becomes $(1 - n_r\,\mathbf{n}\,\beta)$, where n_r is the refractive index of the medium. In a thermal plasma, n_r is lower than one. As a consequence, the content of the term commented on here deviates significantly from zero, and the amplification factor drops severely. The Razin-Tsytovitch effect is the name given to that strong inhibition of the synchrotron emission process in a magnetized thermal plasma.
This effect becomes important at frequencies where the refractive index is significantly lower than one, and this occurs only at sufficiently low frequencies. The specific frequency below which this process occurs is (Pacholczyk, 1970):

$$\nu_R \approx 20\,\frac{n_e}{B} \quad \text{(Hz)} \tag{2.42}$$

where n_e is the electron density and B, the local magnetic field (both expressed in cgs units).

2.2 Radio emission from a massive binary system

2.2.1 Thermal radio emission from the wind

The typical temperature of the plasma in the wind is about $10^4 K$. This temperature allows the winds to produce thermal free-free emission (Bremsstrahlung).

In the previous section, Sect. 2.1.2, the typical free-free emission from a uniform ionized hydrogen cloud was presented. However, the free-free emission from a massive star's wind is more complex. Thus, the solution of the hydrogen cloud is no longer valid in this more realistic case. The dependence on the frequency of the radio flux density of these expanding envelopes was established notably by Wright and Barlow (1975). Based on their development, the mass-loss rate can be expressed by Eq. 1.3 or, equivalently, by the following expression with r being the radial distance, n the number density of particles in the stellar wind, μ the mean molecular weight, m_H the mass of one hydrogen atom and v_∞ the terminal velocity of the wind:

$$\dot{M} = 4\pi\, r^2\, n\, \mu\, m_H\, v_\infty \tag{2.43}$$

Besides, it can be set:

$$A = \frac{\dot{M}}{4\pi \mu m_H v_\infty} \tag{2.44}$$

The flux density of the free-free emission from the expanding envelope is given by:

$$S_\nu = 1.342\, 2\pi\, \frac{B_\nu}{D^2} \left(\frac{\pi \kappa_\nu^{ff} \gamma A^2}{2}\right)^{2/3} \tag{2.45}$$

The frequency dependence can be highlighted by recalling Planck's function in the Rayleigh-Jean limit (Eq. 2.5), $B_\nu \propto \nu^2$) and the absorption coefficient (Eq. 2.13, $k_\nu^{ff} \propto \nu^{-2}$):

$$S_\nu \propto \nu^2 (\nu^{-2})^{2/3} \propto \nu^{2/3} \tag{2.46}$$

In the free-free emission subsection (Sect. 2.1.2) the Coulomb logarithm was introduced. If its dependency on the frequency is taken into account it results in:

$$S_\nu \propto \nu^{0.6} \tag{2.47}$$

The above dependence for an expanding envelope is quite different from the idealized case of a homogeneous ionized cloud in the optically thick regime for which it was $\propto \nu^2$.

A last important dependence concerns the mass-loss rates:

$$S_\nu \propto \dot{M}^{4/3} \tag{2.48}$$

Thanks to this equation, the mass-loss rate may be determined thanks to the flux density measure if the measured radio emission is only thermal emission.

One assumption that was made in this development is the homogeneity and the smoothness of the wind. However, stellar winds of massive stars may present some small-scale structures which are called "wind clumps". They originate from instabilities in the mechanism that drives the wind as explained in Sect. 1.2.2 (Rauw, 2023). Wind clumping has a significant impact on the determination of mass-loss rates based on thermal radio emission.

As radio emission scales with the square of the plasma density, a clumpy wind will produce more thermal radio emission than a smooth wind with the same mass-loss rate. Neglecting the wind clumping may lead to an overestimation of the determined mass-loss rate by a factor $2-4$ (Crowther, 2007).

Furthermore, the high degree of clumpiness in Wolf-Rayet winds is likely to alter the spectral index of their thermal emission (Nugis et al., 1998), resulting in a deviation from the canonical value of 0.6. The thermal spectral index for such systems with clumps in the stellar wind can be significantly greater than 0.6 (Nugis et al., 1998). This will be taken into account when we consider the thermal contribution of the radio emission from WR 147 in Chapter 4.

2.2.2 Non-thermal radio emission

In addition to the thermal emission, massive stars in a binary system may also present non-thermal (NT) radio emission. Indeed, as it was shown in Sect. 1.3.3, relativistic electrons are accelerated in the WCR and more precisely thanks to the DSA process (implying the presence of a magnetic field), leading to a possible synchrotron emission. If such systems present spectral indices lower than 0.6, or even negative ones, it most likely reveals the presence of synchrotron emission (in the optically thin regime) as seen in Fig. 2.2, and thus the presence of an acceleration process in the WCR region. Negative spectral indices are then a clear indicator of an acceleration process, which allows notably the classification of a CWB as PACWB, as explained in Sect. 1.3.3.

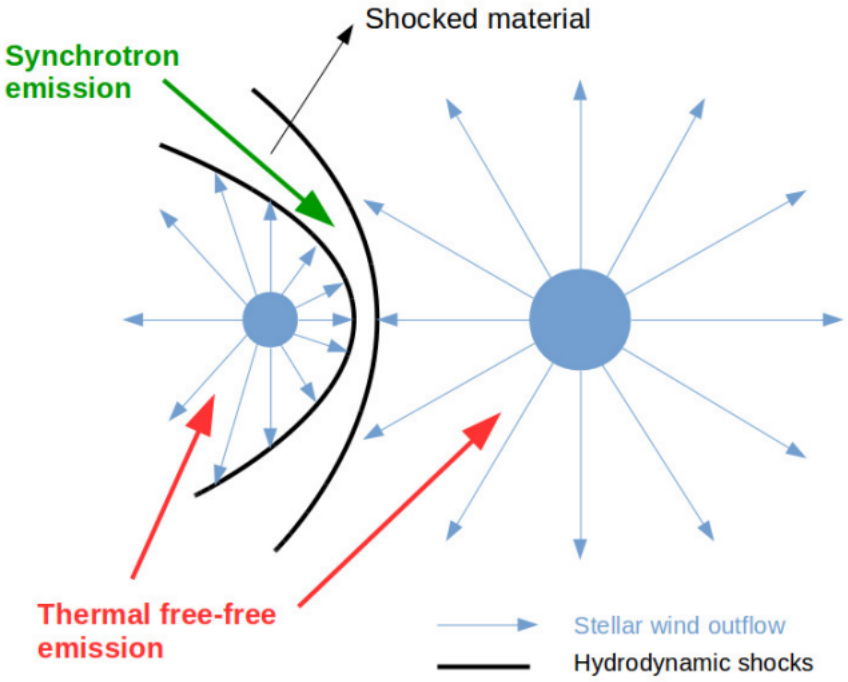

Figure 2.4: Representation of a PACWB with both types of emission (thermal free-free emission from the winds, and synchrotron emission from the shocked material in the WCR). Taken from De Becker (2022)

2.2.3 General radio emission

The global view of these systems can be represented as in Fig. 2.4 with the thermal free-free emission coming from the winds of the star itself and the synchrotron emission arising from the shocks between the two winds and the acceleration of the electrons. The resulting spectrum is likely to adopt a general shape as illustrated in Fig. 2.5. It displays both thermal and non-thermal emissions.

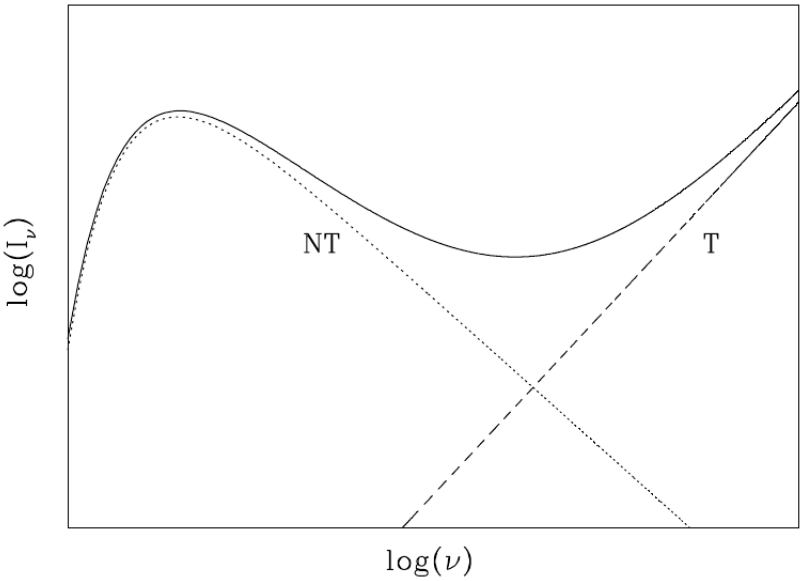

Figure 2.5: General radio spectrum (specific intensity as a function of frequency) of a PACWB taking into account both types of emission; NT = Non-Thermal; T= Thermal. The NT component is affected by a significant turnover process, assumed here to be due to foreground free-free absorption.

Once again it might be interesting to look at the energy budget concerning the radio emission of these systems. Based on Fig. 1.5, only a small part of the wind kinetic power is converted into thermal radio emission coming from the winds themselves. Likewise, synchrotron emission only accounts for a small part of the energy injected in the wind-wind interaction. This could be a possible explanation for the large fraction of WR stars in the catalog. Indeed, the main criterion for identifying a PACWB is synchrotron emission. If the wind kinetic power is higher, as for WR stars, the energy transferred into the electron acceleration process should be higher, also resulting in a brighter synchrotron radio emission and an easier detection.

2.2.4 Clarification of the PACWB identification criteria

In Sect. 1.3.3 it was shown that among the emission processes at work in a PACWB, synchrotron radiation is a very important indicator of particle acceleration. This constitutes a solid basis to establish useful criteria to identify PACWBs (De Becker and Raucq, 2013):

- **Spectral index**: The synchrotron emission is most frequently revealed thanks to the measured spectral index. Indeed, as explained previously, the radio flux density may be described by a power law with a spectral index that is equal to 0.6 (or slightly above) in the case of pure thermal emission coming from the wind (Eq. 2.47). A significant deviation from such values (lower than 0.6 or even negative) most likely indicates a contribution of synchrotron emission. Consequently, such a system is identified as a particle accelerator. Conventionally, one considers that the value of the spectral index must be inferior to 0.3 to be associated with synchrotron emission. A value between 0.3 and 0.6 does not necessarily allow for a definitive detection of synchrotron radiation (De Becker and Raucq, 2013).

- **Excess emission**: As the synchrotron emission is produced on top of the thermal emission from the winds, a particle accelerator may look brighter than expected from a massive star without NT emission. As a result, any excess emission as compared to the expected thermal emission can be seen as a hint for a synchrotron emitter. This criterion can be useful when radio measurements exist at only one specific frequency (thus preventing the determination of a spectral index).

- **Variability**: In a binary system, the stars revolve around each other, potentially leading to some variability in the emission of radiation. This variability may be a hint for the identification of a PACWB, since pure thermal emission from a stellar wind is not expected to be variable[1]. The variability could be either due to an intrinsic variable emission or to a modulation of the free-free absorption of radio photons by the stellar wind material.

  The intrinsic variability is related to the variation of the stellar separation as a function of the orbital phase in an eccentric orbit. In such a system, the stellar separation varies between two extreme orbital phases, apastron and periastron. The wind interaction region in between will thus be characterized by changing properties as a function of the orbital phase. The magnetic field (of stellar origin) in the synchrotron emission region is thus varying, along with the density of the colliding plasmas. The latter is expected to influence the injection rate of electrons into DSA. As both the magnetic field and the number density in relativistic electrons are expected to change, one may expect a variability of the intrinsic synchrotron emission (De Becker et al., 2024).

  The subsequent modulation due to FFA can act from two different points of view. First, in an eccentric orbit, the location of the synchrotron emission region varies, sending it deeper in the winds of the two stars at periastron (leading to a more severe FFA) and unveiling it significantly close to apastron (less severe FFA). Second, even in the absence of a changing orbital separation, the synchrotron emission region may be significantly hidden behind the dense wind of one of the two stars at some orbital

[1] In principle, some variability in the thermal emission may arise in a binary system in the absence of synchrotron emission, provided that the ionization of one wind is significantly influenced by the radiation field from the companion, in an eccentric orbit. This is likely the case in η Car (Kashi and Soker, 2007).

phase from our point of view, leading to enhanced foreground FFA at such orbital phases.

These two effects result in a variability in the flux of the non-thermal emission. Such variations are very useful indicators of the existence of a synchrotron source in the system, allowing us to tag a CWB as a PACWB.

Finally, non-thermal emission from a massive binary in the high-energy domain would also indicate the existence of a population of relativistic particles. This has been confirmed in the case of the systems η Car (Farnier et al., 2011), WR 11 (Martí-Devesa et al., 2020) and Apep (del Palacio et al., 2023). However, to date, radio waves constitute the main spectral domain allowing us to identify particle accelerators among massive binaries.

Chapter 3

Data collection and methods

This chapter will be dedicated to the practical aspect of this Master thesis. The basic concepts of interferometry will be presented in Sect. 3.1 along with the presentation of the telescope that was used to collect the data: the Jansky Very Large Array (JVLA; Sect. 3.2). The third part, in Sect.3.3, concentrates on the data processing that was performed to get the final results.

3.1 Basics of interferometry

3.1.1 General principle and angular resolution

On the contrary of X-rays or infrared (IR) observations, the Earth's atmosphere doesn't absorb too much radio waves. There is an observation window of wavelength between 0.0003 to 30 meters which correspond to a frequency range of 10 MHz to 1 THz. In this range, radio waves can be measured from the surface of the Earth.

Another difference with other parts of the electromagnetic spectrum is the "observation principle". In this domain, the observation is based on the measurement of the electric field of the radio photons, which will create an electric current in the telescope translated into voltage in a resistor. An antenna (or also "sensor") converts the electric field of the incoming photons into a voltage giving information on the amplitude and phase of the electric field.

A radio telescope can be depicted in a simple form as shown in Fig. 3.1 which is another way to explain its principle.

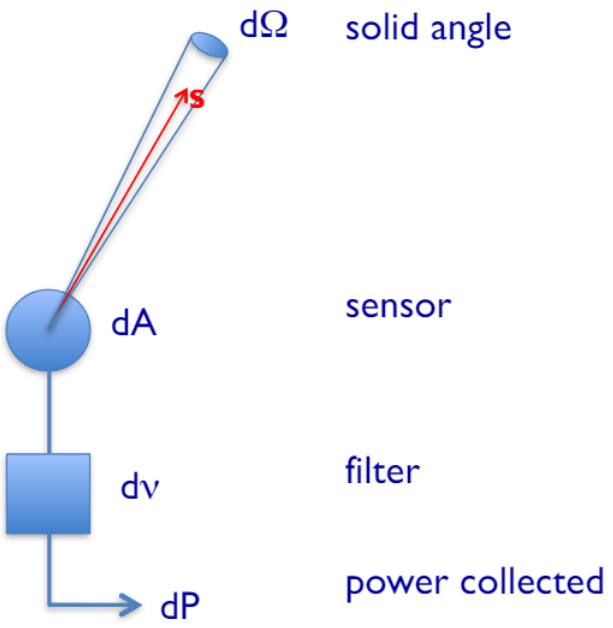

Figure 3.1: A simple representation of a radio telescope. Taken from Perley (16-23 May 2018)

The telescope observes a radio source characterized by a brightness $I(\nu, s)$ with s a unit direction vector. This signal will pass through a collector, or sensor, with an area $A(\nu, s)$ and a frequency filter with a width $d\nu$. The power resulting from this source with a solid angle $d\Omega$ is $dP = I(\nu, s)A(\nu, s)d\nu d\Omega$. Thus, the total power received by this source is the integral of this last quantity over the frequency and solid angle: $P = \int\int I(\nu, s)A(\nu, s)d\nu d\Omega$. (Perley, 16-23 May 2018)

The simplified description presented above concerns one single antenna. Some radio observatories consist of one single-dish telescope, such as the 30 meter IRAM telescope[1], the 100 meter Effelsberg telescope[2] in Germany or the Green Bank Telescope (GBT)[3]. However, an important limitation is met when dealing with one single antenna: the angular resolution. The resolution is defined as:

$$\theta(\text{arcsec}) \approx \lambda(\text{cm})/\text{D(m)} \tag{3.1}$$

with D the diameter of the antenna dish. The human eye can observe waves with a wavelength of 0.5 μm and has a "diameter" of 2.1 mm leading to an angular resolution of 50 arcsec. One of the best-known radio telescopes is the Arecibo Telescope (out of service now) which was designed to observe 6 cm waves with a dish diameter of 300 m, reaching an angular resolution of 60 arcsec. The angular resolution of a single dish is called the primary beam. If a resolution of the order of the arcsec has to be reached, the telescope dish must be larger, with a diameter of the order of a km (Wilner, February 2015), which is not practical. This is the main limitation of a single-dish radio telescope.

[1] https://iram-institute.org/observatories/30-meter-telescope/
[2] https://www.mpifr-bonn.mpg.de/en/effelsberg
[3] https://greenbankobservatory.org/

A solution to this limitation is provided by interferometry, making use of a technique called aperture synthesis. It consists of the combination of a group of antennas or small apertures, responding as a single bigger aperture. The direct advantage of this approach is the increase of the angular resolution, which can now be calculated based on the longest baseline between a pair of antennas of the array, B:

$$\theta(\text{arcsec}) \approx \lambda(\text{cm})/\text{B(km)} \tag{3.2}$$

The radio interferometer ALMA, for instance, can reach an angular resolution of 0.005 arcsec with a 0.3mm λ and a maximum baseline of 15 km (Wilner, February 2015). The resolution of the telescope used in this work, which is also a radio interferometer, will be detailed in Sect. 3.3. This concept can be extended to even longer baselines up to thousands of kilometers (Very Long Baseline Interferometry, VLBI) to reach a much better angular resolution (typically a few milli-arcseconds).

3.1.2 Visibility and Power pattern

A radio telescope works by transforming the electric field or, equivalently, the specific intensity into a measurable voltage. How are the properties of the source transmitted during this conversion? Thanks to Fourier transforms. The radio emission of the source is the specific intensity, also called sky brightness distribution, while the signal received on Earth through the antenna is the complex visibility function. Both are linked by the Fourier transform. More precisely, the van Cittert-Zernike theorem says: "*V(u,v), the complex visibility function, is the 2D Fourier transform of I(l,m), the sky brightness distribution (or specific intensity)*" (Wilson et al., 2013). This results in the following relations with a 2D-Fourier Transform:

$$V(u,v) = \int\int I(l,m)\exp[-i2\pi(ul+vm)]\ dl\ dm \tag{3.3}$$

$$I(l,m) = \int\int V(u,v)\exp[i2\pi(ul+vm)]\ du\ dv \tag{3.4}$$

where u, v, l, m are particular coordinates as shown in Fig. 3.2.

- u, v, w: These are the spatial ground coordinates, with u, v in a tangent plane, and are measured in units of wavelength. The u vector is in the East-West direction and v in the North-South direction, while w is perpendicular to the u, v plane.

- l, m: These are the sky angle coordinates in the tangent plane and are measured in radians. They are the direction cosines on the sky, with l in the East-West direction and m in the North-South direction.

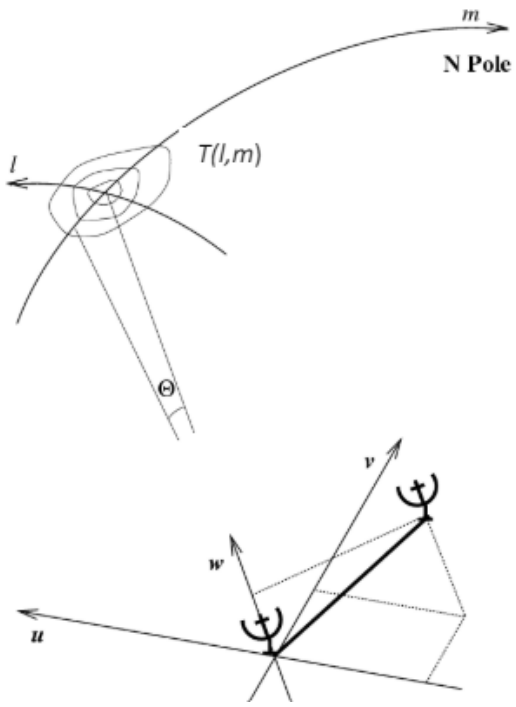

Figure 3.2: Coordinates used in radio interferometry. Taken from Wilner (February 2015)

The Fourier transform allows the decomposing of any kind of signal into a combination of sinusoidal functions keeping all the properties of the original signal. In this case, it preserves the amplitude and the phase of the signal, which are the two ingredients to reconstruct an image. In other words, the brightness distribution from the source can be recovered thanks to the Fourier transform of the visibility function.

3.2 The telescope: Karl G. Jansky Very Large Array (JVLA)

The data used in this work come from the JVLA radio interferometer. This means it is not a single-dish antenna but multiple dishes employing the aperture synthesis technique. This allows the telescope to reach a better angular resolution as explained in Sect. 3.1. The JVLA has 28 antennas but one is decommissioned at each observation. Each dish has a size of 25 m.

The telescope is situated in New Mexico (USA), more precisely in Socorro[4]. This location was selected for several reasons. The main one is its distance from major cities. Indeed, radio interference may arise because of human activity. So it is preferable to construct the telescope far from any human noise source. Moreover, the location is surrounded by mountains which act like a rock barrier against interference. Another reason is the desert nature of this location. Humidity, including water molecules, can be a severe problem in radio astronomy (especially at shorter wavelengths). These molecules may absorb the radio waves, attenuating the signal. The desert allows to avoid this problem.

The antennas are arranged in a Y-shape array, as shown in Fig 3.3. The North arm is 17.7 km long and the two others are 20.9 km. The antennas are spread out along the arms of the Y shape and do not have fixed positions. Indeed, the telescope has different configurations from the most compact to the widest one, as the antennas move along the rails. There are 4 configurations: A, B, C, and D, with A being the widest one, and D the most compact one. The A configuration reaches an extension of 36 km and according to the relation of angular resolution (Eq. 3.2) the higher resolution can be reached with 0.04 arcsec (at 45 GHz). The D configuration is concentrated in 1 km and has a minimum resolution of 850 arcsec (at 74 MHz)[5]. B and C configurations have resolutions between these two values. In this way, the A configuration is used when the aim is to study a region in detail, and on the opposite, the D configuration is dedicated to more extended emission purposes. However, it has to be noted that in the compact configurations, the antennas are close to each other and may create some shadow on the others which may block the light. This effect has to be taken into account especially if the target does not have a high elevation in the sky at the time of the observation. On the other hand, in the widest configuration, more important delays in the received signal may appear between the antennas that are the furthest apart.

Looking at the angular resolution relation, we can see that it depends not only on the baseline distance (changing with the configurations) but also on the wavelength/frequency. JVLA can be operated at different frequency bands, with some impact on the angular resolution. The bands go from 'P-band' (90 cm), which has a frequency range between $0.23 - 0.47$ GHz, to 'Q-band' (0.7 cm), that takes values between $40 - 50$ GHz[6].

[4] https://public.nrao.edu/telescopes/vla/
[5] https://science.nrao.edu/facilities/vla/docs/manuals/oss2017B/performance/resolution
[6] https://science.nrao.edu/facilities/vla/docs/manuals/oss2016A/performance/bands

Figure 3.3: JVLA in D-configuration. Credits: Dave Finley; Courtesy NRAO/AUI.

3.3 Data processing

Data used for this work came from a time request for the JVLA by Dr. Santiago del Palacio. The proposal included the system WR 147 among other PACWBs. The observation covered two nights, 09/08/2016 and 10/08/2016 referred as Epoch 1 and Epoch 2. The software dedicated to calibrating and imaging the radio data is the CASA (https://casa.nrao.edu/) software. The NRAO website proposes several tutorials to learn about data processing with CASA, and in the context of this work, I mainly followed the "VLA Continuum Tutorial"[7][8] The target of interest in this work is WR 147, but during the observing nights several more systems were observed. Thus, the first step was to split the data to recover only the scans related to WR 147. The two nights of observation correspond to two frequency bands in which WR 147 was observed: L-band on the first night, and C-band on the second night. C-band corresponds to frequencies in the range $4.0-8.0$ GHz and L-band in $1.0-2.0$ GHz.

I will explain in more detail what are the different observations linked to WR 147 and how they are organized.
The observations do not only include the target/s but also different calibrators, to be used in a future calibration step. Our observations include the target itself, WR 147, the fluxscale/bandpass calibrator, 3C286, and the Complex Gain Calibrator (CGC) . The bandpass calibrator is the most stable and bright source that will allow us to calibrate the target's flux, while the CGC takes into account the conditions of the observations such as the temperature, the pressure and the delays. This calibrator is chosen to be the closest one to the target on the sky. The specificities associated with the calibrators will be more developed in Sect. 3.3.2.
The data organization for this observation is presented in Table. 3.1. In this case, Field 0 is associated with the Bandpass, Field 1 with the CGC and Field 2 with WR 147. For each night, the bandpass calibrator is first observed at the beginning of the night and then, the

[7] https://casaguides.nrao.edu/index.php?title=VLA_Continuum_Tutorial_3C391-CASA6.4.1
[8] This tutorial includes some parts specifically related to the imaging of a resolved source. This is not the case for WR 147, which is a point source at the angular resolution of our data.

observation of WR 147 is separated into two sets of scans, where the target is bracketed by the CGC observations.

Scan 4	Bandpass	Field 0
Scan 5	CGC	Field 1
Scan 6	WR147	Field 2
Scan 7	WR147	Field 2
Scan 8	CGC	Field 1
Scan 11	CGC	Field 1
Scan 12	WR147	Field 2
Scan 13	WR147	Field 2
Scan 14	CGC	Field 1

Scan 2	Bandpass	Field 0
Scan 3	CGC	Field 1
Scan 4	WR147	Field 2
Scan 5	WR147	Field 2
Scan 6	WR147	Field 2
Scan 7	CGC	Field 1
Scan 11	CGC	Field 1
Scan 12	WR147	Field 2
Scan 13	WR147	Field 2
Scan 14	WR147	Field 2
Scan 15	CGC	Field 1

Table 3.1: Data organization of WR 147 observation for the two nights; Left table : Epoch 2 - C-band ; Right table : Epoch 1 - L-band

Moreover, frequency bands are divided into spectral windows (spw) which are also subdivided into channels (ch). As the C-band and L-band don't have the same width they will not have the same number of spw but all the spw have 64 channels with a width of 2000 KHz. In this observation, the frequency bands are organized as follows:

- C-band has 32 spws going from 8 to 39. Each spw has a frequency width of 125 MHz.
- L-band has 8 spws from 0 to 7. Each spw has a frequency width of 125 MHz.

The last important information is the positions of the antennas during the observations. The JVLA was set in the B-configuration at the time of these observations. Since the targets studied are unresolved with the JVLA, the B-configuration of the telescope was enough. Thanks to the command `plotants` in CASA, one can obtain a plot of the configuration at the time of the observation. As seen in Fig. 3.4, antennas are noted as "ea" followed by their number.
Now that the main aspects of the data are presented, we can proceed with the description of the processing. To get a radio image, several steps have to be executed and most of them are done with CASA. Each step will be related to a specific subsection and, when it will be necessary, a distinction will be made between the C-band and the L-band.

3.3.1 Flagging

The main idea of flagging is to discard bad data which will not be taken into account by the software in the next steps. By flagging the bad data, these are ignored and not suppressed. The command in CASA to flag is `flagdata`. This command may have several modes but the most used one in this work is 'manual'. As its name suggests, the flag is done manually, through a careful inspection of the visibility data, and not by an automatic program. If another mode is used, it will be explained in due course.

Besides target scans, flagging is also applied to calibrator scans. When a flag is applied to one of the calibrators it has to be applied to the related scans of the target (in the same "set" as shown in Table. 3.1). More precisely, if an antenna or baseline is flagged in the bandpass it has to be applied to all the other scans because it is the main calibrator. Besides, if something is flagged in the CGC it has to be applied to the rest of the "set".

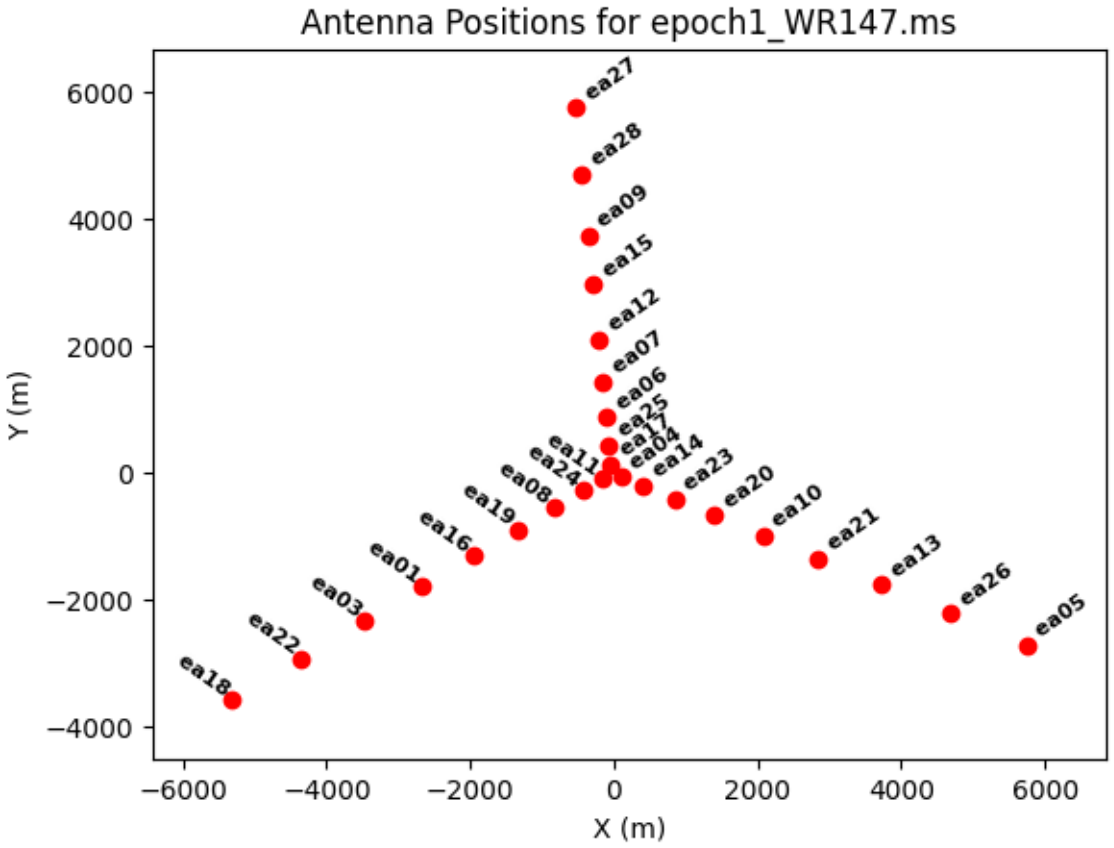

Figure 3.4: Position of the antennas during the observations.

The source of bad data may be a problem with one antenna during the observation, technical issues with the receiver, or Radio Frequency Interference (RFI) that will be more detailed in Sect. 3.3.1.

The first flags to be applied are associated with antenna technical problems during the observation. These are reported in the observing log the JVLA wrote after the observation. None arise on the first night with L-band. Concerning the second night with the C-band, the antenna 'ea20' presented oscillations on the azimuth axis during scans 7 to 10 which could lead to noise in data. The associated data was flagged accordingly. Similar problems arise during this night but they don't involve scans related to WR 147.
Secondly, the first seconds of each scan were flagged. Indeed, it takes some time for the antennas to settle down at the beginning of a scan. This flag is made through the mode 'quack' of the command `flagdata`. Thirdly, all the data equal to 0 value, which are non-physical values, are also flagged. The mode 'clip' allows us to flag these for all the scans.

Then, the concept of shadowing briefly presented in Sect. 3.2 has to be considered. In the most compact configurations of the JVLA, close antennas can put shadows on each other which can affect the data collection. The 'shadow' mode of the `flagdata` task was applied to deal with the associated potential problems, although it is less important in configuration B.

The last but not least step of flagging is the manual flagging. It consists of looking for noise in all the scans, spw by spw (inspecting them in time, frequency, polarization,...)
The order in which the scans are flagged is important because, as explained above, when a flag is applied to a calibrator, it must be applied to the other associated scans, i.e., those that will be calibrated based on that calibrator. For the two bands, the order of flagging was the following:

- C-band: Bandpass (Scan 4) → CGC "set" 1 (Scan 5 and 8) → CGC "set" 2 (Scan 11 and 14) → Target (Scan 6,7,12,13)
- L-band: Bandpass (Scan 2) → CGC "set" 1 (Scan 3 and 7) → CGC "set" 2 (Scan 11 and 15) → Target (Scan 4,5,6,12,13,14)

In the next paragraphs, I will first show the reasoning behind the manual flagging and then how it was applied to the two bands.

The different scans can be analyzed thanks to a tool in CASA called "plotms". Plotms displays the visibility data with many options and parameters as shown in Fig. 3.5. For example, this figure exhibits the amplitude of spws 7 and 2 of scan 15 in the L-band as a function of the frequency. The unit of the amplitude is mJy.
On the bar situated below in the Fig. 3.5, several tools are proposed to analyse the data. The box with a cross allows one to select a part of the data manually and then thanks to the magnifier glass icon we can access the information of the data selected. The details are displayed on another CASA Window which is called "Casa Logger". The Casa Logger informs on all the tasks that are ran in the terminal, problems that may arise, and so on. In Fig. 3.6 details on the data selected in Fig 3.5 are displayed. In this case, the information is organized as follows (taking as an example the upper panel of Fig. 3.6 from left to right) :

- Date and hour of the task executed (2024-02-14 14:14:22)
- Type of given message as informative or warning (INFO)
- Type of asked task (locate+)
- The Scan, as presented in Table. 3.1 (Scan 15)
- The Field and its associated number, as presented also in Table. 3.1 (Field=g1-L-uvminskl and [1])
- The time when these data were taken (Time=2016/08/09 02.36:16.500)
- The baseline with their two possible nominations (BL=ea13&ea26 and [11&24])
- The spectral window (Spw=7)
- The Channel (Chan=39)
- The polarization or correlation (Corr=RL)

The overall reasoning of flagging goes like this: we look at the behavior of the data and look for RFI which corresponds to large amplitude spikes in plotms. These RFI can be associated to a particular antenna, baseline, time or specific channel. Thanks to the Casa

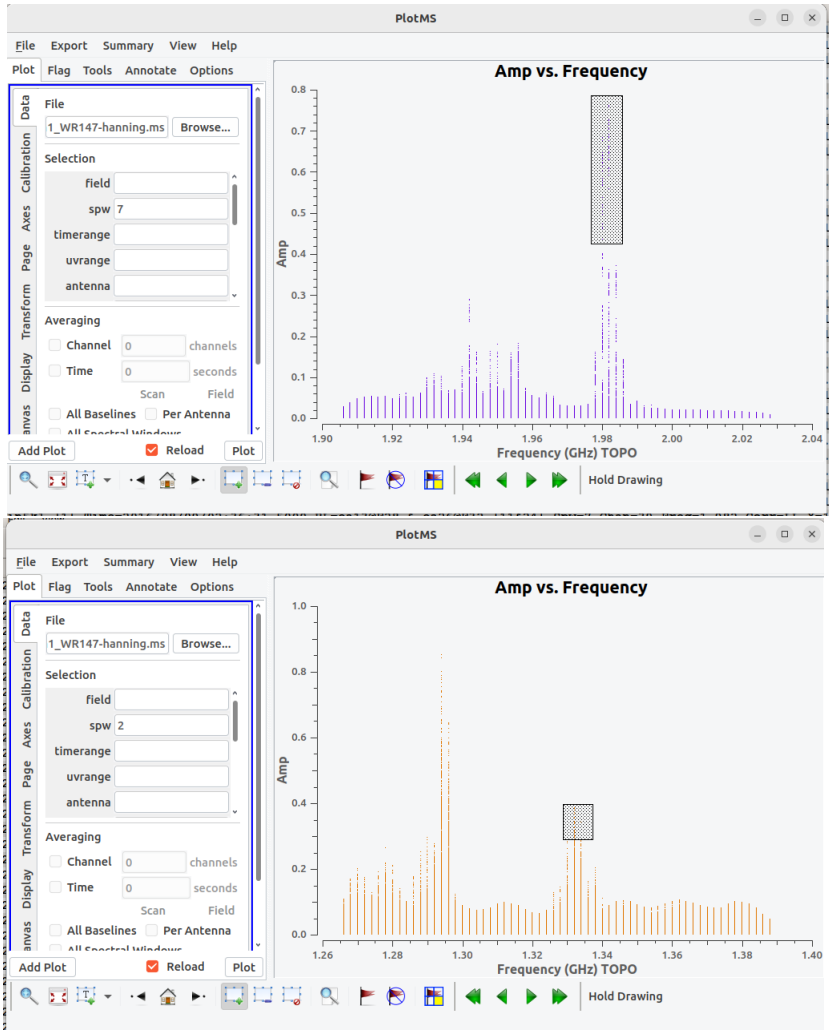

Figure 3.5: Upper image: Plotms display for spw 7 for L-band scan 15. Lower image: Plotms display for spw 2 for L-band scan 15.

Logger it is possible to analyze these spikes and determine what is potentially causing this noise. Then, if the origin of the noise can be identified (antenna, baseline, time,...) it will be flagged.

The principle is quite simple to understand but in practice, it may be hard to apply. Indeed, if we look at the upper panel of Fig. 3.5 and the corresponding detail of the data (in the upper panel of Fig. 3.6) we can see clearly the baseline responsible for this peak, the *ea*13&*ea*26 for channels 38 and 39 (with no specific correlation). However, if we now look at the lower panel of Fig. 3.5 the selected points related to the peak don't match any specific antenna, baseline, or time in the associated Casa Logger (shown in the lower panel of Fig. 3.6). This situation is more frequent than the first simple one. Even if it isn't associated with a particular antenna or baseline it doesn't imply that the peak is not a noise in data. It just shows that the problem involves a lot of different baselines which makes the flagging more complicated.

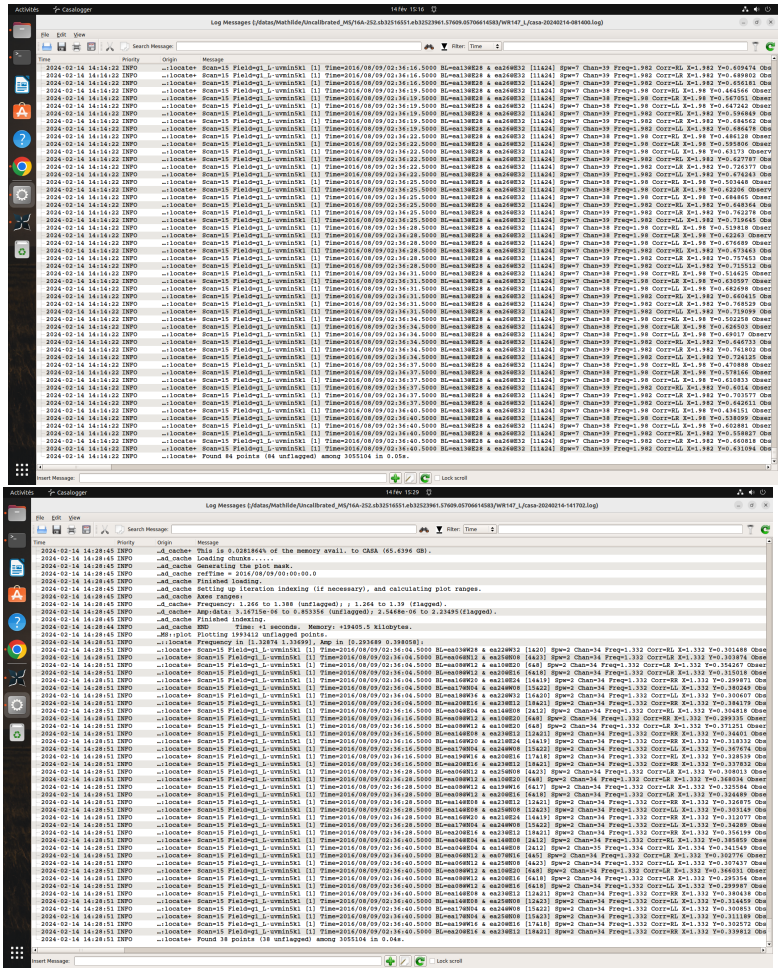

Figure 3.6: Upper image: Casa Logger display for spw 7 for L-band scan 15. Lower image: Casa Logger display for spw 2 for L-band scan 15.

This "procedure" was applied to the two bands in the order presented above, analyzing each spw by spw. I will first present the flagging for the C-band and then for the L-band.

C-band

The C-band is wider than the L-band but was less affected by RFI.

I began with the bandpass calibrator and in some cases, no flagging was needed as in Fig. 3.7 where there is a more or less constant amplitude near 0.20 mJy.

To have an idea of a "clean" example, the bandpass after flagging is displayed in Fig. 3.8.

All the flaggings made on the bandpass calibrator were applied to the other scans. Secondly, I flagged the CGC calibrators (Scan 5 and 8, then Scan 11 and 14 as presented in Table. 3.1). They were noisier than the bandpass but nothing has to be noticed especially. Then these flags were also applied to their related target scans.

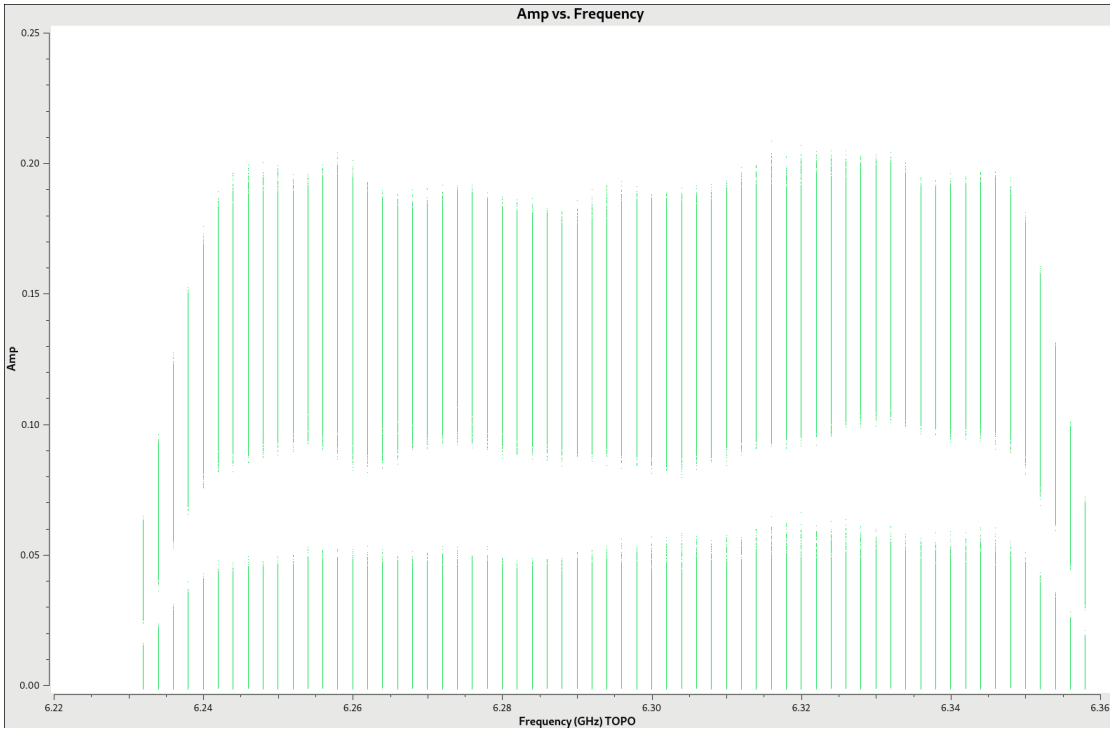

Figure 3.7: Amplitude vs. Frequency for spw 26 in scan 4 (Bandpass calibrator) in C-band

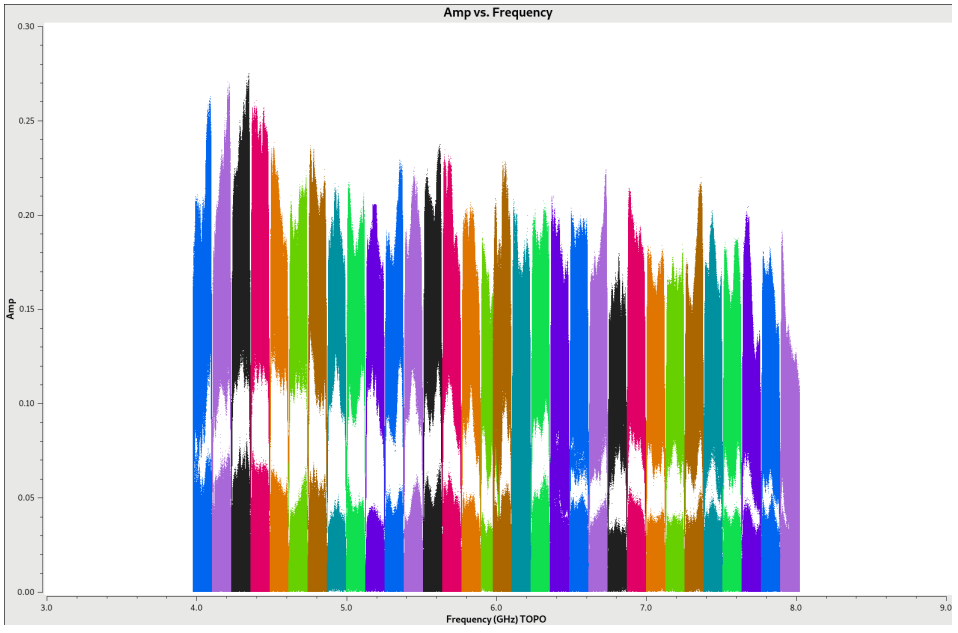

Figure 3.8: Amplitude vs. Frequency for all spw in scan 4 (Bandpass calibrator) in C-band

Then the last step is to flag the target scans, one by one. An example of a comparison between before and after flagging for Scan 12 is displayed in Fig. 3.9. The peaks in the middle of Fig. 3.9a are a good example of noise with an amplitude of 0.3 compared to the average value of the continuum of 0.02.

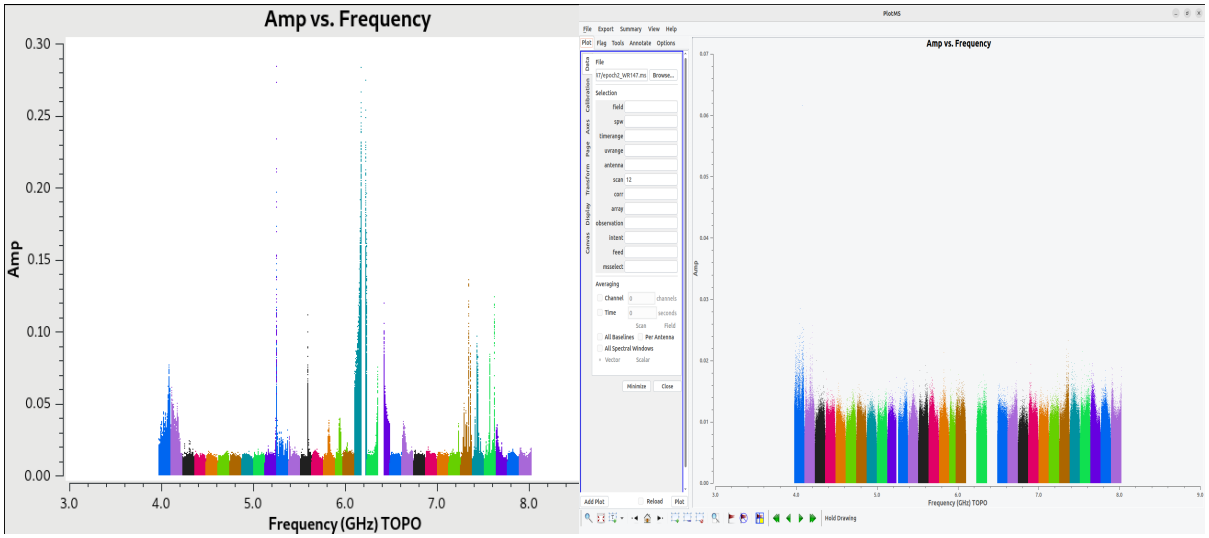

(a) Scan 12 all spw before flagging (b) Scan 12 all spw after flagging

Figure 3.9: Comparison for Scan 12 before and after flagging in C–band

L band

Since the L-band has a smaller frequency bandwidth one could think flagging would take less time than for C-band. Nevertheless, this band was so affected by RFI that the flagging was not straightforward and thus took much more time than expected. In this part dedicated to the L-band, I will present all the steps carried during the L-band flagging with the failures encountered and the possible solutions in chronological order.

Firstly, I began to flag the bandpass calibrator (see Fig. 3.10). At first glance, the spw 4 (brown one) is obviously affected by a high noise level. I started by manually flagging spw by spw. Only two of the eight spw were acceptable (3 and 6). The other ones (for example the spw 2 in Fig. 3.11) showed several noise peaks and a more extended noise pattern. These were not associated with a few clear antennae, baseline, or time, making the flagging long and difficult, especially for spw 4.

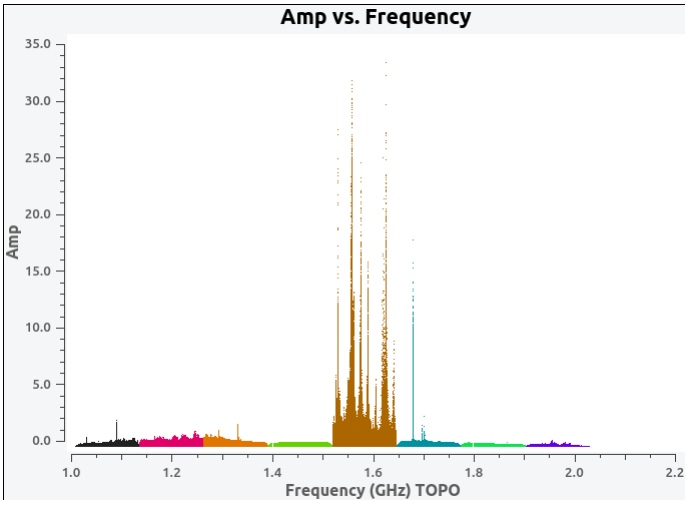

Figure 3.10: Amplitude vs. Frequency for all spw in Scan 2 (Bandpass calibrator)

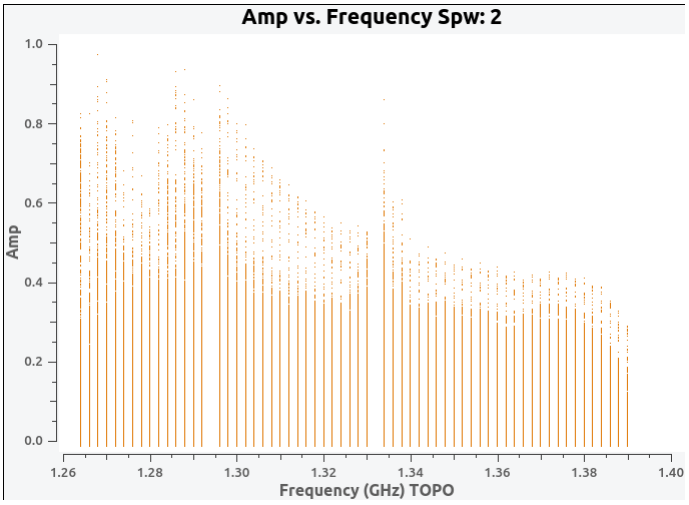

Figure 3.11: Amplitude VS Frequency spw 2 in Scan 2 (Bandpass calibrator)

Flagging of the bandpass is an important step. Indeed, a bandpass calibrator with such variations in the amplitude may raise problems in the calibration step implying incorrect results. However, as pictured in the previous paragraph, it was not manageable to flag manually these spw, in particular for spw 4.

The first possible solution was to apply an automatic function 'tfcrop' which is a special mode of the `flagdata` task. It is an automatic flagging mode using a particular algorithm that identifies in first time outlier points compared to a calculated average and then, flags them a second time. These steps are notably denoted by "calculate" and "apply" options in the parameters of the task. For the bandpass calibrator, it was only applied on the spw 4.

At this point, I decided to move on to the flagging of the CGCs.
The spws of the CGC scans presented more RFI than those of the bandpass scan as shown in Fig. 3.12. So, I used the 'tfcrop' mode on several spws. Then, I tried to manually flag the rest. I followed the same steps for the second slot, CGC2.

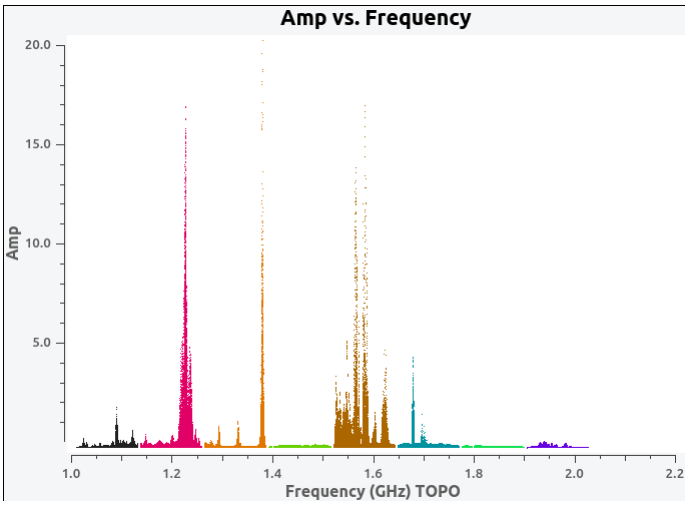

Figure 3.12: Amplitude vs. Frequency for all spws in Scan 3 and 7 (CGC1 calibrator).

I wanted to continue with the target scans, but unfortunately, I realized that some spws were totally flagged in Scan 3 as shown in Fig. 3.13. I supposed the problem came from the 'tfcrop' mode of flagdata because the missing spws correspond to the ones on which the 'tfcrop' was applied. They were in fact full of spikes, but since the frequency width of the L-band is narrower than the C-band, I couldn't afford to lose that much data. Losing too much data may involve not being able to make an image and get some results in this band.

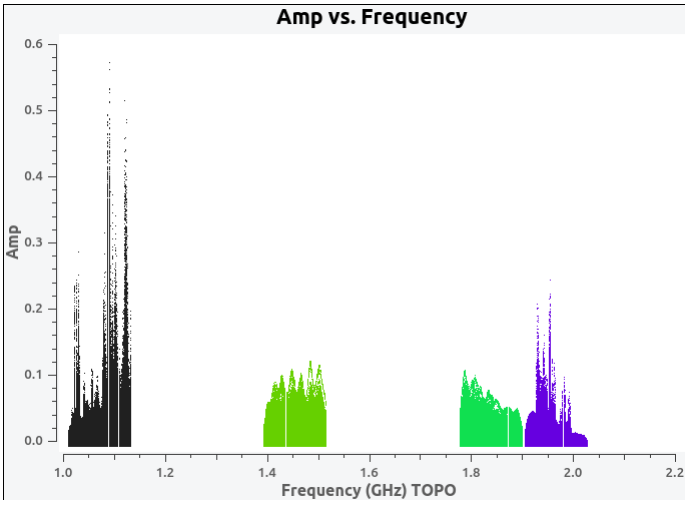

Figure 3.13: Amplitude vs. Frequency for all spws in Scan 3 (part of CGC1 calibrator)

I used 'tfcrop' with the basic arguments but it is an automatic function which has a lot of options related to the implementation of its algorithm. Because I cannot control conscientiously these options to obtain coherent and controlled results, I decided not to use it. I went back to the copy of my data before using this function. The second decision was to flag entirely the spw 4 because even during the trial with the automatic function it didn't help that much. Nevertheless, without this function, it was still hard and time-consuming to flag all these spikes and problem-related features...

At this point I decided to ask for some help from the VLA helpdesk[9]. It is a service proposed by the VLA to help their users if they have any questions (about a proposal, the telescope itself, the CASA interface,...). I explained all the problems encountered with the nearly omnipresent noise and the failure with 'tfcrop' and asked them if there were any solutions to get rid of this noise and at the same time keep enough data. These spikes were RFI, Radio Frequency Interference, and it is known that RFI arise in the L-band frequency range. The Sect. 3.3.1 will be dedicated to these RFI. Sadly, the helpdesk confirmed that there was nothing to deal with the spikes efficiently.

Thus, I decided to manually flag the peaks and noise pattern in a less detailed way than for the C-band because a more careful flagging channel by channel would have taken too much time and would not be manageable. I tried to reach a satisfactory compromise between getting rid of the noise and keeping enough data.

[9] https://help.nrao.edu/

Fig. 3.14 shows the before and after flagging of the bandpass (undertaken with fewer details as explained above).

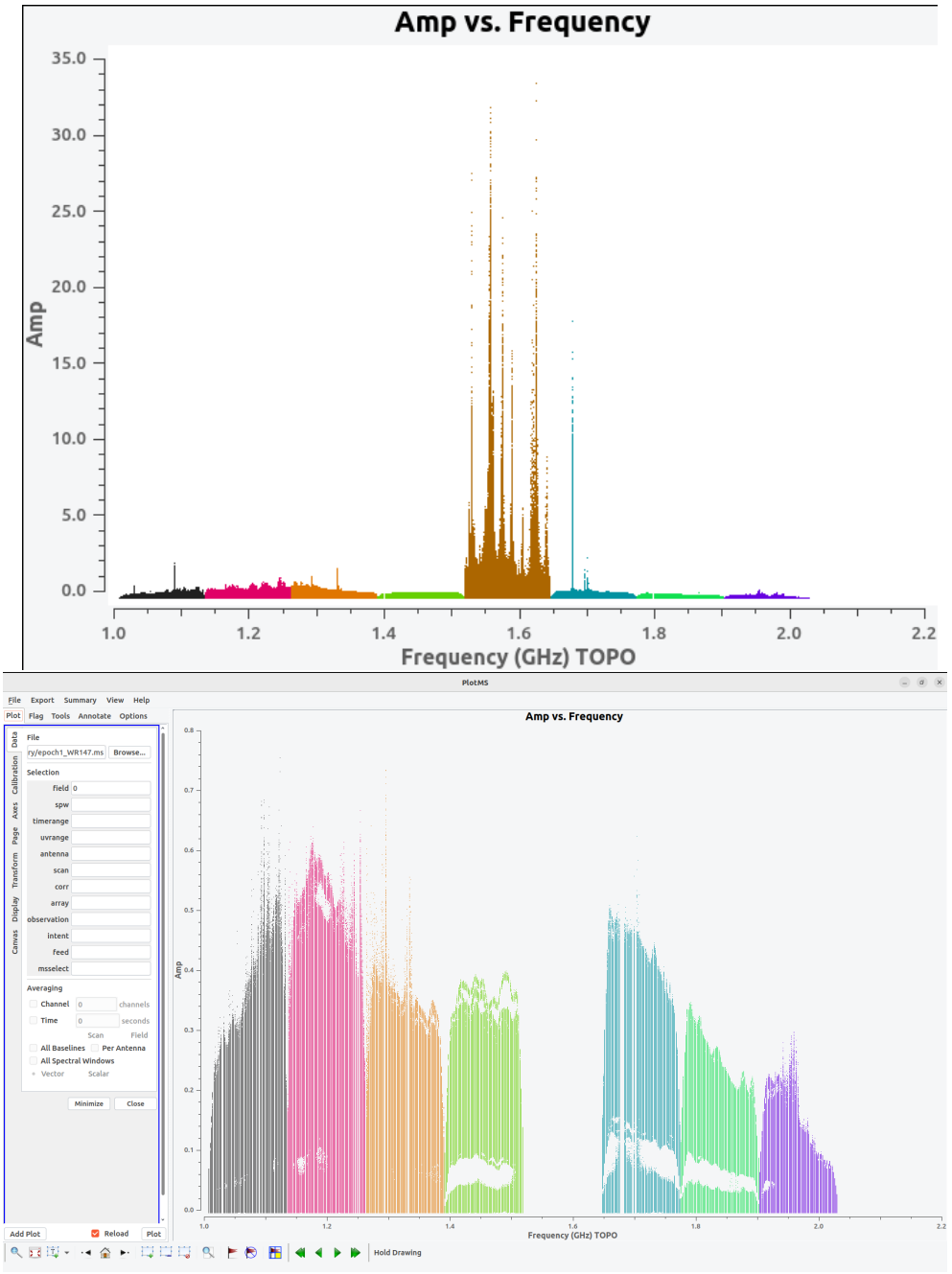

Figure 3.14: Upper image: Plotms display of the bandpass calibrator for L-band before flagging without tfcrop. Lower image: Plotms display of the bandpass calibrator after flagging.

Then, Fig. 3.15 displays the before and after flagging for CGC 1 (Scans 3 and 7 in the right table of Table 3.1).

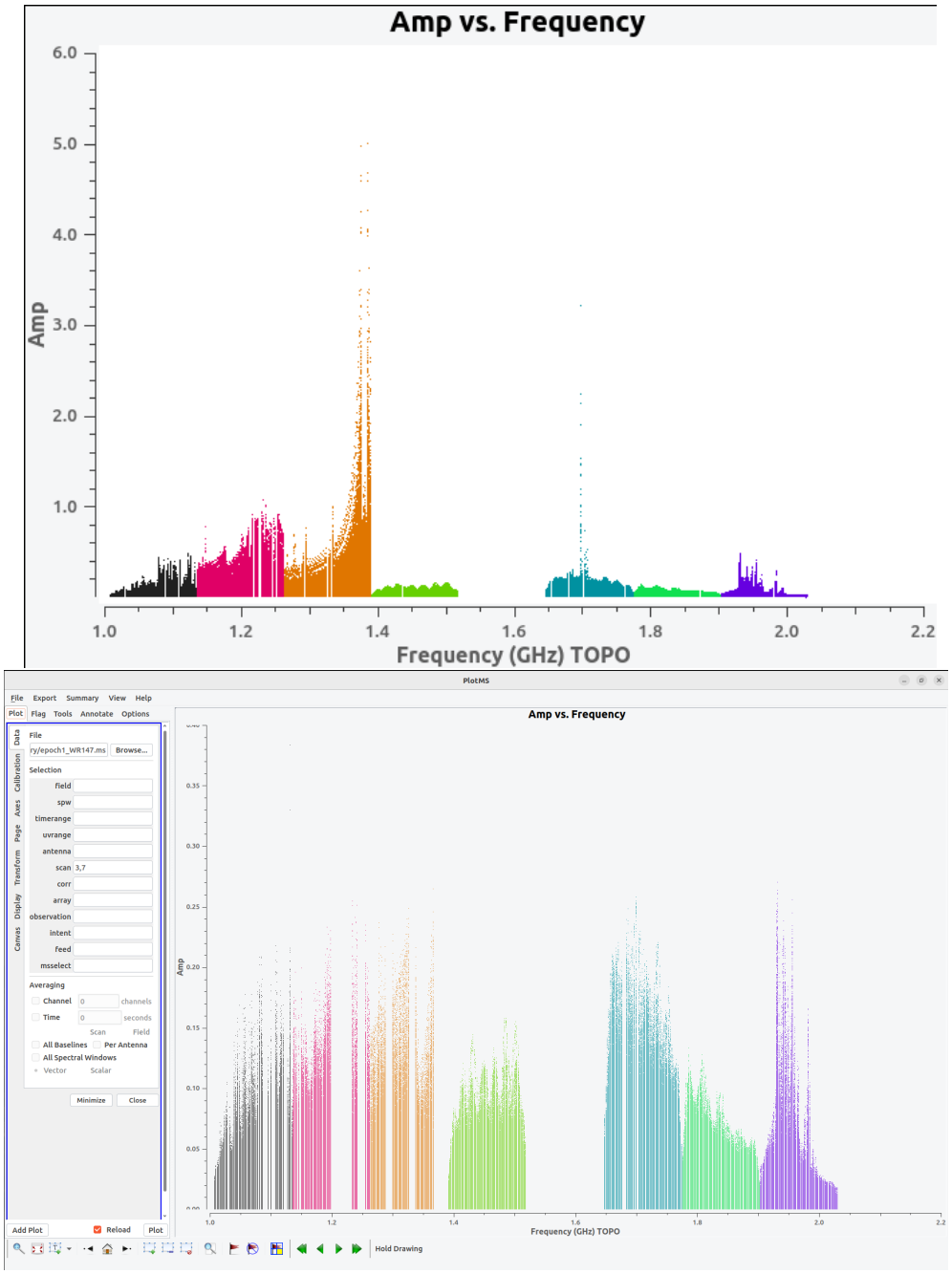

Figure 3.15: Upper image: Plotms display for CGC1 calibrator for L-band before flagging without tfcrop. Lower image: Plotms display for CGC1 calibrator after flagging.

Finally, the target scans were noisier than the bandpass and CGC (even after applying all the flags applied on them). Fig. 3.16 presents only one target scan. The lower part of this figure, Fig. 3.16, depicts the level of details I selected to flag the target scans. For example, the spw 5 (the blue one) still has noise but it was impossible to flag them easily. In this way, I preferred to keep them instead of flagging all the spw.

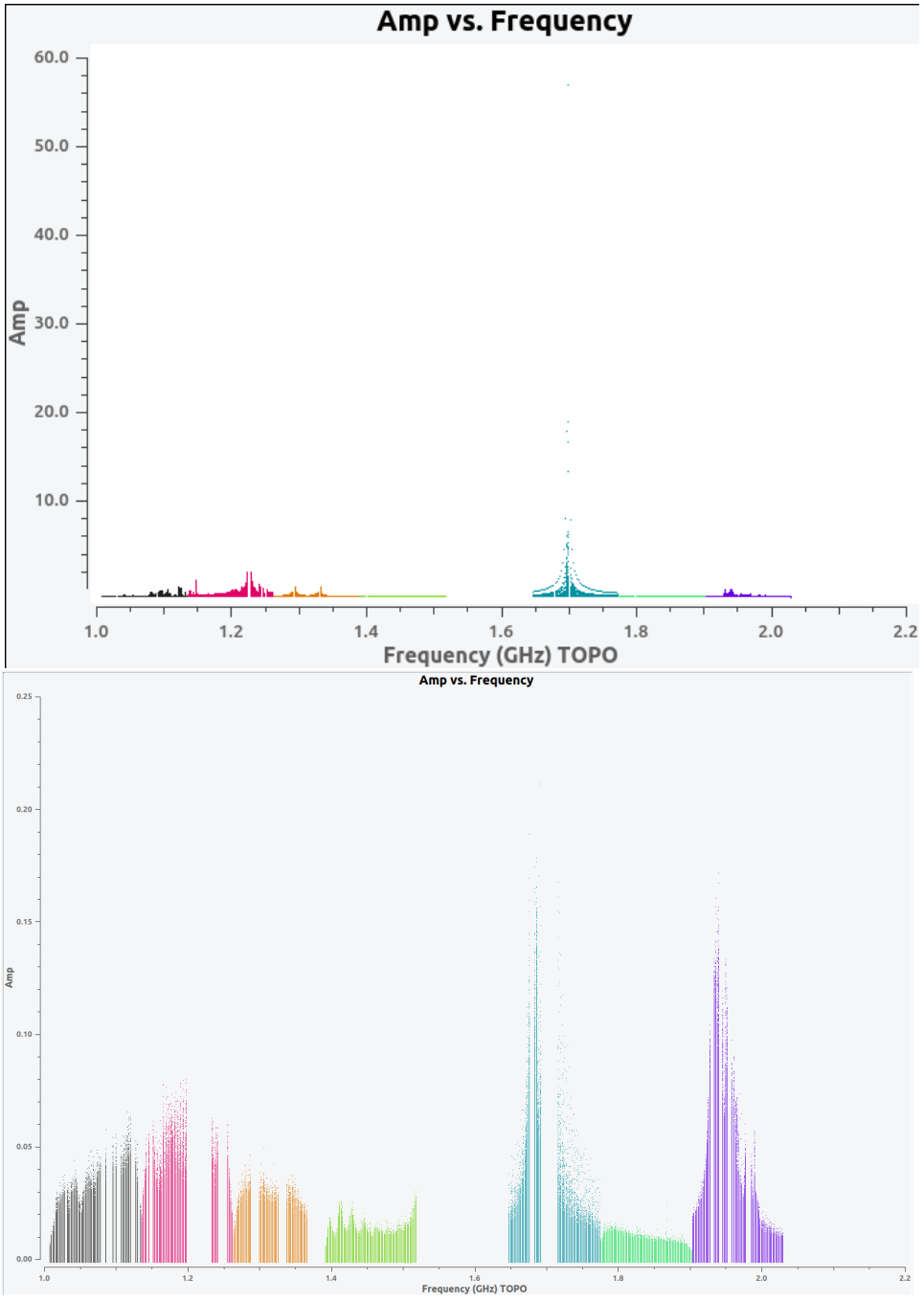

Figure 3.16: Upper image: Plotms display for Scan 4 (Target Scan) for L-band before flagging without tfcrop. Lower image: Plotms display for for Scan 4 (Target Scan) after flagging.

Radio Frequency Interference

As mentioned earlier, the spikes and noise patterns seen in the data were due to RFI. RFI can appear as higher amplitude peaks. This is a signal that does not come from the source itself. This kind of noise affects mainly the lower frequency bands as C, S, or L band[10]. This noise may have an external or internal origin. The internal ones are due to the electronics of the JVLA system. Most of them are eliminated by the JVLA's staff. Nevertheless, some of them remain. The external origin of the RFI is the main problem for radio observations. Indeed, these interferences are notably caused by satellites, aeronautical radar or aircraft navigation. A list of known RFI causes for every band is established by the JVLA allowing the identification of the cause of the peak noise in the data. For example, in Fig. 3.16 the strange pattern in the spw 5 with the peak at 1.7 GHz may be due to the GOES and NOAA weather satellite. The list of the RFI causes of the L-band is much longer than that of the C-band which may explain why the L-band was observed to have more noise than the C-band in this work. These RFIs have different behaviors being continuous, sporadic, pulsed or intermittent with some of them stronger than others.

VLA has a tool, an exposure calculator, which allows you to predict the percentage of data you can expect to lose due to the RFI. In the case of this work, in L-band with a configuration B, 40% are expected to be lost due to RFI, which is in agreement with what we found when inspecting the visibility data.

RFI is a big issue in radio astronomy. The main aspects were notably presented in a conference given by Benjamin Winkel[11]. Some organisms, such as the International Telecommunication Union (ITU-R), are in charge of the radio regulations (RR) which implies setting some principles and rules but also the frequency allocation table. This latter depicts what frequency range is occupied by which service as aeronautical radio navigation, mobile satellite, radio astronomy and so on. The management of all radio sources occupations is a complex task. It was shown that radio astronomy occupies only a few blocks on the global radio spectrum and overlaps with other services. Moreover, the Committee on Radio Astronomy Frequencies (CRAF) performs notably compatibility calculations to determine the impact of cell phones or satellites on radio data to understand the actual data loss. One of the sources of interference mentioned at at the conference was the cell phone networks whose frequency allocations are much more numerous than those dedicated to radio observation and overlap with some of them. If noise associated with cell phones wants to be avoided, antennas must be placed 100 km away from any cell phone base station which is impossible to set up in Europe for example. This is only a glimpse of the complexity of managing the radio spectrum and the actual and future consequences of cell phone networks and satellite constellations on radio observations.

[10] https://science.nrao.edu/facilities/vla/docs/manuals/obsguide/modes/rfi
[11] https://www.evlbi.org/evn-seminars

3.3.2 Calibration

The second important step in data management is the calibration. The main purpose of calibration is to derive scaling factors or corrections from different calibrators whose flux or behavior is known. Then these corrections are applied to the target data.
In the first place, the different calibrators will be described and then, an overview of the calibration process will be presented.

The different calibrators and their use were briefly mentioned at the beginning of the Sect. 3.3 but it might be interesting to specify what they are used for. These calibrators are powerful (quasi) stable sources with accurately known spectra. Most of the time they are quasars. This is the case of the bandpass/flux scale calibrator used in this work, $3C286$. Technically, bandpass calibrator and flux scale calibrator are two different objects but in this case, $3C286$ is both calibrators at the same time.
The bandpass calibrator is used to correct the frequency-dependent response of the interferometer. The flux density scale calibrator gives the reference for the flux density of the signal as a function of the frequency.

As explained in Sect. 3.1, the signal can be represented with a complex number with an amplitude and a phase. Schematically, it can be described by $x + iy = A\exp(i\theta)$ with A the amplitude and θ the phase. The CGC (Complex Gain Calibrator) allows to calibrate both the phase and the amplitude of the signal. It takes into account the variations in time due to changes in the conditions of the instrument or changes in the environment. These changes have multiple sources: variations in the pressure or temperature of the atmosphere, broadcasting satellites or even cell phones[12]. Since the conditions of observations change during the observation time, the CGC is thus observed before and after the target scans. In this way, if time variations in phase and amplitude arise during the observation it will be considered by the CGC and can be applied to the target. Therefore, the CGC must be located close to the target in the sky. Indeed, if it was far from it, then the calibration of the atmosphere conditions would be different.

The calibration process is subdivided into small steps which are executed in a specific order. The overall process is pictured in Fig. 3.17.

[12] https://science.nrao.edu/facilities/vla/docs/manuals/obsguide/calibration

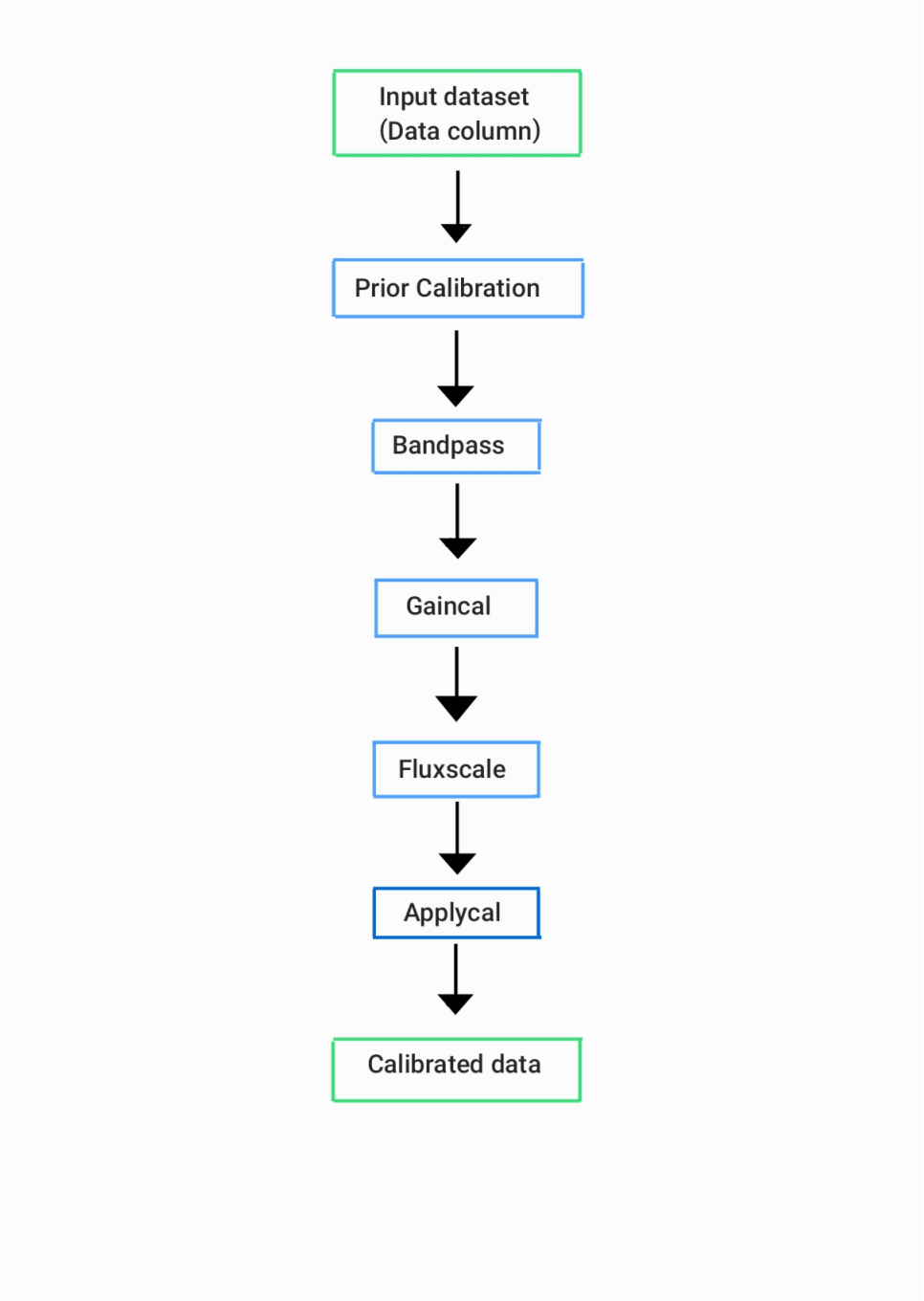

Figure 3.17: Main calibration steps. The green boxes represent the data set including the data column and the corrected data column (see below for an explanation). The blue boxes represent the different calibration steps. These tasks allow the creation of the different calibration solutions stored in the calibration table. The dark blue box is dedicated to the task applycal, which applies the corrections made through the previous calibration tasks.

On top of the Fig. 3.17, there is the input dataset. In CASA, the data are stored in directories called "Measurement Set" (MS). These sets are organised in separate columns. On the one hand, there is the "data" column that encompasses the raw measurements and on the other hand, the "corrected" column which is created after the application of the

calibration [13]. Indeed, the basic idea of the calibration is to derive the different amplitude and phase corrections thanks to specific tasks (bandpass, gaincal,...). These solutions are stored in another directory called "calibration table". Then, this calibration table will be applied to the data creating the corrected data column. It has to be noted that the data marked as flagged during the flagging step are not considered in the calibration.

Let's look at the main calibration steps with Fig. 3.17 as a guide.

- **Prior Calibration**: The first calibration step is the prior calibration which encompasses several subtasks. It includes, for example, the antenna position correction. Indeed, the antenna positions must be accurately known to have a good correlation between the signal that reaches each antenna separately.
  The prior calibration also involves the initial flux density scaling which provides a flux density value for the flux density scale calibrator $3C286$.
  On top of that, the delay calibration is also taken into account by the prior calibration. It permits the derivation of solutions for relative delays that may arise between each antenna and a chosen reference antenna.

- **Bandpass**: The second step is the bandpass calibration. This determines the corrections of amplitude and phase as a function of the frequency for each antenna based on the bandpass calibrator $3C286$. The previously determined corrections calculated in the prior calibration are taken into account.

- **Gaincal**: The third step is to determine the corrections for the complex antenna gain, including both phase and amplitude, as a function of time. It is undertaken thanks to the task `gaincal`. These corrections will be based on the second calibrator (CGC) which is the closest to the target in the sky and mainly consider the variations due to changes in external conditions, as explained previously. Because an absolute phase does not exist, a zero phase is established by choosing the reference antenna for which the gain phase is set to zero.

- **Fluxscale**: In the prior calibration, the absolute flux density of the bandpass/flux density scale calibrator was set ($3C286$). However, this is not yet the case for the secondary calibrator, CGC. The true flux density of CGC can be determined using the `fluxscale` task, based on the flux density scale calibrator.

- **Applycal**: In previous steps, the calibration solutions have only been derived. The final step is then to apply all the calibration solutions to the target data using the dedicated task `applycal`. As previously outlined, the derived solutions stored in the calibration table will be applied to the Data column thereby creating a new column, Corrected Data, containing the calibrated data. Three 'applycal' calls are used. The first two correspond to the calibration of each calibrator. The third concerns the calibration of the target source.

After the calibration, it might be interesting to examine with Plotms the behavior of the corrected calibrators. As expected, for the C-band, nothing suspicious has to be noted. For example, Fig. 3.18 displays the behavior of the amplitude and phase of the CGC after calibration and a quasi-constant/flat trend is observed around a central value.

[13] https://www.aoc.nrao.edu/events/synthesis/2012/Kimball_ALMA_CASA_Calibration.pdf

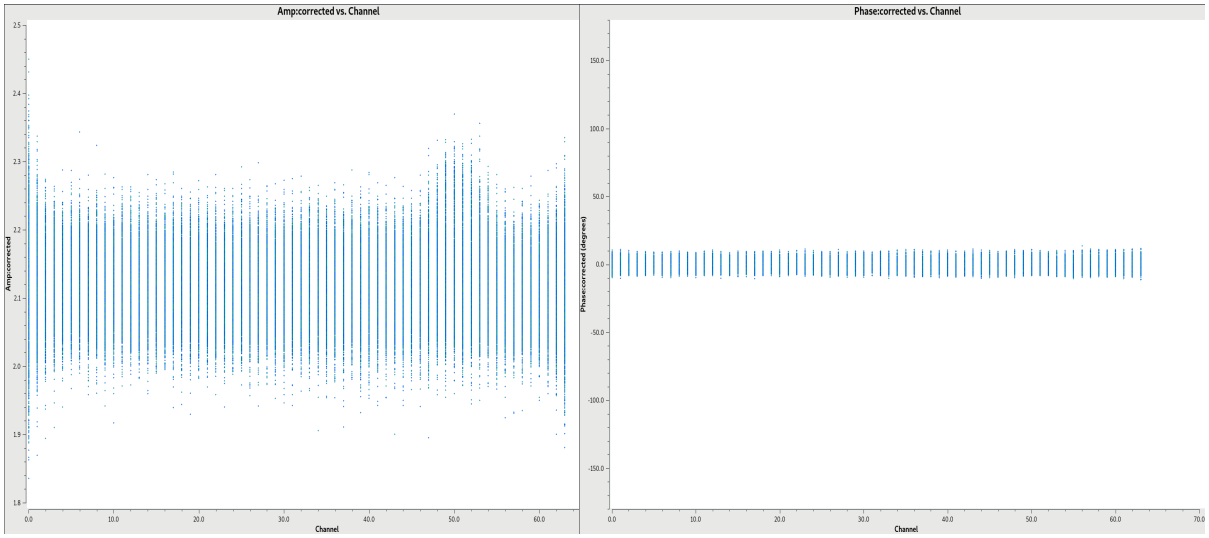

(a) Corrected amplitude as a function of channel for the CGC in C-band

(b) Corrected phase as a function of channel for the CGC in C-band

Figure 3.18: Behaviour of the secondary calibrator (CGC) after calibration of the C-band

However, for the L-band, even after calibration, a less "stable" behavior is seen in Fig. 3.19. The different values are not symmetric around a central one, there is more scattering than in C-band. This is explained by the larger amount of noise present in the L-band data compared to the C-band as explained in Sect. 3.3.1 and more precisely the presence of RFI.

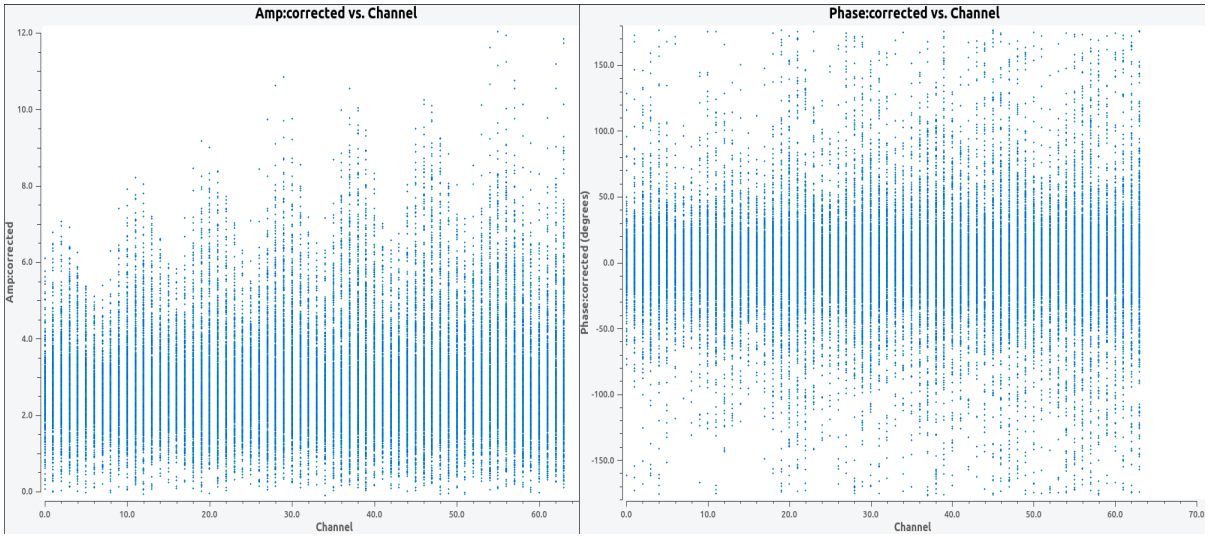

(a) Corrected amplitude vs. channel for the CGC in L-band.

(b) Corrected phase vs. channel for the CGC in L-band.

Figure 3.19: Behaviour of the secondary calibrator (CGC) after calibration for L-band.

As the L-band was still noisy, especially the scans related to the target (as already shown in Fig. 3.16) I employed the semi-automatic flagging option 'rflag' as recommended by the JVLA helpdesk. The 'rflag' option of the `flagdata` task works similarly as the 'tfcrop' previously described, detecting automatically the outliers. However, this option is only applicable to calibrated data. Since it is based on a complex algorithm I decided to work only with the default parameters. It was applied on the corrected target scans (and the

most problematic spw) since these are the only scans that will serve in the next steps. In contrast to 'tfcrop' which flagged too much data, 'rflag' had a minimal impact on the data.

Once the calibration solutions have been applied and the supplementary flagging has been undertaken, the corrected data (corrected target scans) can be separated from the other corrected scans (bandpass and CGC). The task `split` in CASA creates a new 'MS' containing the corrected target data. In the next step of the data processing, only this new 'MS' with the calibrated target data will be used.

3.3.3 Imaging

As explained in Sect. 3.1, the visibility data and the sky brightness distribution (the image) are linked by a Fourier Transform (Eq. 3.3). Thus, we have to apply a Fourier Transform to the corrected target data to have an image of the source. This can be done with the task `tclean` in CASA. Some parameters have to be set to have an optimized image:

- **Pixel size:** The synthesized beam is generally divided into 4 or 5 pixels. Thus, to have the size of one pixel, I divided the beam size, which is given in this VLA site[14], by 4 for each band.

- **Image size:** The size of the primary beam can be calculated. It is given by $\Theta_{PB}(') = 45/\nu(GHz)$. It has to be converted to Arcseconds ("). Then, since the associated size beam for 4 pixels is known, by a rule of three the size of the image (corresponding to the primary beam) in pixels can be deduced.

- **Number of iterations:** The task `tclean` does not proceed with only a single Fourier transform but also encompasses a whole image cleaning process with different cycles helping to reduce the residuals between the data and a model of the source. The number of iterations corresponds to the number of cycles the image will go through during the cleaning process.

- **Weighting:** Several weighting functions are proposed as parameters for the task `tclean` . The one selected in this work is the Briggs function coming with another parameter 'robust'. If the 'robust' parameter takes a value near -2 it corresponds more to a uniform weighting which privileges the resolution. On the opposite, if the 'robust' parameter takes a value near 2 it corresponds more to a natural weighting which privileges the sensitivity. In this way, thanks to 'robust' value one can choose between having a better sensitivity or resolution. In this work, a value of 0 was chosen for L and C-bands to achieve a good compromise between both.

Different values for these parameters were tested. They were quickly analysed by eye thanks to the CARTA program. CARTA is a tool dedicated to the image visualization and analysis of images. The best images were achieved with the following set of values summarized in Table. 3.2. These images, one per band (L and C), are presented in Fig. 3.20. The target source is near the center of the images.

[14] https://science.nrao.edu/facilities/vla/docs/manuals/oss/performance/resolution

Parameters	L	C
Pixel size	1.075 arcsec	0.25 arcsec
Size of the image	2048	2400
Nbr of iterations	2000	2000
Briggs robust	0.0	0.0

Table 3.2: Main best parameters of `tclean` for L-band and C-band images.

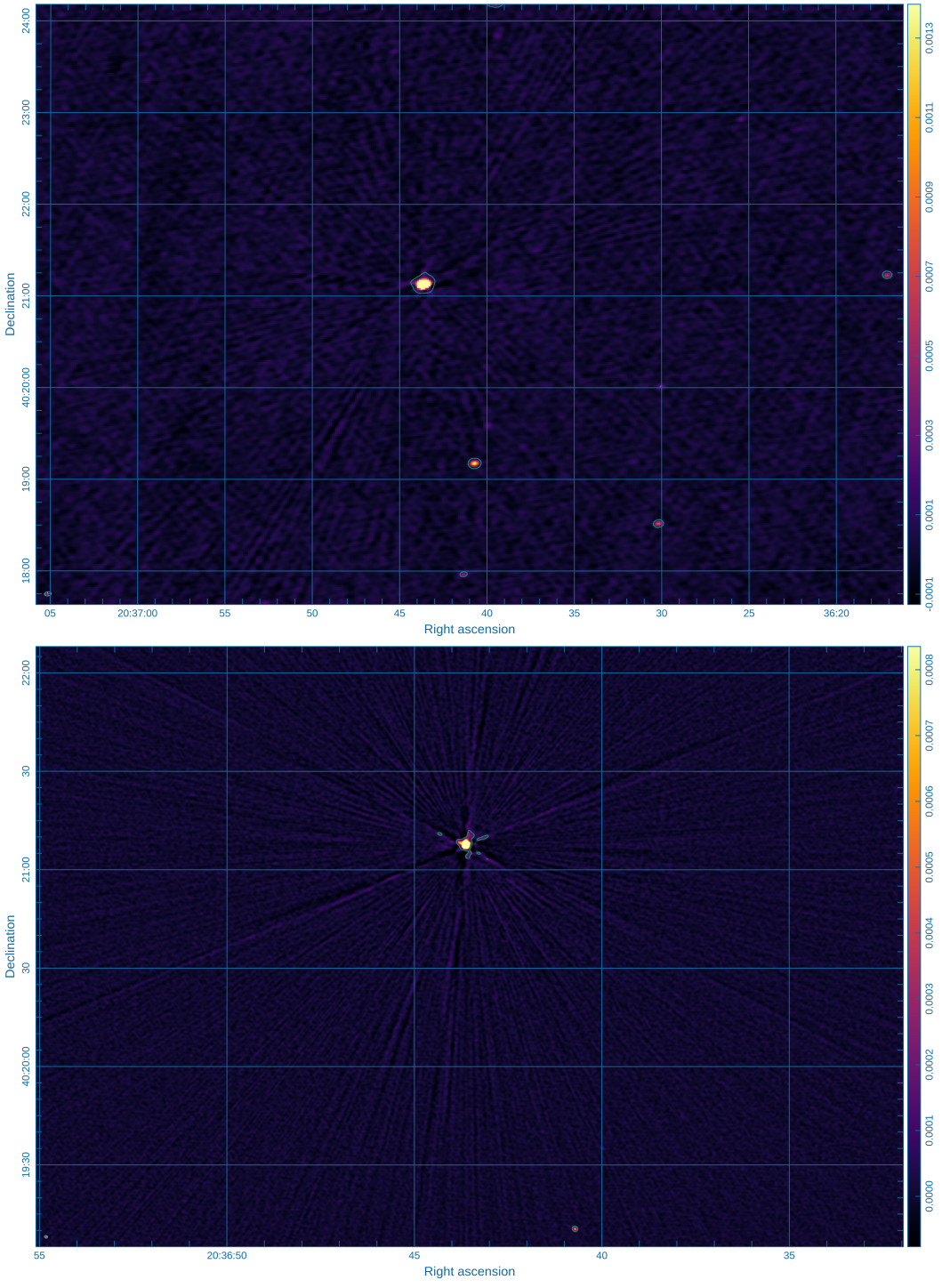

Figure 3.20: Images of WR 147 in the two bands before the Self-Calibration; upper panel shows the L-band ; lower panel shows the C-band.

One can observe in Fig. 3.20, some radiation patterns, especially in the C-band, emerging from the source. It is not a real physical signal but an artifact due to the interferometry process and Fourier Transform. Moreover, in the L-band some other sources can be observed that are not visible in the C-band. This is explained by the frequency range of the two bands. The L-band includes the frequency of an atomic hydrogen transition, more precisely the neutral hydrogen line at 1.4 GHz, which is omnipresent in the universe so it is more likely to detect more sources in the L-band.

Once again I asked for the opinion and advice of the JVLA helpdesk based on Fig. 3.20. They answered that my data could benefit from phase Self-Calibration. Self-calibration is a complex process that takes time to understand and is difficult to handle. Because of this and the fact that I deal with an unresolved source, I only used the default parameters and I will only present the basic principle.
Self-calibration is a process used after the initial calibration if there are remaining errors in the data. It is only useful in particular situations that include possible effects of RFI in the image. The principle is the same as the calibration i.e. derive the corrections with respect to a model and apply them to the target source. The specificity of Self-Calibration resides in the choice of the model which is the image of the source itself made with `tclean`, instead of the calibrators. The procedure can be described in three main steps :

1. Create an image of the source with `tclean` using the Corrected data column coming from the initial, standard calibration. These data are stored in the Model column.

2. Thanks to the task `gaincal` the corrections are derived by comparing the Data column and the Model column (containing the Corrected data) and are stored in an external table.

3. Then, with the task `applycal` these corrections are applied to the Data column. It will create new Corrected data which will overwrite the previous one made by the initial calibration.

What is more difficult in Self-Calibration is setting the calibration parameters between steps 2 and 3. Indeed, thanks to 'Plotms', the calibration solutions can be inspected, and based on them the parameters can be optimized. Another tricky aspect of the Self-Calibration is the undetermined end of the process. The Self-Calibration can be made several times and is not limited to only one round. The number of iterations depends on many aspects but mainly on the data quality, the structure of the source, and the user's patience.

After one round of Self-Calibration with the parameters suggested by the tutorial, the imaging results are shown in Fig. 3.21. We can see that the different noise patterns have disappeared and the source is more distinguishable.

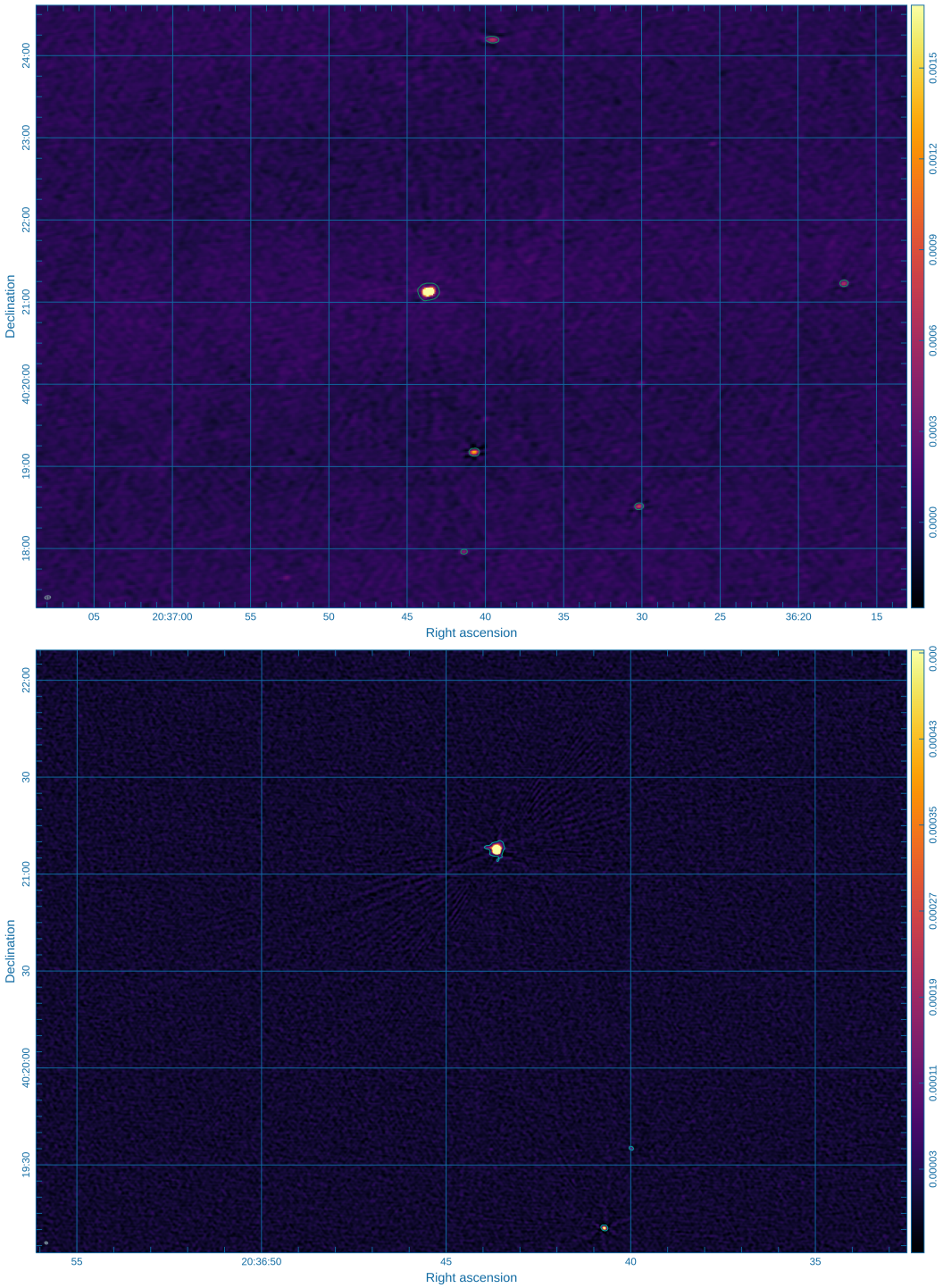

Figure 3.21: Images of WR 147 in the two bands after the Self-Calibration; upper panel shows the L-band ; lower panel shows the C-band.

After all the data processing including flagging, calibrating, and imaging, it was possible to recover the emission from WR 147 in both L-band and C-band, despite the important effect of RFI.

Chapter 4

Multi-bands spectral analysis

In this Chapter, I will first present the imaging of the source made spw by spw. Secondly, I will show how the different measurements of interest can be obtained based on these images. Thirdly, the general radio spectrum based on these values will be displayed along with a fitting based on the *foreground absorption model* presented in Chap. 2. Finally, we will present the results obtained using an alternative model that will be called the *internal absorption model*.

4.1 Multi-frequency images and data acquisition

4.1.1 Multi-frequency images

The general method to obtain an image in a complete spw was described in Sect. 3.3.3. Two images of the source were obtained, one for each frequency band displayed in Fig. 3.21. One possibility offered by CASA is to make images within a particular frequency range by only specifying it in the `tclean` task. I decided for this work to make images of the source for each spw in both bands. This results in 32 images for the C-band and 8 images for the L-band. It has to be noted that the Self-Calibration was only performed for the entire band. Its application to every specific spw would have been too time-consuming in the framework of this master thesis.

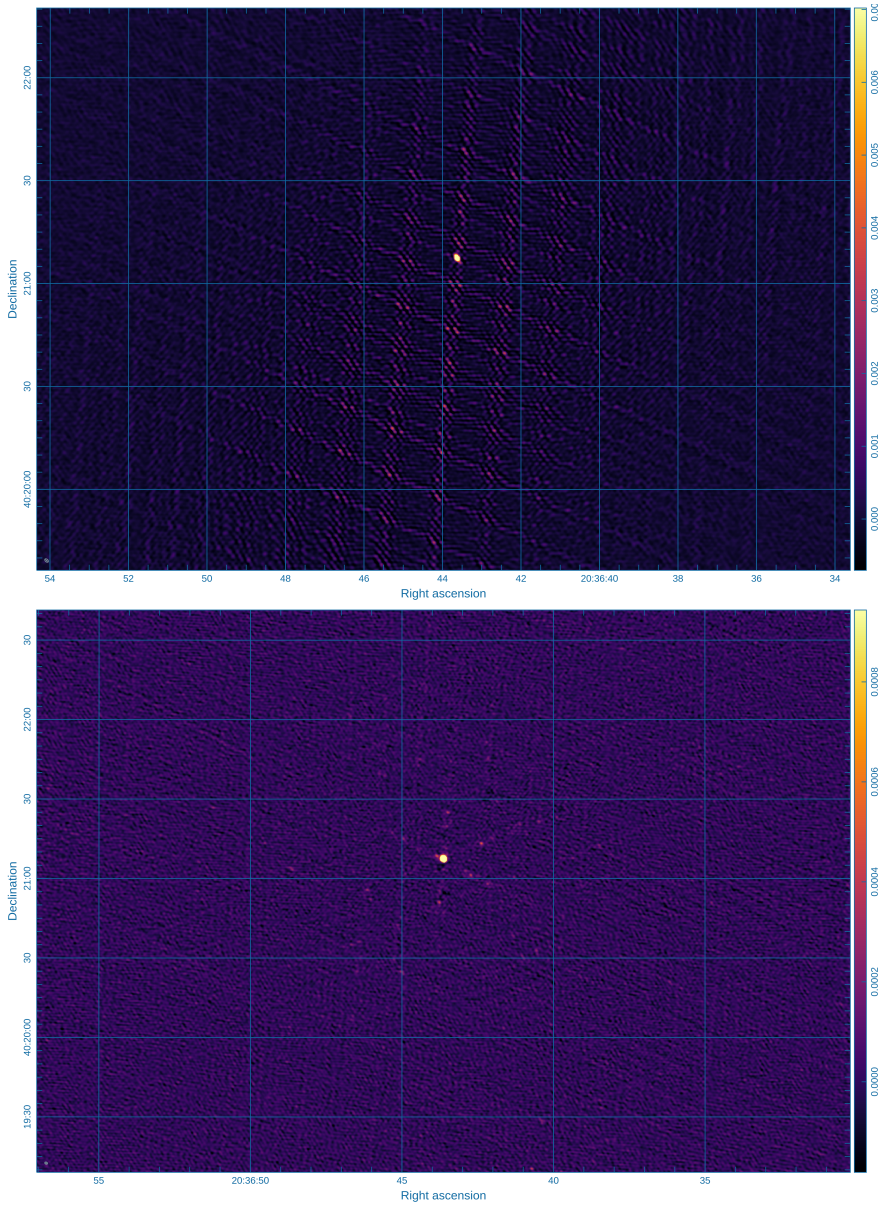

Figure 4.1: Images of WR147 in C-band in two different spws (17 and 19) without Self-Calibration.

It can be seen from Fig. 4.1 that the quality of the image is somewhat lower than that of the full band image (Fig. 3.20). Indeed, with an entire band, we have a lower spectral resolution but a higher Signal-to-noise ratio (SNR). Conversely, an image based on only one spw offers a more accurate spectral resolution with a lower SNR. It can be intuitively understood as 'if we have more data due to a larger frequency range, the accuracy of the flux values will be better but it is less precise in terms of frequency". It can be noticed in Fig. 4.1 that the quality of the image varies with the selected spw (these spws have been selected for comparison purposes only). As seen in the flagging step, not all the spws of the target scans have the same behavior or the same level of noise, which then impacts the quality of the image.

4.1.2 Data acquisition

The CARTA tool allows us to get information about the source. The ones that are useful in this work are the flux density of the source and the RMS (Root Mean Square) of the image.

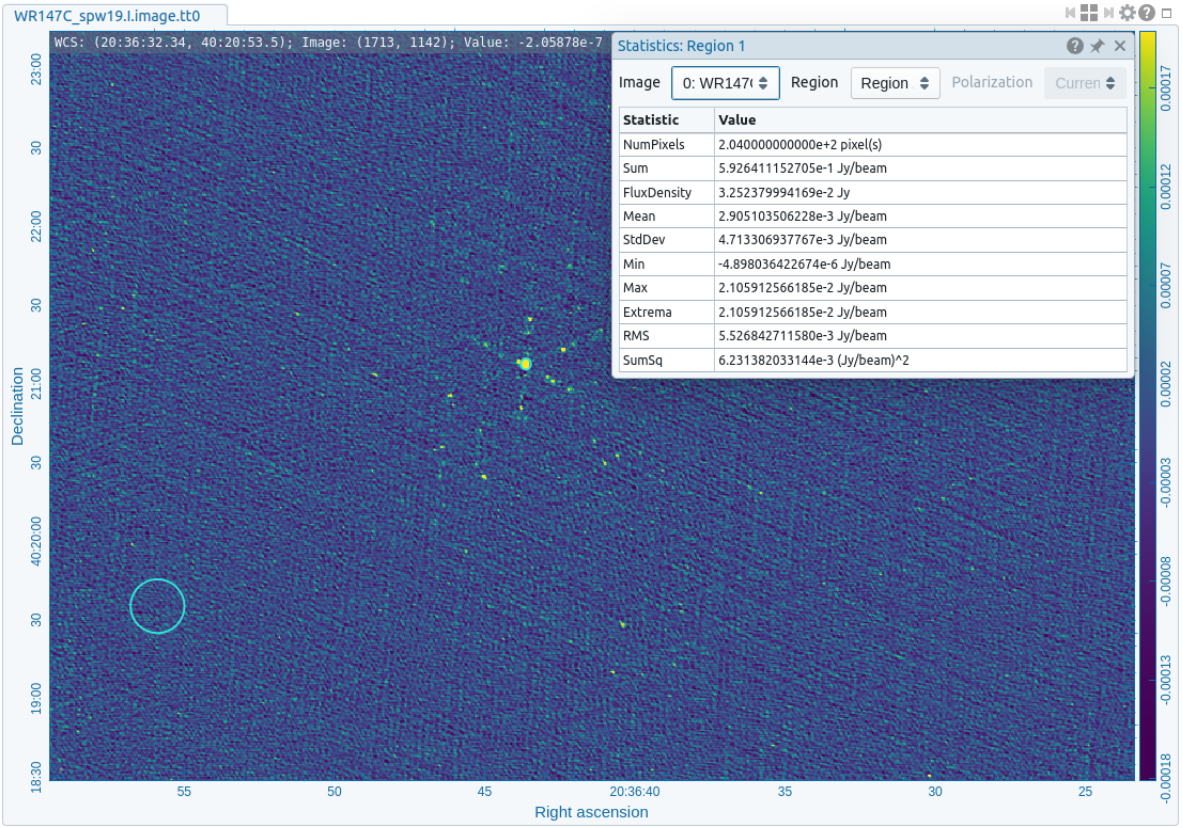

Figure 4.2: CARTA example of how to get useful information about any specific location on the radio map (here, image of WR 147 in L-band, spw 19). In the upper right corner, the widget displays the information about a specific part of the image (for instance, here, the small circular region enclosing the target).

As observed in Fig. 4.2, in the upper right corner of the image, a widget in CARTA summarising all the statistical information about the source is shown. The rows of the column "Statistic" used in this work are "FluxDensity" and "RMS". In addition to that, two blue circles are marked in the image. The center circle is the region enclosing the source and the circle in the lower left corner represents the background region chosen. This latter is selected to be not too close to the source and not too close to the edges of the image. The wanted region can be selected in the widget thanks to the "Region" tool. The flux density, given in Jy, is measured in the region enclosing the source and the RMS, in Jy/beam, is measured in the background region.

The error in the flux density measurements is not only given by the RMS noise which is generally defined as the average of electronics-originated noise. Since the flux density was calibrated against the flux scale calibrator ($3C286$), the error on this latter has to be considered as well. The absolute accuracy of the flux density scale is said to be of the

order of 2%[1]. The RMS noise and the error of the flux calibrator are added in quadrature leading to the final error on the flux density measurements σ_f :

$$\begin{aligned}\sigma_f &= \sqrt{\sigma_{RMS}^2 + \sigma_{cal}^2} \\ &= \sqrt{\sigma_{RMS}^2 + (0.02 * S_\nu)^2}\end{aligned}$$

Some of the spws were discarded due to their high RMS. The parameters of the source in the remaining spws for each band are summarized in Table. 4.1.

[1] https://science.nrao.edu/facilities/vla/docs/manuals/oss2016A/performance/fdscale

Spw	Central Frequency (MHz)	Flux Density (mJy)	RMS (mJy/beam)	σ_f (mJy)
1	1199	23.4	1.31×10^{-1}	0.485
2	1327	24.2	6.66×10^{-2}	0.488
3	1455	25.0	4.60×10^{-2}	0.502
5	1711	26.1	5.25×10^{-2}	0.524
6	1839	26.8	4.26×10^{-2}	0.537
7	1967	27.4	6.80×10^{-2}	0.552
8	4039	31.6	4.18×10^{-2}	0.633
9	4167	31.4	4.53×10^{-2}	0.629
10	4295	32.6	4.70×10^{-2}	0.653
11	4423	32.6	3.86×10^{-2}	0.653
13	4679	31.4	3.55×10^{-2}	0.629
14	4807	32.2	3.99×10^{-2}	0.645
16	5063	31.6	4.23×10^{-2}	0.633
18	5319	32.9	3.15×10^{-2}	0.658
19	5447	32.5	4.55×10^{-2}	0.651
20	5575	34.0	4.46×10^{-2}	0.681
21	5703	34.3	4.43×10^{-2}	0.687
22	5831	33.2	4.77×10^{-2}	0.665
24	6039	33.6	4.50×10^{-2}	0.673
26	6295	33.9	4.18×10^{-2}	0.679
28	6551	32.7	4.16×10^{-2}	0.655
29	6679	34.1	4.78×10^{-2}	0.683
31	6935	35.3	4.33×10^{-2}	0.707
32	7063	33.0	5.42×10^{-2}	0.662
34	7319	34.7	4.83×10^{-2}	0.695
35	7447	35.0	4.88×10^{-2}	0.701
36	7575	34.9	4.23×10^{-2}	0.699
37	7703	33.5	5.01×10^{-2}	0.671
38	7831	34.5	5.35×10^{-2}	0.692
39	7959	34.0	6.11×10^{-2}	0.682

Table 4.1: Values of the frequency, flux density, RMS, and the final error on the flux density σ_f. The first upper section (up to spw 7) is related to the L-band, and the second one, to the C-band.

4.2 Radio emission spectrum and foreground absorption model

4.2.1 Overview of the radio spectrum

The spectrum of both L-band and C-band can be obtained with the values given in Table 4.1. It is displayed in Fig. 4.3. The first trends that emerges from this figure are a quasi-linear increase for the L-band (red) and a more or less constant behavior for the C-band (blue). For the latter, a slightly increasing trend is suggested by the plot, but is has to be considered with caution regarding the scatter of the measurements and their error bars.

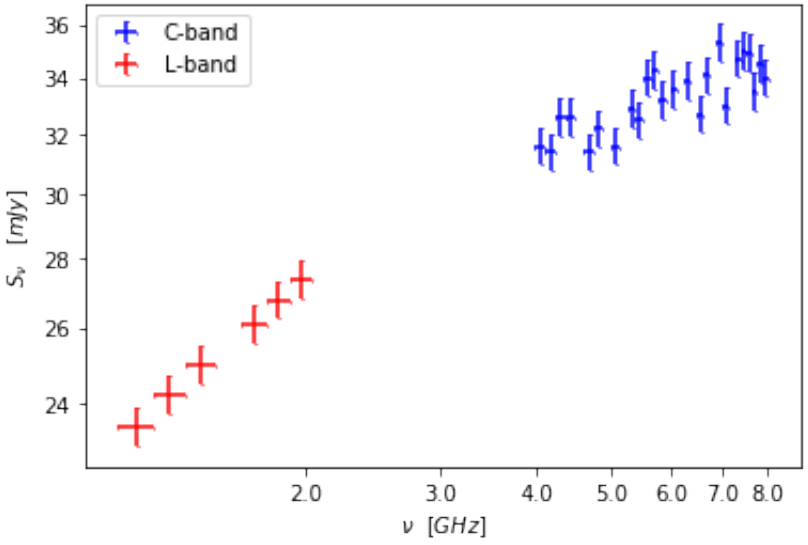

Figure 4.3: Spectrum for WR 147 including the L-band (red) and C-band (blue).

The spectrum fitting to the foreground absorption model will be conducted step by step, with each step described in the next subsections. The foreground absorption model on which the fitting will be based is given by the sum of the thermal and non-thermal contribution as presented in Chap. 2. More precisely, it is given by the following expression:

$$S_\nu = A\nu^{\alpha_{TH}} + B\nu^{-\alpha_{NT}} e^{-\tau_\nu} \tag{4.1}$$

$$= A\nu^{\alpha_{TH}} + B\nu^{-\alpha_{NT}} e^{-C\nu^{-2.1}}. \tag{4.2}$$

It has to be noted that, for the non-thermal component, the convention for the spectral index (α) sign adopted is the theoretical one as presented in Chap. 2 i.e. $S_\nu \propto \nu^{-\alpha}$. According to this convention, the α_{NT} will exhibit a positive value with the negative sign preceding it which is compliant with the behavior of the synchrotron flux meaning a decrease of the flux with increasing frequency. Eq. 4.1 expresses the flux density (S_ν) as the sum of the thermal component of the emission (the first term) and the non-thermal component (the second term).
On the one hand, the thermal term is based on Eq. 2.47 but in a more general form with α_{TH} and a normalization coefficient (A). On the other hand, the non-thermal component relates to Eq. 2.40. This expression takes into account the optically thin part of the synchrotron emission with a spectral index α_{NT} and a normalization coefficient (B), along with the turnover modifying the spectrum at lower frequencies through the factor $e^{-C\nu^{-2.1}}$. This factor explicitly assumes that the turnover is due to free-free absorption (FFA) of the

ν (GHz)	$\Delta\nu$ (GHz)	S_ν (mJy)	ΔS_ν(mJy)	Reference
42.8	0.05	83	2	Contreras et al. (1996)
231	0.064	280	30	Williams et al. (1997)
273	0.034	292	15	Williams et al. (1997)
375	0.064	357	70	Williams et al. (1997)

Table 4.2: Radio measurements of WR 147 at high radio frequencies found in the literature.

synchrotron emission with τ_ν being the optical depth defined in Eq. 2.14, and C, another normalization coefficient quantifying the amplitude of free-free absorption. The frequency dependence in the exponential factor results from the dependence of the optical depth on the frequency through two factors: ν^{-2} and $\ln\Lambda$ with its dependence as $\nu^{-0.1}$ (see Sect. 2.1.2). As discussed in Sect. 2.1.4, FFA is the most likely turnover process affecting the synchrotron spectrum of PACWBs at lower frequencies. This will be further discussed in Chap. 5.

The fitting based on this foreground absorption model will allow us to determine α_{TH}, α_{NT} and the normalization coefficients A, B and C. These will characterize the radio emission for WR147.

4.2.2 The thermal part of the Spectrum

The first step of this general fitting is to characterize the contribution of the thermal emission to the spectrum.

By comparing Fig. 2.5 and Fig. 4.3, one could see at first sight that the L-band accounts more likely mainly for the non-thermal part of the emission and the C-band for both thermal and non-thermal emission components.

The thermal contribution can be determined based on existing published data, especially at high frequencies where it dominates the radio spectrum of a PACWB. The thermal contribution, as explained in Sect. 2.2, is an important contribution of the radio emission coming from a massive binary system. The thermal emission measurement at higher frequencies allows us to evaluate how much it contributes to the radio emission at any frequency. In particular, the extrapolation at lower frequencies of the thermal spectrum is necessary to remove it from our measured radio emission. It permits to isolate the non-thermal part of the emission which is directly linked with the particle acceleration process.
Because the C-band values result from the addition of both thermal and non-thermal emissions, it is difficult to use them to determine only the thermal emission from this system. Consequently, radio measurements at higher frequencies than those obtained with our VLA data were extracted from the literature (Contreras et al., 1996; Williams et al., 1997). These values, representative of the thermal emission coming from WR 147, are summarized in Table 4.2.
The global spectrum including the values of this work and the "external" supplementary values is shown in Fig. 4.4.

The characterization of the thermal part of the WR 147 radio emission will be based only on these external values which are not significantly "contaminated" by the non-thermal emission. In order to model this thermal emission, the thermal parameters of Eq. 4.1

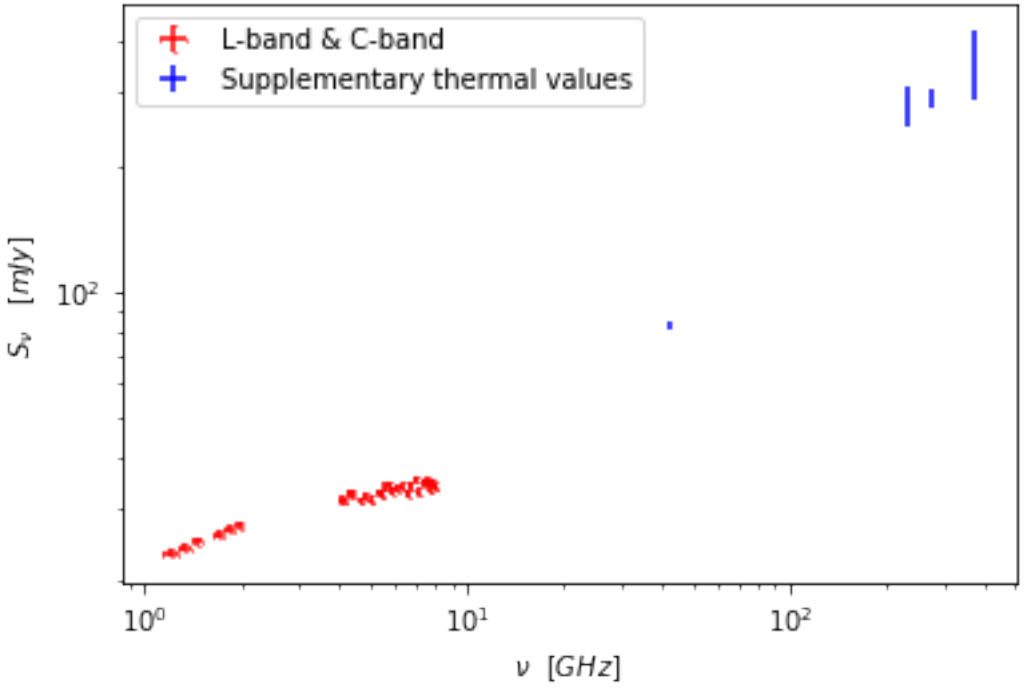

Figure 4.4: General Spectrum including the values of this work (red) and the values taken from the literature (blue) which represent purely thermal emission coming from the source.

($S_\nu = A\nu^{\alpha_{TH}}$) will be determined with these external flux density values. This fit is presented in Fig. 4.5.

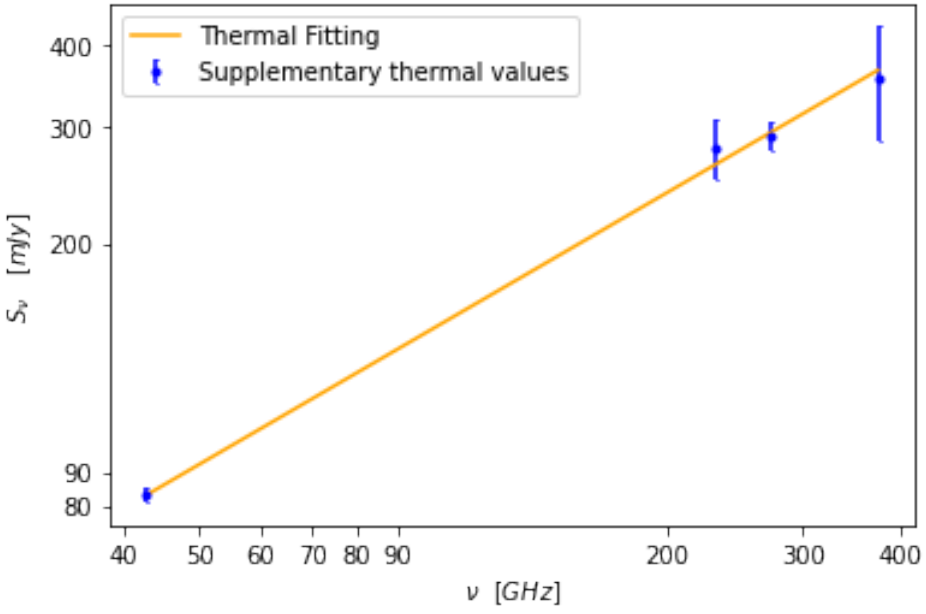

Figure 4.5: Thermal part of the spectrum with the external supplementary thermal values (blue) and the associated fit (orange).

The residuals and the normalized residuals of the thermal emission fitting are shown in Fig. 4.6.

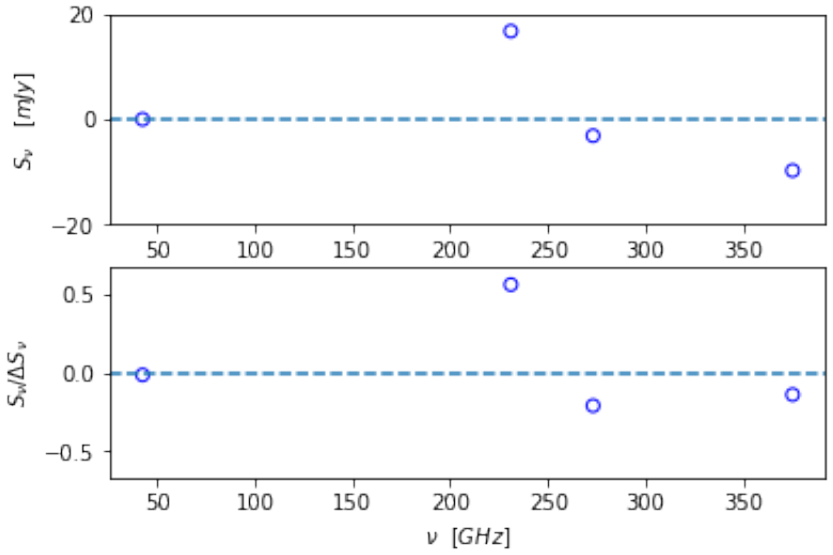

Figure 4.6: Upper panel: Residuals of the thermal fitting. Lower panel: Normalized residuals of the thermal fitting.

The associated χ^2 and the reduced χ^2 (χ^2_{red}) of this fit are:

$$\chi^2 = 0.37 \tag{4.3}$$

$$\chi^2_{red} = 0.19 \tag{4.4}$$

The parameter values deduced from this fit are :

$$\alpha_{TH} = 0.684 \pm 0.027 \tag{4.5}$$

$$A = 6.346 \pm 0.744 \quad (\mathrm{mJy/MHz^{\alpha_{TH}}}) \tag{4.6}$$

The spectral index is in fair agreement with the value expected for the thermal emission from massive star winds discussed in Sect. 2.1.2. In particular, the value above 0.6 is compliant with the thermal index measured for WR stars.

4.2.3 The synchrotron spectrum

The next step consists of removing the thermal contribution to the L-band and C-band measurements, with the objective of achieving a measurement of the synchrotron spectrum only. To this end, the thermal contribution of L and C bands were extrapolated using the α_{TH} and A values determined above. As shown in Fig. 4.7, the extrapolated thermal values for the C-band and L-band are illustrated by the orange curve.
Then these extrapolated thermal values are subtracted from my flux density measurements. The specific case of non-thermal C-band (so after subtraction of its thermal component) is presented in Fig. 4.8. Data points (in red) present a slope that is completely different from that displayed by the direct values measured in our data. At first sight, they suggest a negative slope, in agreement with the expectation from an optically thin synchrotron spectrum (see also Fig. 2.2).

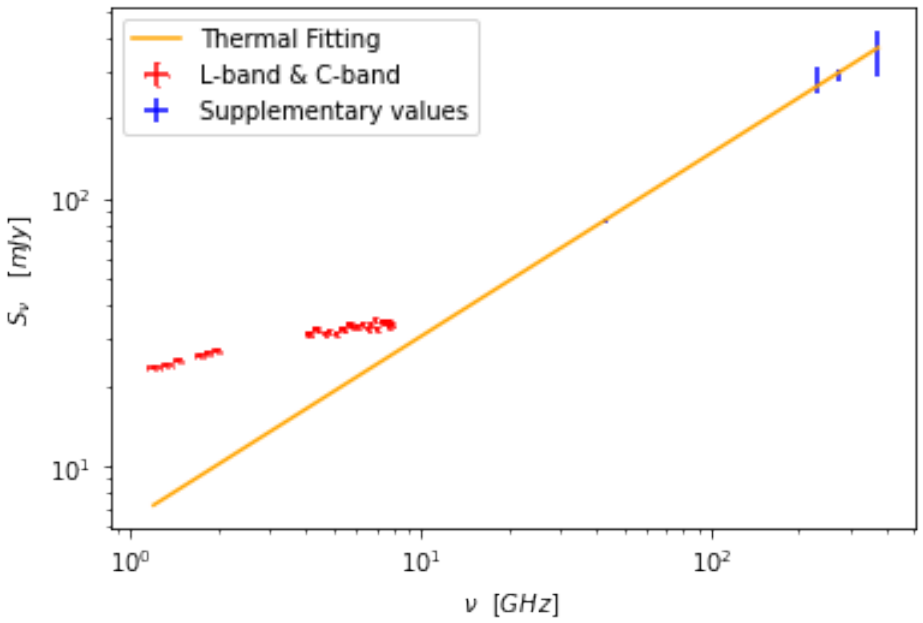

Figure 4.7: General spectrum including values of this work (red) and external supplementary values(blue). The fit based on the external value is also shown (orange). The orange curve below the C-band and L-band represents their thermal contribution. This latter is subtracted from the original measurements to get the non-thermal contribution only.

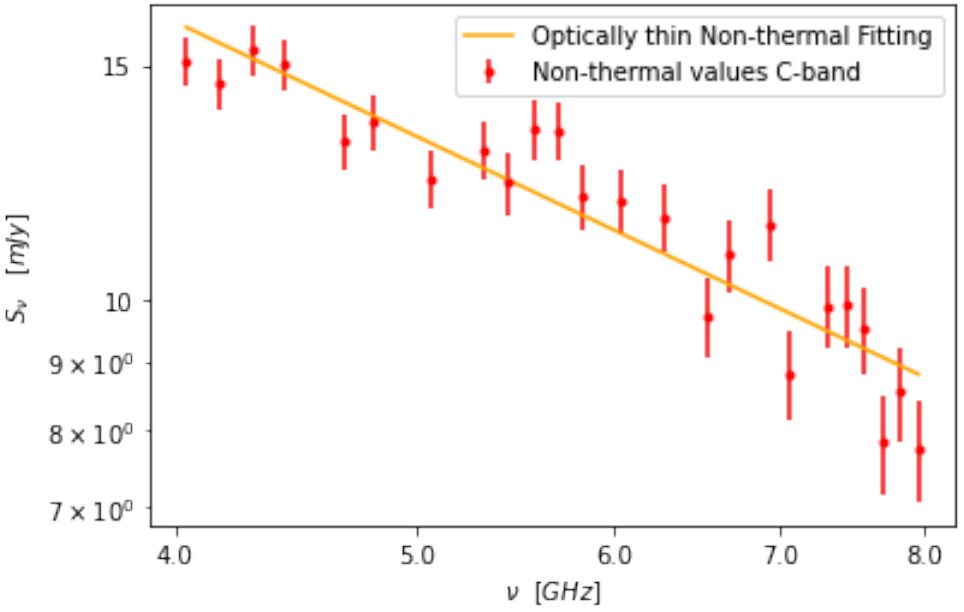

Figure 4.8: Spectrum of the non-thermal component of the C-band. These points correspond to the subtraction of the total C-band with the extrapolated values of its thermal component. It corresponds to the optically thin part of the synchrotron spectrum.

These data points, corrected for the thermal emission, do not seem to be affected by a turnover process. As a result, this optically thin part could be fitted with the $B\nu^{-\alpha_{NT}}$ part of the Eq. 4.1 representing this optically thin part of the synchrotron spectrum, unaffected by any turnover process. This fit is represented by the orange curve in Fig. 4.8.
The residuals and the normalized residuals for the fit of the optically thin non-thermal part of the spectrum are given in Fig. 4.9.

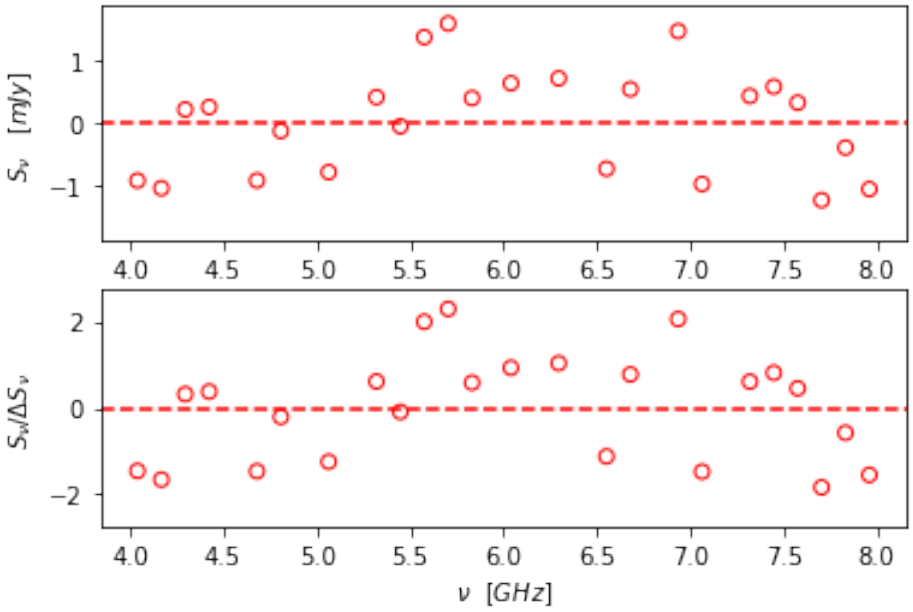

Figure 4.9: Upper panel: Residuals of the non-thermal optically thin fitting. Lower panel: Normalized residuals of the non-thermal optically thin fitting.

The associated χ^2 and reduced χ^2 for this part of the spectrum are :

$$\chi^2 = 36.66 \tag{4.7}$$
$$\chi^2_{red} = 1.66 \tag{4.8}$$

The parameters of this fit on the optically thin part of the spectrum are :

$$\alpha_{NT} = 0.88 \pm 0.076 \tag{4.9}$$
$$B = 54.89 \pm 7.48 \quad (\mathrm{MJy} \times \mathrm{MHz}^{-\alpha_{\mathrm{NT}}}) \tag{4.10}$$

In order to go further in the analysis of the full synchrotron spectrum, as a second step, both L-band and C-band are included in the fit. This time, we have to consider a part of the non-thermal spectrum that is affected by a turnover process (specifically, FFA). In the same way as it was done for the C-band, the thermal contribution of the L-band was removed to have only the non-thermal emission of this band. Indeed, as seen in Fig. 4.7, the extrapolated thermal values of the L-band seem to be non-negligible. The last parameter to determine, C, can be determined by including the non-thermal part of the L-band. The fit was made on the complete non-thermal part of Eq. 4.1, $B\nu^{-\alpha_{NT}} \exp -C\nu^{-2.1}$, with B and α_{NT} fixed to the values determined above.
The fit is displayed in Fig. 4.10 with the orange curve and the red points representing the non-thermal emission of L and C-bands.

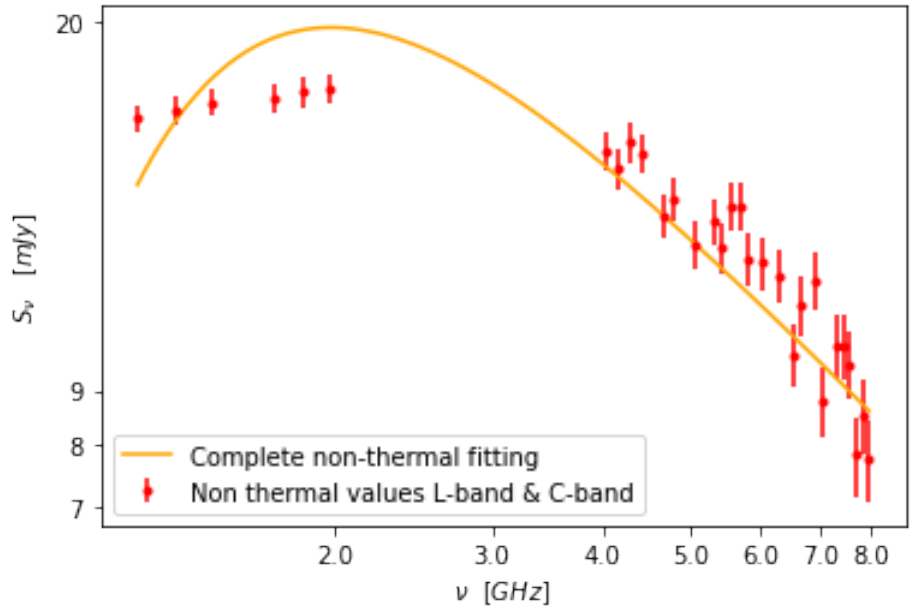

Figure 4.10: Spectrum of the non-thermal component of the L and C-bands. It includes the optically thin part of the spectrum and the part that is affected by the turnover process.

The residuals and normalized residuals of this fit are shown in Fig. 4.11:

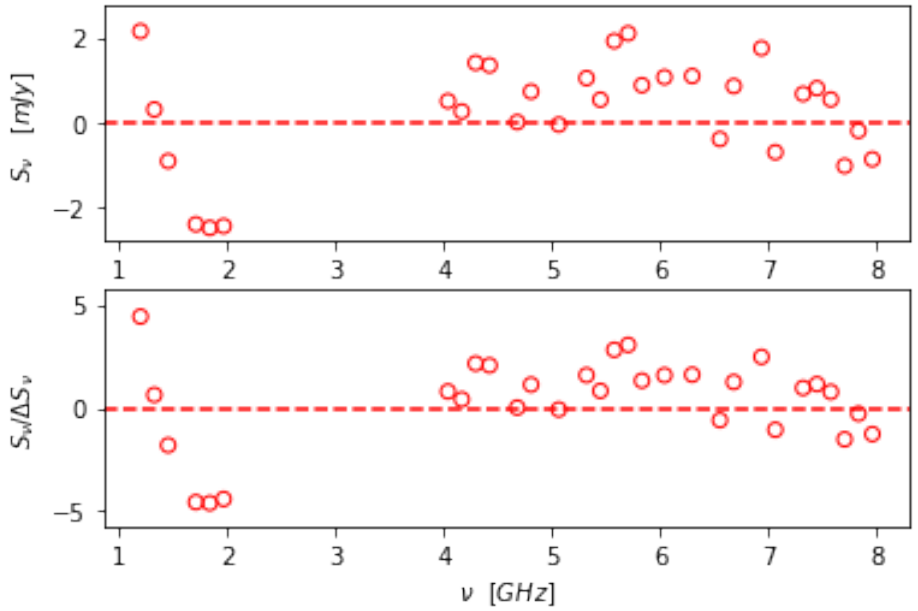

Figure 4.11: Upper panel: Residuals of the non-thermal spectrum with L-band and C-band. Lower panel: Normalized residuals of the non-thermal spectrum with L-band and C-band.

The associated χ^2 and reduced χ^2 for this fit are :

$$\chi^2 = 140.08 \tag{4.11}$$

$$\chi^2_{red} = 4.83 \tag{4.12}$$

With this fit, the value found for the parameter C is :

$$C = 1.76 \pm 0.08 \quad (\mathrm{MHz}^{2.1}) \tag{4.13}$$

A visual inspection of Fig. 4.10 and the associated residuals in Fig. 4.11 shows that the part of the spectrum that is affected by the turnover (L-band) is not well fitted by the *foreground absorption model*. There is an overestimation for one part of the points (lower frequencies of the L-band) and an underestimation for the other part (higher frequencies of the L-band).

4.2.4 Global non-thermal fitting

The step-by-step approach adopted so far is useful to make sure that the best-fit parameters converge to physically relevant values, e.g. α_{TH} and α_{NT}, compliant with the nature of the emission processes at work in this system. To verify these results, one could make this same fitting with the non-thermal contributions of the C-band and L-band simultaneously, without fixing any parameter. In other words, α_{NT}, B, and C are determined simultaneously, based on both non-thermal fluxes from L and C-band. This new fit gives the following parameters :

$$\alpha_{NT} = 0.77 \pm 0.078 \tag{4.14}$$

$$B = 47.11 \pm 6.80 \quad (\mathrm{MJy} \times \mathrm{MHz}^{-\alpha_{\mathrm{NT}}}) \tag{4.15}$$

$$C = 1.53 \pm 0.258 \quad (\mathrm{MHz}^{2.1}) \tag{4.16}$$

$$\tag{4.17}$$

Since the deduced parameters with this fit are comparable to the previous method, the resulting spectrum is similar to Fig. 4.10.
The χ^2 and reduced χ^2 for this fit are :

$$\chi^2 = 99.68 \tag{4.18}$$

$$\chi^2_{red} = 3.69 \tag{4.19}$$

4.2.5 Global fitting

The previous subsections were dedicated to a manual fitting made step-by-step accounting for the different contributions of the emissions. Now, the global fitting can be presented with the parameters deduced previously with the two different approaches described above and summarized here:

1. α_{NT} and B determined on the non-thermal part of the C-band. The parameter C is determined on the non-thermal parts of both bands. This approach refers to the Sect. 4.2.3

2. α_{NT}, B, and C are determined at the same time on the non-thermal parts of both bands. This approach refers to the Sect. 4.2.4

The global radio spectrum, including both thermal and non-thermal contributions, is built with Eq. 4.1. Over-plotting our data with a complete fitting with the associated parameters found in Sect. 4.2.3 gives the result shown in Fig. 4.12.
The associated residuals and normalized residuals are shown in Fig. 4.13

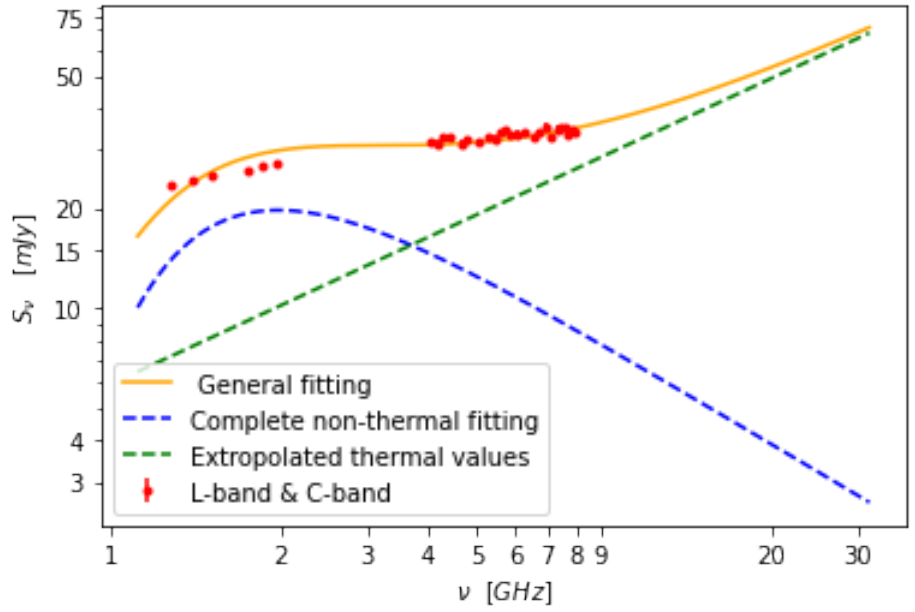

Figure 4.12: Flux values for L-band and C-band with the fit based on the parameters found with the first approach. The green curve represents the thermal fitting based on the external values (Sect. 4.2.2). The blue curve represents the non-thermal fitting (Sect. 4.2.3). The orange curve represents the total fitting including both thermal and non-thermal contributions of the emission.

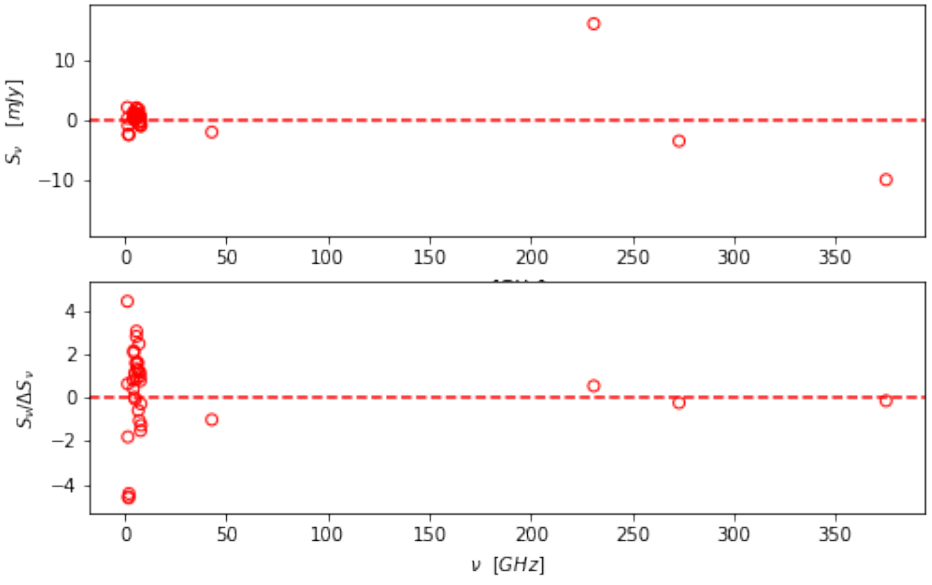

Figure 4.13: Upper panel: Residuals of the complete spectrum for the first approach. Lower panel: Normalized residuals of the complete spectrum for the first approach.

A second global spectrum can be obtained with the second approach and thus with its associated parameters. This fit is displayed in Fig. 4.14

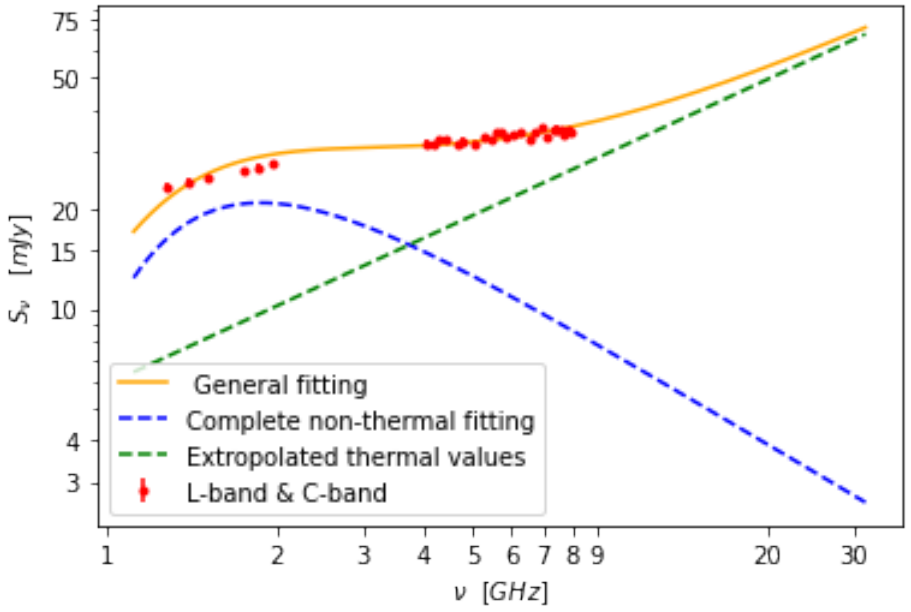

Figure 4.14: Flux values for L-band and C-band with the fit based on the parameters found with the second approach. The green curve represents the thermal fitting based on the external values(Sect. 4.2.2). The blue curve represents the non-thermal fitting(Sect. 4.2.4). The orange curve represents the total fitting including both thermal and non-thermal contributions of the emission.

The associated residuals and normalized residuals for this second approach are shown in Fig. 4.15

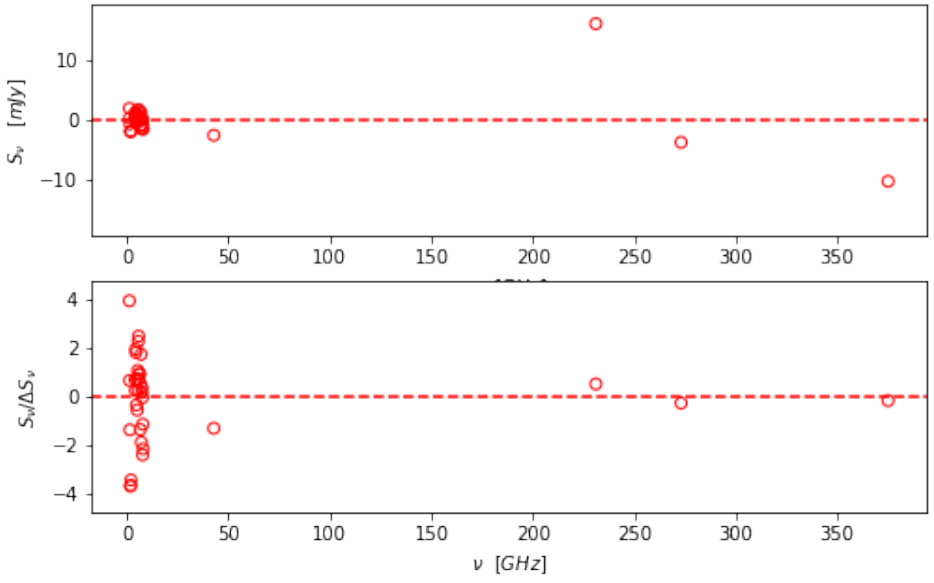

Figure 4.15: Upper panel: Residuals of the complete spectrum for the second approach; Lower panel: Normalized residuals of the complete spectrum for the second approach.

A quick comparison can be made between the two approaches based on the parameters and the χ^2 and χ^2_{red} for the global fitting. This comparison is shown in Table 4.3. Parameters

	Approach 1	Approach 2
α_{TH}	0.684 ± 0.027	0.684 ± 0.027
α_{NT}	0.88 ± 0.076	0.77 ± 0.078
A	6.346 ± 0.744	6.346 ± 0.744
B	54.89 ± 7.48	47.11 ± 6.80
C	1.76 ± 0.08	1.53 ± 0.258
χ^2_{red}	4.87	3.51

Table 4.3: Comparison between the two approaches for the modelling.

α_{TH} and A are similar because they were fitted with the same thermal model in the two approaches (Sect. 4.2.2). The other parameters have close values in the two approaches but the χ^2_{red} is lower in the second approach.

4.2.6 Additional value from uGMRT

To go further in our investigation of the behavior of the target in the low-frequency part of the radio spectrum, it is relevant to include a measurement from another study in our discussion. The selected value comes from Benaglia et al. (2020) obtained with the upgraded Giant Meterwave Radio Telescope (uGMRT):

$$\begin{aligned} \nu_{uGMRT} &= 0.610 \ \text{(GHz)} \\ S_{\nu_{uGMRT}} &= 20.6 \ \text{(mJy)} \\ \Delta S_\nu &= 0.3 \ \text{(mJy)} \end{aligned}$$

It gives the following non-thermal spectrum, displayed in Fig. 4.16:

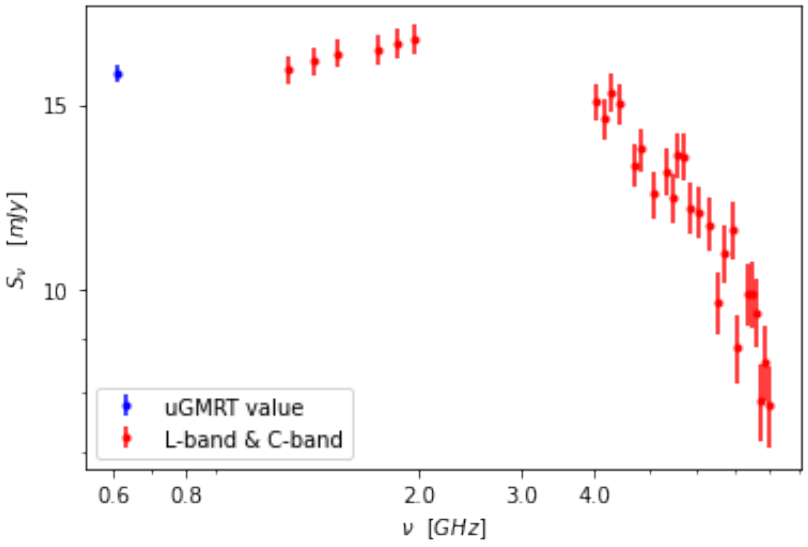

Figure 4.16: Non-thermal spectrum including L-band and C-band (in red), and the additional flux density determined by Benaglia et al. (2020) from uGMRT data (in blue).

One clearly sees that the uGMRT measurement is completely incompatible with the exponential drop considered in the part of the spectrum affected by the turnover process.

Indeed, the supplementary point at a lower frequency has a much too high flux density compared to the L-band series of measurements. This statement, motivated by visual inspection of the data points in the spectrum, has been confirmed by failed attempts to fit the foreground absorption model to the full set of flux densities. *This confirms that the foreground absorption model is not adequate to reproduce the behavior of WR 147 at low radio frequencies.*

4.3 Internal absorption model

4.3.1 Presentation of the model

In the previous Section, due to the residuals of the global fitting and the supplementary value given by the uGMRT, it was shown that a new model is required to represent the flux density of WR 147. Indeed, visual inspection of the fitting and residuals indicates that it is unsuitable for the radio spectrum of WR 147. In particular, *the low-frequency radio emission is much less severely absorbed than expected for a pure foreground absorption.*

In Sect. 2.1.2, the free-free spectrum from an ionized cloud was presented. In this example, it was assumed that the thermal emission coming from this cloud may be absorbed by the thermal electrons present in the same cloud. The region is both an emitter and an absorber. This leads to the spectrum presented in Fig. 2.1 with a decrease of the emission at frequencies lower than the cut-off frequency following a regular trend (without any abrupt exponential cut-off).
A similar case is given in Sect. 2.1.3, where the synchrotron emission region is also the region where the relativistic electrons may absorb the emission. In this case, the resulting spectrum was given by Fig. 2.2 characterized by an optically thin part with a slope given by the spectral index α and an optically thick part at lower frequencies dominated by synchrotron self-absorption.

However, in Sect. 2.2 dedicated to the emissions of a binary system, the assumptions are different. On the one hand, the thermal emission comes from the wind of the stars and the non-thermal emission comes from the WCR. On the other hand, the absorption of the emission, more particularly the non-thermal emission, is considered to be effective in the region along the line of sight of the observer by free-free absorption. In other words, the non-thermal emission will be absorbed by the thermal electrons present in the wind (gas column) which is situated between the region of emission and the observer. This is the foreground absorption model. This model is represented by Eq. 4.1 in which the non-thermal emission is affected by the FFA through the decreasing exponential but this behavior is not in agreement with the non-thermal radio spectrum observed for WR 147.

Therefore, in this work, another model is investigated to better match the behavior of the radio emission of WR 147: the *internal absorption model*. In short, *this model considers that only thermal electrons present in the synchrotron emission region contribute to FFA, with no significant additional absorption along the line of sight by the surrounding wind material.*
The expression used to represent the internal absorption model is based on the radiative transfer equation of synchrotron emission, Eq. 2.27. Nonetheless, the synchrotron absorption coefficient will be replaced by a free-free absorption coefficient leading to the following equation:

$$I_\nu = \frac{J_\nu}{4\pi\ \overline{\kappa^{ff}_{\nu,mod}}}\Big(1-\exp(-\tau_\nu)\Big)$$
$$= \frac{J_\nu}{4\pi\ \overline{\kappa^{ff}_{\nu,mod}}}\Big(1-\exp\left(-\overline{\kappa^{ff}_{\nu,mod}}\,L\right)\Big) \tag{4.20}$$

where $\overline{\kappa^{ff}_{\nu,mod}}$ expresses an equivalent modified free-free absorption coefficient, averaged along the considered line of sight. This parameter can also be seen as some kind of generalized and averaged absorption coefficient. It plays the role of the factor in the general spectrum that will alter the spectral energy distribution in the lower part of the spectrum. In other words, for a given value of the optically thin non-thermal spectral index, this parameter is in charge of ruling the measured spectral index below the internal FFA turnover.

Similarly to Chap. 2, two frequency regimes can be drawn at first order:

- **High-frequency regime** :

$$I_\nu = \frac{J_\nu}{4\pi\ \overline{\kappa^{ff}_{\nu,mod}}}\overline{\kappa^{ff}_{\nu,mod}}L$$
$$I_\nu \propto J_\nu \propto \nu^{-\alpha_{NT}}$$

  This corresponds to the optically thin part of the non-thermal emission which is not affected by the turnover process.

- **Low-frequency regime** :

$$I_\nu = \frac{J_\nu}{4\pi\ \overline{\kappa^{ff}_{\nu,mod}}}$$
$$I_\nu \propto \frac{\nu^{-\alpha_{NT}}}{\nu^{-\beta}} \propto \nu^{-\alpha_{NT}+\beta}$$

  This corresponds to the part of the spectrum which is affected by the internal FFA. The parameter β represents the dependence on the frequency of $\overline{\kappa^{ff}_{\nu,mod}}$. β is thus a parameter that has to be tuned to allow the model to reproduce the data below the internal FFA turnover. Given the exploratory nature of this modeling approach, one has to refrain from speculating on any a priori value for β, and it was decided to keep it as a free parameter.

4.3.2 Fitting of the model

Our radio measurements consist in flux densities, and not specific intensities, the former being defined as the integration over solid angle of the latter. As a first approximation, assuming a one-dimension system distributed along only one specific line of sight, the expressions presented at the end of Sect. 4.3.1 can be directly transposed to their equivalent for flux densities.
Based on Eq. 4.20, the total expression used to fit our flux density measurements is:

$$S_\nu = D\nu^{-\alpha_{NT}+\beta}\Big(1-\exp\left(-B\nu^{-\beta}\right)\Big). \tag{4.21}$$

Concerning the thermal part of the spectrum, the method is the same employed in Sect. 4.2. The subtraction of this thermal component to the L-band and C-band is also undertaken in the same manner as Sect. 4.2. In this way, the change of the model will only affect the non-thermal part of the spectrum.

Independent fitting of the pre- and post-turnover parts

Similarly to the previous section, the non-thermal contribution can be divided into two parts: the optically thin part (high-frequency part of the spectrum) and the part affected by the turnover process (low-frequency part of the spectrum), here internal FFA.

The expression used for the optically thin part at higher frequencies can be found based on Eq. 4.21:

$$S_\nu = D\,B\,\nu^{-\alpha_{NT}} \tag{4.22}$$
$$= C\nu^{-\alpha_{NT}} \tag{4.23}$$

With $C = D \times B$. This last expression has the same shape as the one used in Sect. 4.2.3. Indeed, the modification of the model affects mainly the absorbed part of the spectrum. Thus the determined parameters and the associated χ^2 and reduced χ^2_{red} are the same as in Sect. 4.9

$$\alpha_{NT} = 0.88 \pm 0.076 \tag{4.24}$$
$$C = 54.89 \pm 7.48 \quad (\mathrm{mJy} \times \mathrm{MHz}^{\alpha_{\mathrm{NT}}}) \tag{4.25}$$

$$\chi^2 = 36.66 \tag{4.26}$$
$$\chi^2_{red} = 1.66 \tag{4.27}$$

The part of the spectrum affected by FFA at low frequencies is represented by the expression :

$$S_\nu \propto D\nu^{-\alpha_{NT}+\beta} \tag{4.28}$$

The determined parameters for this part of the spectrum and the associated χ^2 and reduced χ^2_{red} are :

$$\beta = 1.00 \pm 0.04 \tag{4.29}$$
$$D = 15.91 \pm 0.35 \quad (\mathrm{mJy} \times \mathrm{MHz}^{\alpha_{\mathrm{NT}}-\beta}) \tag{4.30}$$

$$\chi^2 = 0.10 \tag{4.31}$$
$$\chi^2_{red} = 0.02 \tag{4.32}$$

These parameters give the Fig. 4.17 fits for the optically thin part and the part affected by the turnover process of the non-thermal spectrum.

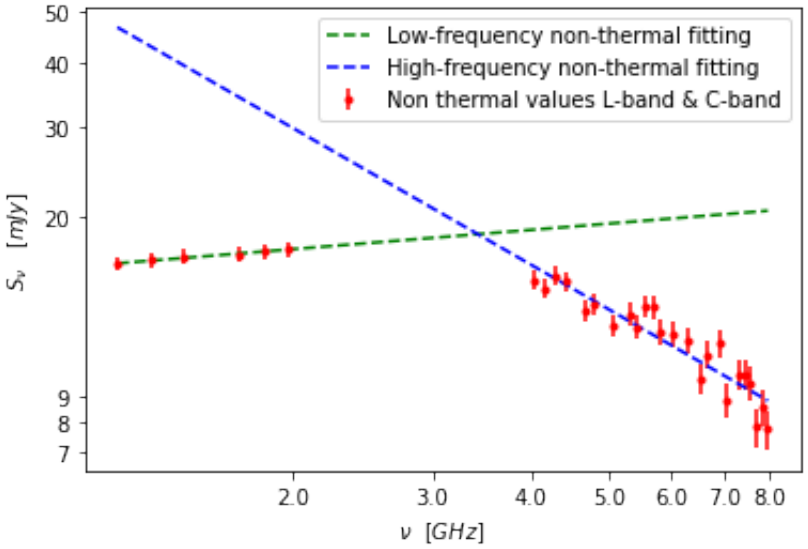

Figure 4.17: Fitting of the non-thermal part of the WR 147 spectrum with the internal absorption model. The optically thin part fit is shown in blue and the part affected by the internal FFA is shown in green.

General fitting with α_{NT} fixed

In Sect. 4.2, two approaches were presented, one where the model parameters are determined "step-by-step" and the other one where all the non-thermal parameters are deduced at the same time on both bands simultaneously. The χ^2_{red} seemed better for this latter approach. Hence, this second approach will be also applied to the internal absorption model. More precisely, the α_{NT} will be fixed to the value determined above since it doesn't change between the two models but the other parameters (β, B, D) will be determined on both non-thermal bands based on the general expression Eq. 4.21.

With this approach, the model parameters are given by:

$$\beta = 1.81 \pm 0.28 \tag{4.33}$$

$$D = 13.28 \pm 1.43 \quad (\text{mJy} \times \text{MHz}^{\alpha_{\text{NT}}-\beta}) \tag{4.34}$$

$$B = 4.52 \pm 0.36 \quad (\text{MHz}^{\beta}) \tag{4.35}$$

The χ^2 and reduced χ^2_{red} are:

$$\chi^2 = 56.65 \tag{4.36}$$

$$\chi^2_{red} = 2.09 \tag{4.37}$$

These parameters give the general non-thermal fitting presented in Fig. 4.18.

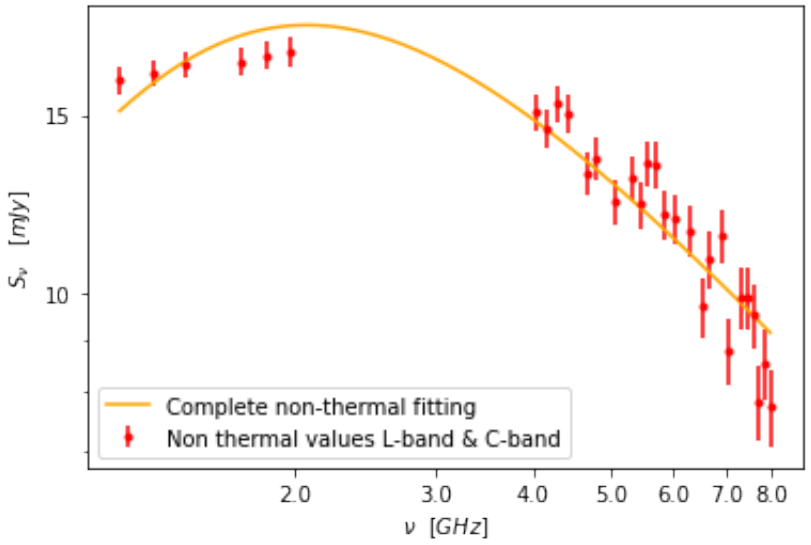

Figure 4.18: General non-thermal fitting of the internal absorption model with the second approach.

It is possible to look at the importance of the two contributions (low frequency and high frequency parts) to this general fit. They are shown in Fig. 4.19.

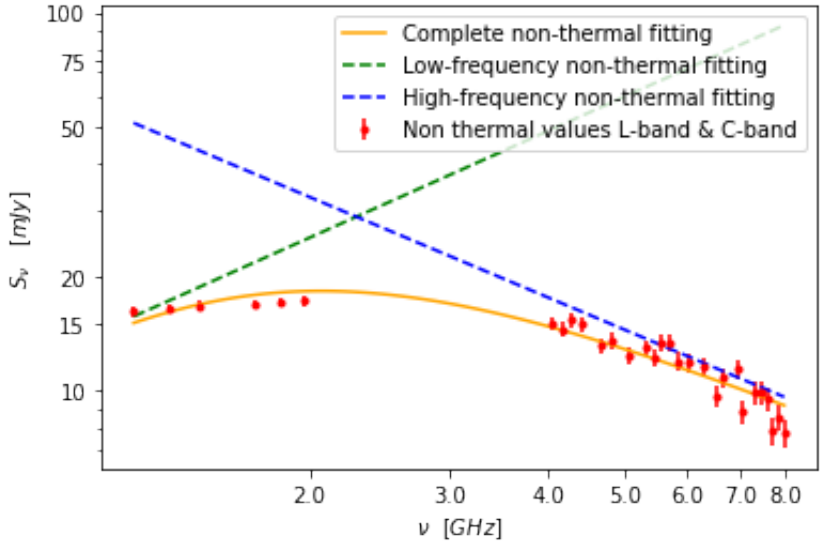

Figure 4.19: General non-thermal fitting of the internal absorption model with the second approach and the two contributions. The optically thin part (high-frequency) is displayed in blue and the part affected by FFA (low-frequency) is displayed in green.

From a visual inspection of Fig. 4.18 and Fig. 4.19 and comparing to the fit obtained in Sect. 4.2, this internal absorption model seems to better represent the behavior of WR 147. Moreover, even though the two χ^2_{red} values are of the same order, the value obtained for the internal absorption model is slightly lower than the one found with the foreground absorption model (Table 4.3).

4.3.3 Additional value from uGMRT

As it was undertaken in Sect. 4.2.6, it might be useful to look at this internal absorption model with the supplementary low-frequency measurement obtained with the uGMRT interferometer. With this additional value, the model parameters and χ^2 become:

$$\beta = 1.15 \pm 0.01 \tag{4.38}$$

$$D = 17.31 \pm 0.54 \quad (\text{mJy} \times \text{MHz}^{\alpha_{\text{NT}}-\beta}) \tag{4.39}$$

$$B = 4.07 \pm 0.13 \quad (\text{MHz}^{\beta}) \tag{4.40}$$

$$\chi^2 = 88.88 \tag{4.41}$$

$$\chi^2_{red} = 3.17 \tag{4.42}$$

This model and the related data are plotted in Fig. 4.20.

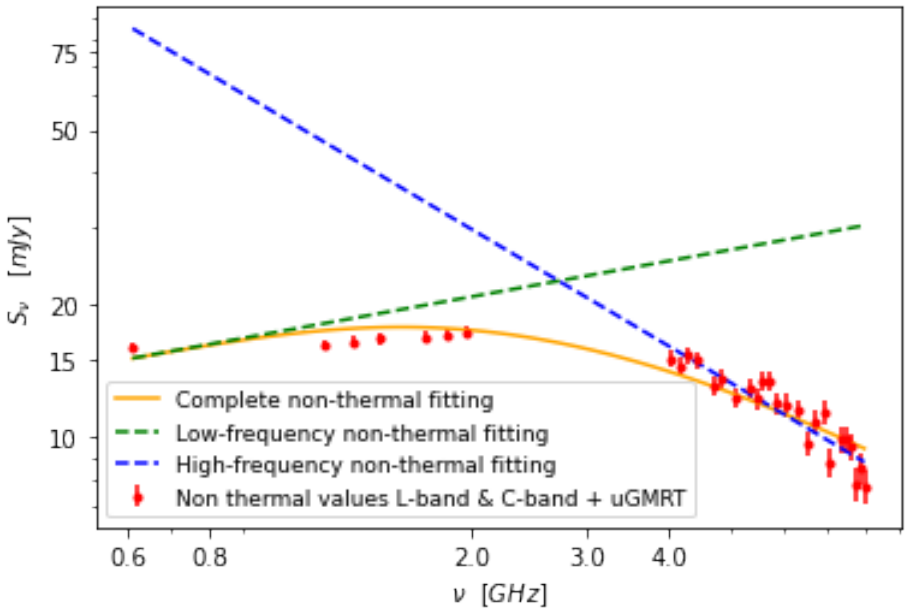

Figure 4.20: General non-thermal fitting of the internal absorption model with the second approach and the two frequency contributions as well as the supplementary value obtained with the uGMRT. The optically thin part (high-frequency) is displayed in blue and the part affected by FFA (low-frequency) is displayed in green.

Even though the internal absorption model doesn't fit the low-frequency values perfectly well, it has the merit not to deviate too much from the full measurement series, at the opposite of the foreground absorption model that completely failed at fitting the uGMRT and L-band data properly.

Chapter 5

Discussion

In this Chapter, several elements of interpretation and discussion about the results obtained in Chap. 4 are presented.

5.1 Determination of the electron index

First of all, one quantity can be deduced directly based on the fitting: the electron index. It was introduced in Chap. 2.

The electron index is related to the synchrotron spectral index by this formula:

$$\alpha_{NT} = \frac{p-1}{2}$$
$$\rightarrow p = 2\,\alpha_{NT} + 1$$

Taking the value of α_{NT} of the internal absorption model, we obtain the following value for the electron population index:

$$p = 2.76 \pm 0.152 \tag{5.1}$$

In the context of DSA in high Mach number shocks (see Sect.1.3), the electron index is expected to be equal to 2. The determined steeper index indicates a slight deviation from the a priori expected behavior.
Such a steep index can be discussed in the context of the shock physics at work in PACWBs, through the following elements:

- The electron index arising from DSA is directly related to the hydrodynamic properties of the shock. In particular, the electron index is determined by the compression ratio (χ) of the shock (see Eq. 1.13). As a result, the compression ratio can be written as:
$$\chi = \frac{p+2}{p-1}$$
Our determination of p gives a gas compression ratio of about 2.7. This is lower than the expected value of 4.0, valid for High Mach number adiabatic shocks and monoatomic gas. In standard DSA theory, such a low value of χ is expected to occur for lower Mach number shocks. However, this is unlikely, since the shocks in WR 147 are highly supersonic. Indeed, the sound speed in a 10^4 K plasma is about 10 km/s and the pre-shock velocity is of the order of 1000 km/s (see Sect. 5.3), resulting in a Mach number of the order of 100 (which corresponds to a high Mach number).

- Radio sources driven by DSA that show a steep index may sometimes be associated with modified shocks. This has been observed, for example, in some young supernova remnants. The basic idea is that a significant population of non-thermal particles can apply some feedback on the shock structure. This results in a modified shock structure that allows for a compression ratio that is not uniform along the shock. As a consequence, lower energy relativistic electrons are influenced by a lower compression, and higher energy relativistic electrons are ruled by a higher compression. As lower energy non-thermal electrons are responsible for the synchrotron radio emission, this may explain the steeper index measured in the radio domain. Particle acceleration by shocks whose structure is modified by accelerated non-thermal particles is called *non-linear* DSA. Even though some models suggest that such a process may be at work in some PACWBs (Pittard et al., 2021), a more accurate determination of the spectral index as a function of frequency is required to investigate this idea.
- The determination of the synchrotron spectral index of other PACWBs based on high angular resolution imaging also yielded values steeper than predicted by the linear DSA theory (De Becker et al., 2024; Sanchez-Bermudez et al., 2019). This is thus not limited to the case of WR 147 studied in this master thesis.

5.2 Determination of the turnover frequency

The turnover frequency is defined as the frequency at which the optical depth is equal to 1, i.e., below which FFA has a significant impact on the measured radio emission, whatever the model considered.
In the case of the *foreground absorption model* (Sect. 4.2), looking at the Eq. 4.1, the turnover frequency is deduced through the value of parameter C:

$$\nu_{turnover} = C^{\frac{1}{2.1}} \tag{5.2}$$

In Sect. 4.2, two approaches were presented with different resulting parameters (Table. 4.3). With the first approach, the turnover happens at the frequency:

$$\nu_{turnover} = 1.23 \pm 0.098 \text{ GHz} \tag{5.3}$$

$$\tag{5.4}$$

With the second approach, it happens at:

$$\nu_{turnover} = 0.83 \pm 0.091 \text{ GHz} \tag{5.5}$$

$$\tag{5.6}$$

In Setia Gunawan et al. (2001), they measured a turnover frequency at about 1000 MHz assuming a foreground absorption model. The values found in this master thesis, for both approaches, are of the same order as the latter. It has to be noted that the foreground absorption model doesn't illustrate well the behavior of the spectrum at low frequencies where the turnover process is effective. Therefore, the values given above are mainly determined for comparison with previous studies.

In the case of the *internal absorption model*, the turnover frequency is derived in the same manner as in the foreground absorption model. In this model, the optical depth is defined based on Eq. 4.21, as:

$$\tau_\nu = B\,\nu^{-\beta}. \tag{5.7}$$

Thus, the turnover due to FFA in the internal absorption model happens at the frequency:

$$\nu_{turnover} = 2.29 \pm 0.31 \text{ GHz}. \tag{5.8}$$

In the internal absorption model, the turnover is reached at higher frequencies than in the foreground absorption model. This indicates that the absorption by thermal electrons distributed in the synchrotron emission region is already influencing the measured spectrum at about 2 GHz.

5.3 Turnover origin

As assumed throughout this work, the turnover process most likely to occur in a PACWB system is FFA. The turnover effect considered in the modeling undertaken in Sect. 4 is thus due to FFA. It was briefly emphasized in Sect. 2.1.4 why this process has a higher contribution than the other two (SSA and Razin-Tsytovitch effect) in a PACWB system.

Nevertheless, it is important to ensure that these two other processes are indeed less likely to occur in WR 147 than FFA .

Firstly, the **SSA** process can be eliminated based on the results obtained by Setia Gunawan et al. (2001). Indeed, Setia Gunawan et al. (2001) demonstrated that this process has a lower probability of occurring in such systems. They used a particular expression related to SSA to get the angular size of the non-thermal source based on the turnover frequency. The basic idea is that a synchrotron source must be compact enough for SSA to be significant. Considering their turnover frequency, this would lead to an angular size of 0.3 mas, which is three orders of magnitude smaller than what was measured on the high angular resolution radio image by Williams et al. (1997) for WR 147. Thus, SSA cannot be responsible for the turnover observed in the multi-band radio spectrum of WR 147.

Secondly, the **Razin-Tsytovitch** (RT) effect can be analyzed in more detail.
The RT turnover frequency is given by Pacholczyk (1970) :

$$\nu_{RT} = 20\frac{n_e}{B} \text{ Hz} \tag{5.9}$$

with n_e being the number density of thermal electrons and B, the magnetic field (both expressed in cgs units). To determine the turnover frequency, one must first have an estimation of these two parameters. These must be evaluated in the synchrotron emission region.

The different required parameters are found in Zhekov et al. (2020) which analyzed WR 147 based on observations made with the Gran Telescopio Canarias and the HST (Hubble Space Telescope). The ones used for the determination of the RT frequency are:

- The mass-loss rate: $\dot{M} = 10^{-4.9}\,\mathrm{M_\odot yr^{-1}} = 8.0\,10^{20}\,\mathrm{g\,s^{-1}}$
- The mean molecular weight: $\mu = 3.21$
- The terminal velocity: $V_\infty = 1000\,\mathrm{km\,s^{-1}} = 10^8\,\mathrm{cm\,s^{-1}}$
- The distance to WR 147: $630\,\mathrm{pc} = 1.94\,10^{21}\,\mathrm{cm}$

- The angular separation between the WR star and the main synchrotron source: $\Delta\theta = 0.6'' = 2.9\,10^{-6}$ rad

The first quantity that can be calculated is the linear separation between the WR star and the main synchrotron source:

$$r = \Delta\theta\, d = 5.7\,10^{15}\,\mathrm{cm} \tag{5.10}$$

This distance is a lower limit on the linear separation for two reasons. Firstly, this is the projected separation, which is equal to the absolute separation only if the line of centers of the long-period binary is perpendicular to the line of sight. Secondly, the assumed distance d (630 pc) is certainly underestimating the actual distance to WR 147.

The second quantity is the local density of the WR wind (before wind collision), which is given by:

$$\begin{aligned} n &= \frac{\dot{M}}{4\,\pi\,r^2\,\mu\,m_p\,V_\infty} \\ &= \frac{8.0\,10^{20}}{4\,\pi\,(5.7\,10^{15})^2\,3.21\,1.67\,10^{-24}\,10^8} \\ &= 3650\ \ \mathrm{cm}^{-3} \end{aligned}$$

Since the mean number of electrons per ion is close to 1, n constitutes a valid estimate of n_e. Assuming a gas compression of factor 4, valid for adiabatic high Mach number shocks (for monoatomic gas), the post-shock density is about $1.5\,10^4\,\mathrm{cm}^{-3}$.

The third quantity is the local magnetic field. It was estimated to be about 5 mG by Setia Gunawan et al. (2001) assuming energy equipartition as presented in Sect. 2.3. For orders of magnitude considerations, let's assume $B = 1$ mG $= 0.001$ G. Since the RT turnover frequency is higher for weaker magnetic fields, this constitutes a conservative limit as compared to the 5 mG value proposed by Setia Gunawan et al. (2001).
Therefore putting these last two values in Eq. 5.9, the RT turnover frequency is:

$$\nu_{RT} = 20\,\frac{1.5\,10^4}{0.001} = 3\,10^8\,\mathrm{Hz} = 300\,\mathrm{MHz}$$

Several remarks can be mentioned :

- The r used in this calculation is a lower limit on the actual linear separation. In addition to the projection effect mentioned above, let's note that the distance to WR 147 could be much longer than 630 pc. According to Gaia DR3 (Crowther et al., 2023), d is estimated to be 1.7 ± 0.1 kpc. Adjusting the distance by a factor 3, the local density drops by a factor 9, leading ν_{RT} to drop by the same factor.
- The actual B strength estimated by Setia Gunawan et al. (2001) is 5 mG, and not 1 mG. Using that value would also shift ν_{RT} to a lower value.

Despite the large uncertainties on several parameters influencing the value of ν_{RT}, it is clear that its value is much lower than the turnover measured by radio data in this work. The influence of the Razin-Tsytovitch effect on the radio spectral energy distribution of WR 147 can be thus ruled out.

The fact that SSA and Razin-Tsytovitch can be discarded as responsible for the turnover process reassures the choice of FFA in the fitting of the non-thermal part of the radio spectrum.

5.4 The influence of the triple nature of WR 147

In Sect. 1.4, WR 147 was presented to be a confirmed binary system made of a WN8 star and an OB companion. Nevertheless, WR 147 may actually be a triple system. This fact was brought up by Rodríguez et al. (2020a) who observed a radio pinwheel structure, at 15GHz, around the WN8 star. Rodríguez et al. (2020a) concluded that this structure would be due to the presence of another star orbiting around the WN8 with a period of the order of 1.7yr.

The triple nature of WR 147 and the existence of this likely additional synchrotron source motivates us to formulate a legitimate question: Can this additional contribution to the radio emission significantly affect our interpretation of the results concerning the main synchrotron source discussed so far?
Given the angular resolution of the radio observations analyzed here, we know that the WR wind, the main synchrotron source, and the additional source associated with the radio pinwheel are unresolved. All these source components are within the synthesized beam of the JVLA in L and C-bands. In the modeling described in Chap. 4, we considered only the thermal emission from the WR wind and the main synchrotron source from the long-period colliding-wind region. The additional radio source being physically independent of the main one, it should be characterized by independent parameters. However, as these two radio sources are not spatially resolved, these parameters cannot be disentangled.

The impact of the additional contribution coming from the pinwheel is rather difficult to evaluate. Indeed, in Rodríguez et al. (2020a) this structure was clearly observed at 15 and 22 GHz but the nature of this emission (thermal or non-thermal) remains undetermined. Given this uncertainty, it is complicated to hypothesize the influence of this pinwheel on the emission at lower frequencies such as L-band or C-band. Yet, Williams et al. (1997) observed WR 147 at 5 and 1.6 GHz with a high angular resolution. In their radio images, at these two frequencies, no pinwheel structure was observed. Consequently, it can be assumed that the influence of the emission from the pinwheel on the lower frequency non-thermal spectrum of this work is either weak or absent.

5.5 The internal absorption model

5.5.1 Relevance of the model

In Chap. 4, it was demonstrated, through the fittings, that the foreground absorption model is not adequate for the WR 147 system. This is the reason why a second model was proposed: the internal absorption model. After examination of the residuals and the value of χ^2, it can be concluded that this model reflects more accurately the behavior of the radio emission emanating from WR 147, although it is not yet a perfect fitting. The main idea of this model was presented in Sect. 4.3.1 but it would be interesting to deepen the motivation behind it.

The justification of this model lies in the very long period of this system which is proposed to be about 1300 years. This period is much greater than for other PACWBs in the catalog (De Becker and Raucq, 2013). Thus, the WCR where the non-thermal emission emerges is much further away from the two components. Since the density of the wind decreases with the square of the distance to the star, its value at the WCR is lower than for many other

PACWBs. The density of the wind material in front of the synchrotron emission region is thus quite low. The density of the wind is closely linked to the FFA process. So, in the case of WR 147, foreground FFA, characterized by an exponential drop at low frequencies, is less likely to happen (at least at the frequencies of our measurements). This could explain why the foreground absorption model doesn't match the non-thermal emission observed in WR 147.

An illustrative example of the internal absorption model is the homogeneous ionized cloud, which is both emitter and absorber (see Sect. 2.1.2). This leads to a spectrum split into two regimes, characterized by different spectral indices (where the low frequency part is mainly dominated by the ratio of the emissivity to the absorption coefficient). In the case of WR 147, the emission region (the WCR) is also the absorption region. In this case, the synchrotron emission will emerge from the WCR and be attenuated by the FFA process in this same region.
The scenario where the same region gives rise to both emission and absorption was investigated by de Bruyn (1976). In this study, de Bruyn (1976) established expressions of the flux density for non-uniform synchrotron sources affected by internal absorption, considering either SSA or FFA. Depending on assumptions about the geometry of the source, the distribution of the magnetic field strength across the source, and the distribution of the density in thermal and relativistic electrons, he derived expressions for the index in the part of the radio spectrum where internal absorption operates. Given the large uncertainties on all the parameters enumerated above, we refrain from using his specific equation to interpret our results. In principle, however, this approach would deserve to be adapted to the geometry of a colliding wind region.

The internal absorption model may only apply to systems with a large orbital period. A large separation between the non-thermal zone and the WR wind is essential. The period of PACWBs usually takes values in the order of weeks or years (Sect. 1.3.3) but can be extended to much higher values such as for WR 147. Nonetheless, it appears that the period of WR 147 is more atypical than representative of the typical values taken by other PACWBs. There are only a very few similar cases where the orbital period reaches high values, potentially allowing to investigate the specific case of internal absorption in massive binaries. Moreover, the conditions required to unveil internal absorption, i.e. clearance of the non-thermal zone of any contamination from a thermal source, would require measuring the radio emission at a sufficiently high angular resolution.

5.5.2 Density distribution dependence of the internal absorption model

One crucial aspect of the internal absorption model is the density distribution of the emission (and absorption) region. A parallel can be drawn with the difference between the thermal emission coming from the uniform ionized cloud (given in Sect. 2.1.2) and the thermal emission emerging from a massive star (Sect. 1.2). It was demonstrated that the optically thick free-free emission coming from the former exhibits a frequency dependence (spectral index) of 2, while it is 0.6 for the latter. The difference between the two values is non-negligible although the physical process behind both cases is the same, i.e., free-free absorption. The difference between these two cases lies in the density distribution. In the case of the homogeneous ionized cloud, the density distribution is uniform with all its parts contributing equally to the emission and absorption. In contrast, the density of the wind decreases with the square of its distance to the star. The density distribution in

the emission/absorption region has a strong impact on the competition between emission and absorption in the region of interest. This translates into significantly different spectral indices from one case to the other.

This can be illustrated based on a given synchrotron spectrum affected by internal FFA, assuming different values of the β parameter. As a reminder, β represents the frequency dependence of the internal FFA active in a given synchrotron emission region. This parameter is tuned to adjust the index of an internally absorbed spectrum to observations, and it is reasonable to assume that it is sensitive to the density distribution. Assuming a synchrotron spectrum with $\alpha_{NT} = 0.88$ (see Chapter 4), Fig. 5.1 shows how the absorbed part of the spectrum is sensitive to β.

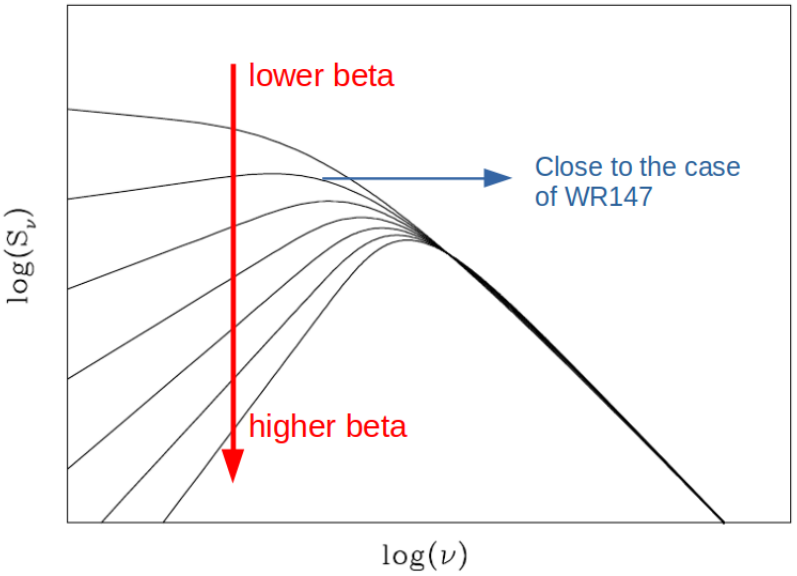

Figure 5.1: Illustration of the effect of the β parameter on an internally absorbed synchrotron spectrum. Below the turnover, β takes values between 0.8 and 2.0 (each steps of 0.2), from top to bottom. The higher the β value, the stronger the internal absorption.

It is clear in Fig. 5.1 that higher values of β lead to a more severe internal absorption. On the opposite, a flatter spectrum is expected for a β value closer to α_{NT}.

5.5.3 The broadband radio spectrum of PACWBs

Another legitimate question can be formulated: Are the foreground absorption model and internal absorption model incompatible? If the internal absorption model appears to be more appropriate for a given non-thermal source, should the foreground absorption model be entirely put aside? In this subsection, it will be shown that both models can be considered at the same time to represent the broadband spectrum of a PACWB.

A more general model is thus built based on the expression of the foreground absorption model (given by Eq. 4.1) and of the internal absorption model (given by Eq. 4.21). The expression related to this general model is given by:

$$S_\nu = A\nu^{\alpha_T} + D\nu^{-\alpha_{NT}+\beta}\left(1 - \exp\left(-B\nu^{-\beta}\right)\right) \exp\left(-C\nu^{-2.1}\right). \tag{5.11}$$

The Eq. 5.11, considers both thermal and non-thermal emission, expressed by the first and the second term respectively. The former has the same meaning as given in Eq. 4.1. The latter is a combination of the non-thermal expressions coming from the two absorption models. The term $D\nu^{-\alpha_{NT}+\beta}\left(1-\exp\left(-B\nu^{-\beta}\right)\right)$ comes from the internal absorption model accounting for the optically thin part and its absorption at lower frequencies. The other term, $\exp\left(-C\nu^{-2.1}\right)$, comes from the foreground absorption model.

This expression aims to generalize the two different absorption models and provides a more general representation of the broadband spectrum of a PACWB. Several examples based on this model are shown in Fig. 5.2. In this figure, all synthetic spectra consider the same optically thin synchrotron spectrum, the same internal absorption (same parameters D, α_{NT}, B, and β parameters) and the same thermal contribution (same parameters A and α_T parameters). Only the C parameter changes when considering cases (a) to (d). The purpose of this series of illustrations is to show how foreground FFA alone can significantly impact the broadband spectrum of a PACWB, assuming a background internally absorbed composite spectrum. These synthetic spectra were built assuming the thermal and non-thermal spectral indices determined in Chapter 4, along with a β value of 1.0, not far from the best-fit value obtained for WR 147. The various cases illustrated in Fig. 5.2 are commented below:

- **Case (a):** If C takes very low values, the absorption process of the non-thermal emission will be dominated by internal absorption over a wide band, while the effect of foreground absorption will appear only at very low frequencies. In fact, the exponential cut-off appears at much lower frequencies than the internal FFA turnover. This case corresponds to a very low amount of foreground material likely to alter the synchrotron spectrum. WR 147 could belong to this category.
- **Case (b):** The increase of the value of C results in a more pronounced foreground absorption, with the exponential cut-off occurring closer to the internal absorption turnover.
- **Case (c):** The foreground absorption is strong enough to make the flatter part of the spectrum due to internal absorption disappears. From this point, no hint of internal absorption can be obtained from the observation. If the sensitivity of the observation is high enough, the non-thermal bump can be measured, superimposed onto the thermal emission.
- **Case (d):** This corresponds to the extreme case in which the foreground FFA is so important that only the thermal contribution of the source can be measured. All the non-thermal emission is absorbed by FFA, and the synchrotron emission from the system can't be detected at all.

The broadband, general model shows that the measured shape of the full radio spectrum of a PACWB depends on various parameters affecting all of its emission and absorption components. Extreme cases can go from an internal absorption-dominated spectrum to a fully thermal spectrum due to a severe foreground FFA. The main example is ηCar which is categorized as a PACWB due to its emission in hard X-rays and γ-rays, but no synchrotron emission has been reported (De Becker and Raucq, 2013). The same is also true for WR 11, which is confirmed as a PACWB thanks to its γ-ray emission (Martí-Devesa et al., 2020), while it displays a full thermal radio spectrum down to about 150 MHz (Benaglia et al.,

2019). According to the general model, these systems potentially may correspond to the extreme case (d), in which all the non-thermal emission is absorbed by the foreground FFA.

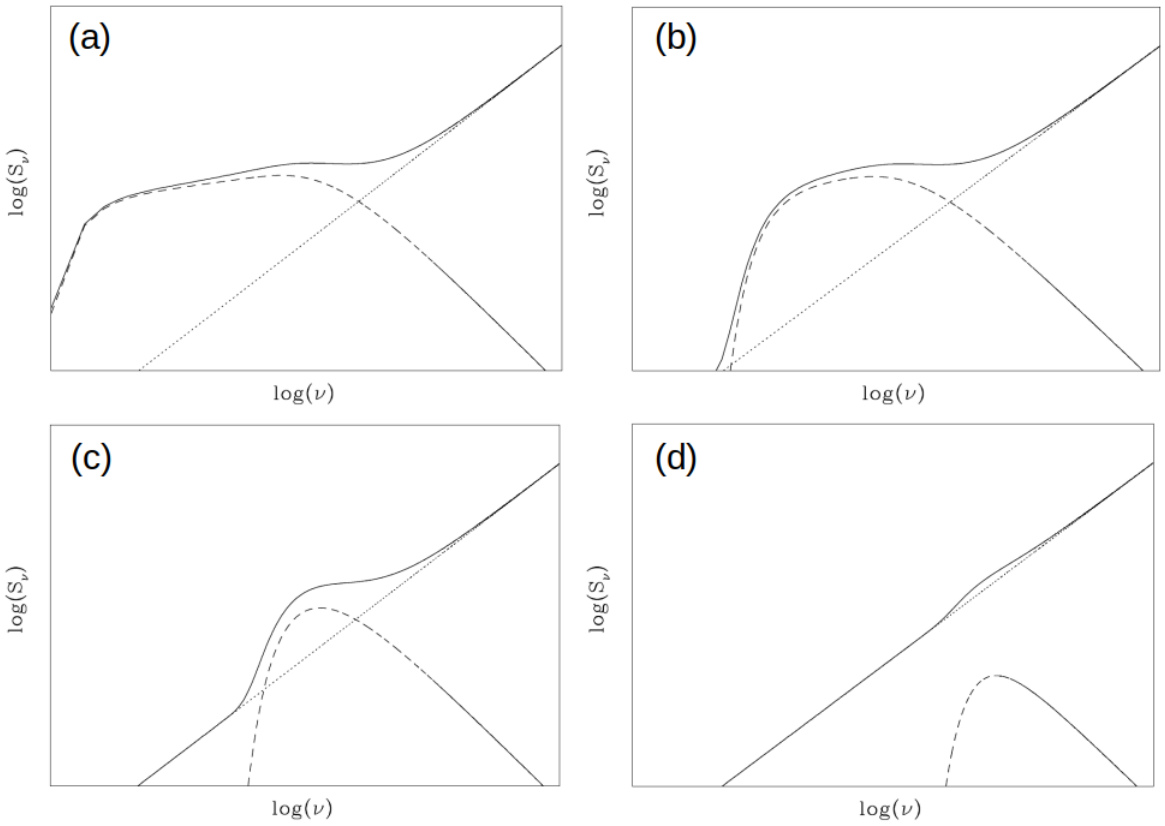

Figure 5.2: Illustration of the effect of a change in turnover frequency due to foreground FFA. From (a) to (d), foreground FFA increases, pushing the cut-off to higher frequencies.

Chapter 6

Conclusions and prospects

6.1 Summary and conclusions

This master's thesis has covered several main aspects of radio astrophysics. In **Chapter 1**, it started with the global properties of massive stars with a particular focus on Wolf-Rayet stars. The multiplicity of these stars, coupled with their powerful winds, has led to the categorization of binaries known as CWB. Since shock physics plays a key role in CWB, these have been developed in this context, with particular emphasis on DSA, which is essential for accelerating the electrons in the wind collision region. In this manner, PACWBs were defined as CWBs in which the electrons are accelerated to relativistic velocities. This work was dedicated to one of these objects: WR 147. Its selection was mainly based on the fact that it had already been identified as a PACWB and that it is one of the brightest systems in the radio domain.

In **Chapter 2**, the fundamentals of radio astrophysics were explained with the different types of emission, i.e., thermal free-free emission and synchrotron emission. For both types of emission, a simplified example was presented with their possible regimes and the resulting spectrum. In addition, a general spectrum resulting from the addition of these two types of emission was discussed along with three distinct turnover processes (FFA, SSA, and RT) that could significantly affect the radio spectrum. Subsequently, the particular radio emission and its associated theoretical spectrum emanating from a massive binary system was detailed.

The practical part of the radio data processing was described in **Chapter 3**. It includes an overview of the basics of interferometry which allows us to understand how the data are collected with the interferometric array, in this case, the JVLA. Then, all the data processing accomplished during this master's thesis was depicted. The first step was flagging. It was highlighted that this task was particularly time-consuming and difficult due to notably the high level of RFI, especially in the L-band. Calibration is the second essential step which allows the data to be calibrated against well-known sources. The final step, imaging, transforms the visibility data into a sky brightness distribution, creating an image of the source. The different parameters used in this work for imaging for both bands were explained as well as the Self-Calibration performed. The target was observed and reduced in two bands (C and L), and the flux densities were also obtained in both bands, despite the poor data quality of the L-band. Several methods were tested to deal with the omnipresence of RFI in the L-band.

One of the most significant aspects of this work is the use of multi-frequency images (**Chapter 4**). Typically, radio spectra are constructed with a single point per band. An important aspect of this master's thesis was to divide both L-band and C-band into sub-bands, to provide a more accurate view of the behavior of the source. This was achieved thanks to the high enough brightness of the source and the quality of points in each band after flagging and calibration. In this way, flux density and noise values associated with each measurement were obtained in each sub-band, although some of them were discarded due to a higher noise level.
With these flux densities, a first fitting was proposed based on the *foreground absorption model* assuming free-free absorption. Different parameters were deduced such as α_{TH} or α_{NT}. The values found were in agreement with the theoretical values. The theoretical radio spectrum of a binary system was globally recovered. However, it was observed that this foreground absorption model failed to represent the part of the spectrum affected by the turnover process. That is why a new model, the *internal absorption model*, was necessary. The key point of this model is the near absence of absorption of the non-thermal emission along the line of sight by the surrounding material. The absorption by the thermal electrons only takes place in the same region as the emission. Similarly to the approach undertaken with the foreground absorption model, a fitting was performed based on this new model. Despite not providing an exact fit to the low-frequency part of the spectrum, the internal absorption model offered a more precise representation of the absorption physics at play in WR 147.

Furthermore, in **Chapter 5**, several topics worth of discussion were addressed. The first one was the determination of the electron index which can be directly related to the shock physics present at the WCR. Thanks to its value, the compression ratio χ could also be determined. Nevertheless, the resulting value was lower than anticipated for a high Mach number adiabatic shock. Additionally, modified shocks and non-linear DSA were also discussed in relation to the electron index value. A second physical quantity that has been determined is the turnover frequency in the context of the two models proposed in the fitting. Then, the turnover was proven to be of FFA origin by discarding the two other processes, SSA and RT. The potential influence of a third star orbiting around the WR star was also qualitatively assessed and, at first glance, appeared to have no influence on the results obtained in this work.
The last, and most important points of the discussion were devoted to the *internal absorption model*. The relevance and the justification of this model have been explained by comparison with examples presented in the chapter on radio emission. In addition, the atypical behavior of WR 147 was highlighted indicating that this model may not apply to other WR systems with a shorter period. Furthermore, it was also pointed out that this model is highly dependent on the density distribution in the wind collision region, more particularly through the factor β as shown in Fig. 5.1.
On top of that, a more general model combining the foreground absorption model and the internal absorption model has been proposed. This model aims to explain the behavior of PACWBs with varying degrees of internal and foreground absorption.

In conclusion, the scientific questions and objectives of this master's thesis, presented in Sect. 1.4, have been achieved. Indeed, the multi-band observation of WR 147 was successful and allowed a more detailed study of this target. This shed light on its atypical low-frequency behavior. The *internal absorption model* was proposed to explain the physics

behind it. In addition, a new advanced model, based on both *internal absorption model* and *foreground absorption model*, was suggested to generalize the physics of all PACWBs.

6.2 Prospects

In this last section, possible perspectives following this master's thesis will be detailed.

6.2.1 Improvements in data processing

The first immediate perspective of this work lies in the improvement of data processing. Firstly, during the flagging process, described at the beginning of Sect. 3.3, some semi-automatized functions from CASA were used. In particular, the 'tfcrop' mode did not work as intended in the L-band, resulting in the suppression of some spws. One improvement would be to deepen this semi-automatized algorithm and understand how it is implemented. As explained in the dedicated section, this kind of function has a lot of parameters and options that are difficult to handle. Getting the optimal way to apply this function to this dataset for both the L-band and C-band could improve and save time on the flagging, resulting in better quality images and a more accurate estimation of the flux densities.

Another step that was run in its simplest form was the Self-Calibration. This task can also be optimized through many different parameters in addition to its undefined end since it can be repeated as much as desired. In the same way, a deeper understanding and a more appropriate application of this task could improve the quality of the image. Moreover, in this work, it was only applied to each whole band, but another enhancement could be applying this task properly to each sub-band too.

6.2.2 Observations of WR147 at other frequencies

Observations of WR 147 at other frequencies may provide new constraints on its behavior, especially on the low-frequency part of the spectrum where it appears to deviate from the classical foreground absorption model. WR 147 has already been observed at various ranges of frequencies. Some of these observations were used in this work as the high-frequency values shown in Table 4.2 and the additional value at 0.61GHz taken from Benaglia et al. (2020).

One way to investigate is to obtain observations in other frequency bands and measure the flux density values in sub-bands. An interesting frequency band would be the one proposed by the JVLA between 2 and 4 GHz, the S-band[1]. This band lies between the L-band and C-band, and would be particularly useful to understand the transition between the optically thin part of the non-thermal spectrum of WR 147 and the part affected by the turnover process. Furthermore, the turnover frequency would be determined with a higher accuracy.

Another band that can be studied is the P-band of the JVLA. This frequency band takes values between 0.23 and 0.47 GHz. It is located at frequencies lower than those of the L-band. As observed in this work in Chap. 4, the uGMRT value at lower frequencies exhibits a deviation from the L-band behavior. In addition to this, WR 147 could be studied at frequencies where the foreground absorption model would be effective, i.e., at rather low frequencies, as illustrated in Sect. 5.5.3. Studying flux density values at lower frequencies

[1] https://science.nrao.edu/facilities/vla/docs/manuals/oss2016A/performance/bands

than uGMRT may deliver a better understanding of this part of the spectrum and may bring some validation to the more general model. However, it should be noted that the P-band is highly subject to RFI. The analysis into sub-bands may not be possible due to the high level of noise.
The suggestions delivered here concern the JVLA but these observations at lower frequencies can be also undertaken by other suitable radio telescopes such as the uGMRT.

6.2.3 Observations with a higher angular resolution

The L-band and C-band flux densities measured in this work include both thermal and non-thermal components. In Chap 4, the thermal contributions had to be subtracted from these bands to obtain only the non-thermal spectrum of WR 147. These thermal contributions were calculated using some external published values displayed in Table 4.2. Indeed, in this work, the angular resolution of this observation does not permit to resolve the different sources of emission. Although the thermal contribution does not appear to affect severely the results of the non-thermal portion of the spectrum, it would be more precise to directly resolve and only measure this non-thermal component.

This is only feasible if the angular resolution is high enough to separate both contributions. WR 147 has already been resolved by Williams et al. (1997) with the telescope MERLIN at the frequencies 5 GHz and 1.6 GHz with a resolution of 50 and 150 mas respectively. It has to be noted that MERLIN has only three frequency bands at 1.6, 5, and 22 GHz (L, C, and K bands). Thus, the L-band and C-band of MERLIN could be used to measure the non-thermal spectrum of WR 147 without the contamination of the thermal emission. Yet, if the future study is dedicated to the lower frequencies (as mentioned in the previous subsection) MERLIN would not be adequate. According to the angular resolution expression (Eq. 3.2), longer baselines are needed to achieve the same or better resolution than MERLIN at lower frequencies. One telescope array capable of reaching these angular resolutions at such low frequencies is the European VLBI Network (EVN). EVN has several low frequency bands at 0.3, 0.6 and 1 GHz, for example. The length of the longest baseline for the EVN Europe is 7139 km resulting in angular resolution values (for the frequencies mentioned above) of 32, 17 and 10 mas [2]. Since these angular resolutions are sufficient to resolve the WR 147 system at low frequencies, the EVN telescope would be appropriate for the study of this system's non-thermal emission.

6.2.4 Observations of others targets

The previous prospects concerned WR 147 only. However, it is necessary to confront the internal absorption model or the general one, discussed in Sect. 5.5.3, to other multiple systems. For this purpose, several possibilities can be considered.

- The first possibility is to use the PACWB catalog (De Becker and Raucq, 2013). These objects have already been categorized as particle accelerators that fulfill the criteria of identification presented in Sect. 2.2.4. The goal would be to search in this catalog for long-period multiple systems and undertake the same procedure as employed in this master's thesis. Then, the internal absorption model will be evaluated on those targets that are more likely to meet the conditions for this absorption model.

[2] https://www.evlbi.org/capabilities

The internal absorption model would be tested on frequencies similar to those of the L-band of JVLA. In addition, the more general model proposed in Sect. 5.5.3 and the possibility of a foreground absorption model at lower frequencies may also be verified on these targets, as envisaged for WR 147 in Sect. 6.2.2. The requirements would be high-quality data at low frequencies and frequencies even lower than the L-band to identify the location of the low-frequency cut-off, if present.

It is important to note that the target must be sufficiently bright at lower frequencies to perform a sub-band analysis.

- The second possibility is to also use the PACWB catalog but not to search specifically for very long-period multiple systems. The aim would be to confront the more general model of Sect. 5.5.3 with several known "classical" particle accelerator systems and verify its consistency. This general model would be tested on more atypical cases too, and may provide an explanation for these particular spectra thanks to different absorption processes.

Bibliography

P. Benaglia, S. del Palacio, C. H. Ishwara-Chandra, M. De Becker, N. L. Isequilla, and J. Saponara. Investigation of the WR 11 field at decimeter wavelengths. *A&A*, 625:A99, May 2019. doi: 10.1051/0004-6361/201834971.

P. Benaglia, M. De Becker, C. H. Ishwara-Chandra, H. T. Intema, and N. L. Isequilla. Megahertz emission of massive early-type stars in the Cygnus region. , 37:e030, July 2020. doi: 10.1017/pasa.2020.21.

M. E. Contreras, L. F. Rodriguez, Y. Gomez, and A. Velazquez. VLA Observations of Massive Stars at 7 Millimeters. *ApJ*, 469:329, September 1996. doi: 10.1086/177782.

P. A. Crowther. Wolf-Rayet content of the Milky Way. In Wolf-Rainer Hamann, Andreas Sander, and Helge Todt, editors, *Wolf-Rayet Stars*, pages 21–26, January 2015. doi: 10.48550/arXiv.1509.00495.

Paul A. Crowther. Physical Properties of Wolf-Rayet Stars. *Ann. Rev. Astron. Astroph.*, 45 (1):177–219, September 2007. doi: 10.1146/annurev.astro.45.051806.110615.

Paul A. Crowther, G. Rate, and Joachim M. Bestenlehner. Line luminosities of Galactic and Magellanic Cloud Wolf-Rayet stars. *MNRAS*, 521(1):585–612, May 2023. doi: 10.1093/mnras/stad418.

M. De Becker. *Course Radio astrophysics"*. 2022.

M. De Becker and F. Raucq. Catalogue of particle-accelerating colliding-wind binaries. *A&A*, 558:A28, October 2013. doi: 10.1051/0004-6361/201322074.

M. De Becker and V. Van Grootel. *Course Interstellar Medium.* 2022.

M. De Becker, P. Benaglia, G. E. Romero, and C. S. Peri. An investigation into the fraction of particle accelerators among colliding-wind binaries. Towards an extension of the catalogue. *A&A*, 600:A47, April 2017. doi: 10.1051/0004-6361/201629110.

M. De Becker, B. Marcote, T. Furst, and P. Benaglia. High-resolution radio imaging of the two particle-accelerating colliding-wind binaries HD 167971 and HD 168112. *A&A*, 682: A160, February 2024. doi: 10.1051/0004-6361/202348622.

A. G. de Bruyn. Radio spectra of non-uniform synchrotron sources with internal absorption. *A&A*, 52(3):439–447, November 1976.

S. del Palacio, F. García, M. De Becker, D. Altamirano, V. Bosch-Ramon, P. Benaglia, B. Marcote, and G. E. Romero. Evidence for non-thermal X-ray emission from the double Wolf-Rayet colliding-wind binary Apep. *A&A*, 672:A109, April 2023. doi: 10.1051/0004-6361/202245505.

K. Dsilva, T. Shenar, H. Sana, and P. Marchant. A spectroscopic multiplicity survey of Galactic Wolf-Rayet stars. I. The northern WC sequence. *A&A*, 641:A26, September 2020. doi: 10.1051/0004-6361/202038446.

K. Dsilva, T. Shenar, H. Sana, and P. Marchant. A spectroscopic multiplicity survey of Galactic Wolf-Rayet stars. II. The northern WNE sequence. *A&A*, 664:A93, August 2022. doi: 10.1051/0004-6361/202142729.

K. Dsilva, T. Shenar, H. Sana, and P. Marchant. A spectroscopic multiplicity survey of Galactic Wolf-Rayet stars . III. The northern late-type nitrogen-rich sample. *A&A*, 674: A88, June 2023. doi: 10.1051/0004-6361/202244308.

M.-A. Dupret. *Course Stellar Structure and evolution I.* 2022.

C. Farnier, R. Walter, and J. C. Leyder. η Carinae: a very large hadron collider. *A&A*, 526:A57, February 2011. doi: 10.1051/0004-6361/201015590.

Amit Kashi and Noam Soker. Modelling the radio light curve of η Carinae. *MNRAS*, 378 (4):1609–1618, July 2007. doi: 10.1111/j.1365-2966.2007.11908.x.

A. Maeder. The Conti scenario for forming WR stars: past, present and future. In J. M. Vreux, A. Detal, D. Fraipont-Caro, E. Gosset, and G. Rauw, editors, *Liege International Astrophysical Colloquia*, volume 33 of *Liege International Astrophysical Colloquia*, page 39, January 1996.

G. Martí-Devesa, O. Reimer, J. Li, and D. F. Torres. Hints of γ-ray orbital variability from γ^2 Velorum. *A&A*, 635:A141, March 2020. doi: 10.1051/0004-6361/202037462.

F. Martins, D. Schaerer, and D. J. Hillier. A new calibration of stellar parameters of Galactic O stars. *A&A*, 436(3):1049–1065, June 2005. doi: 10.1051/0004-6361:20042386.

L. E. Muijres, Jorick S. Vink, A. de Koter, P. E. Müller, and N. Langer. Predictions for mass-loss rates and terminal wind velocities of massive O-type stars. *A&A*, 537:A37, January 2012. doi: 10.1051/0004-6361/201015818.

T. Nugis and H. J. G. L. M. Lamers. Mass-loss rates of Wolf-Rayet stars as a function of stellar parameters. *A&A*, 360:227–244, August 2000.

T. Nugis, P. A. Crowther, and A. J. Willis. Clumping-corrected mass-loss rates of Wolf-Rayet stars. *A&A*, 333:956–969, May 1998.

S. S. R. Offner, M. Moe, K. M. Kratter, S. I. Sadavoy, E. L. N. Jensen, and J. J. Tobin. The Origin and Evolution of Multiple Star Systems. In S. Inutsuka, Y. Aikawa, T. Muto, K. Tomida, and M. Tamura, editors, *Protostars and Planets VII*, volume 534 of *Astronomical Society of the Pacific Conference Series*, page 275, July 2023. doi: 10.48550/arXiv.2203.10066.

A. G. Pacholczyk. *Radio astrophysics. Nonthermal processes in galactic and extragalactic sources.* 1970.

R. Perley. Fundamentals of radio interferometry, sixteenth synthesis imaging workshop. 16-23 May 2018.

J M Pittard, G S Vila, and G E Romero. Colliding-wind binary systems: diffusive shock acceleration and non-thermal emission. *Monthly Notices of the Royal Astronomical Society*, 495(2):2205–2221, 04 2020. ISSN 0035-8711. doi: 10.1093/mnras/staa1099. URL https://doi.org/10.1093/mnras/staa1099.

J. M. Pittard, G. E. Romero, and G. S. Vila. Particle acceleration and non-thermal emission in colliding-wind binary systems. *MNRAS*, 504(3):4204–4225, July 2021. doi: 10.1093/mnras/stab1107.

G. Rauw. *Course Variable Stars*. 2023.

Luis F. Rodríguez, Jane Arthur, Gabriela Montes, Carlos Carrasco-González, and Jesús A. Toalá. A Radio Pinwheel Emanating from WR 147. *ApJ*, 900(1):L3, September 2020a. doi: 10.3847/2041-8213/abad9d.

Luis F. Rodríguez, Jane Arthur, Gabriela Montes, Carlos Carrasco-González, and Jesús A. Toalá. A Radio Pinwheel Emanating from WR 147. *ApJ*, 900(1):L3, September 2020b. doi: 10.3847/2041-8213/abad9d.

Anindya Saha, Anandmayee Tej, Santiago del Palacio, Michaël De Becker, Paula Benaglia, C. H. Ishwara-Chandra, and Prachi Prajapati. Search for particle acceleration in two massive Wolf-Rayet stars using uGMRT observations. *MNRAS*, 526(1):750–757, November 2023. doi: 10.1093/mnras/stad2758.

J. Sanchez-Bermudez, A. Alberdi, R. Schödel, W. Brandner, R. Galván-Madrid, J. C. Guirado, R. Herrero-Illana, C. A. Hummel, J. M. Marcaide, and M. A. Pérez-Torres. A VLBI study of the wind-wind collision region in the massive multiple HD 167971. *A&A*, 624:A55, April 2019. doi: 10.1051/0004-6361/201834659.

D. Y. A. Setia Gunawan, A. G. de Bruyn, K. A. van der Hucht, and P. M. Williams. WSRT 1.4 and 5-GHz light curves for WR 147 (AS 431, WN8(h)+OB). *A&A*, 368: 484–496, March 2001. doi: 10.1051/0004-6361:20000561.

D. J. Wallace, M. M. Shara, A. F. J. Moffat, and V. S. Niemela. Hst-wfpc2 pc observations of galactic wolf-rayet stars, preliminary results. 1999. URL https://api.semanticscholar.org/CorpusID:117124893.

P. M. Williams, S. M. Dougherty, R. J. Davis, K. A. van der Hucht, M. F. Bode, and D. Y. A. Setia Gunawan. Radio and infrared structure of the colliding-wind Wolf-Rayet system WR147. *MNRAS*, 289(1):10–20, July 1997. doi: 10.1093/mnras/289.1.10.

D. Wilner. Radio astronomy and interferometry fundamentals , lecture i. February 2015.

T. L. Wilson, K. Rohlfs, and S. Hüttemeister. *Tools of Radio Astronomy*. Springer Berlin, Heidelberg, 2013.

A. E. Wright and M. J. Barlow. The radio and infrared spectrum of early type stars undergoing mass loss. *MNRAS*, 170:41–51, January 1975. doi: 10.1093/mnras/170.1.41.

Svetozar A Zhekov, Blagovest V Petrov, Toma V Tomov, and Peter Pessev. A global view on the colliding-wind binary WR147. *Monthly Notices of the Royal Astronomical Society*, 494(3):4525–4538, 05 2020. ISSN 0035-8711. doi: 10.1093/mnras/staa993. URL https://doi.org/10.1093/mnras/staa993.